Edinburgh Wave Power Project

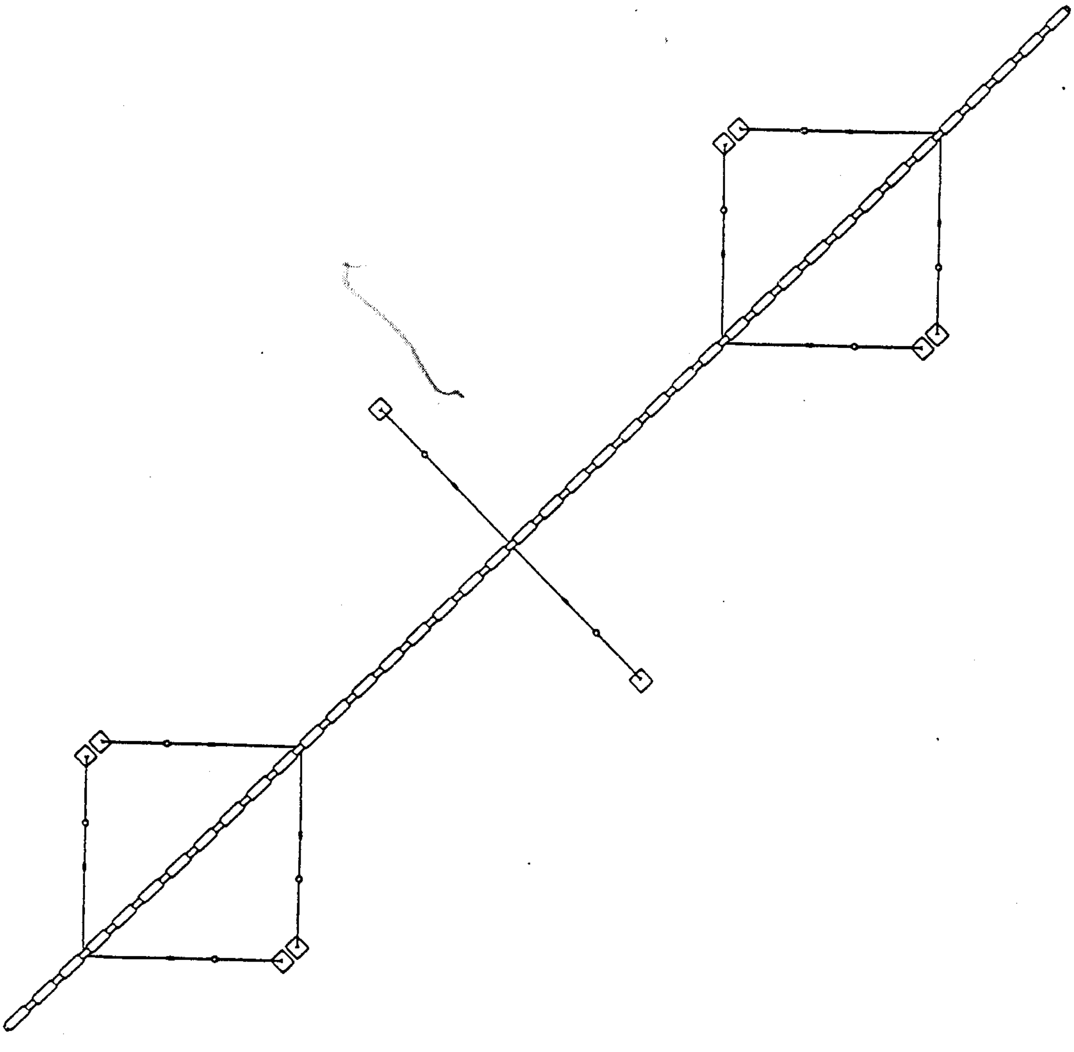

The Long Spine Mooring

1986

THE LONG SPINE MOORING

A report to the Wave Energy Steering Committee
covering work supported by the United Kingdom Department of Energy

EDINBURGH UNIVERSITY WAVE POWER PROJECT

University of Edinburgh

Mayfield Road

Edinburgh EH9 3JL

031 667 1081 X 3276

CONTENTS

LIST OF FIGURES

SECTION 1 INTRODUCTION

In this report we present the specification of the mooring for the long spine model, and a detailed analysis of its static and dynamic characteristics. We describe the experimental investigations of the behaviour of the mooring alone, and coupled to the spine, in a variety of multidirectional seas representative of the full range of North Atlantic conditions.

In preliminary experiments some seas caused the spine to sway axially. Adoption of a new mooring plan solved the problem completely.

Measurements were collected from anchor gauges and a position gauge which gave good resolution, and were robust and easy to use.

The experiments explored the effects of wave loading on the spine and mooring in terms of instantaneous forces and displacements. These measurements were combined with statistical data to deduce the fatigue loading on the mooring.

The fatigue of the electrical down-feeder cables required at full scale is the limiting factor in the mooring design. We present a design for a joint for the cable which reduces fatigue to arbitrarily low values.

All loads, static and cyclic, were found to be within the capabilities of the mooring in its present form. Theory and experiment agreed well, and pointed the way to design improvements which would reduce the loads on the mooring still further.

MAIN CONCLUSIONS

Although most data in this report are presented at tank scale for a 125 mm diameter spine, in this section we have referred numerical values to the 1983 full scale design for the 13.5 metre ducks - ie, a scale of 107.7.

1) A mooring stiffness density of 37 Newtons per metre for each metre of spine length is sufficient to keep the spine on station.

2) The 86 metre surge range of the current mooring will not be required. The weighted mean spine drift in the South Uist wave climate is 3.6 metres aft - about a quarter of a spine diameter. In the extreme 50 year wave the peak aft excursion is 15 metres.

3) The South Uist wave climate produces mooring line tension variations of 100 Newtons per metre of wave height for each metre of spine length. The annual weighted tension variation is less than 3% of the static tension. The 50 year wave produces a peak-to-peak tension variation of 2100 Newtons for each metre of spine length.

4) The South Uist wave climate produces angle variations in the mooring joints of 0.025 radian per metre of wave height. Averaged over a year, the angular variation is 0.018 radian - about one degree. The 50 year wave produces a peak-to-peak angle variation of 0.5 radian.

5) The fatiguing angles imposed on the electrical down-feeder cables are an order of magnitude smaller than the failure bounds determined in industrial tests. The angles may be reduced by a further order of magnitude with the use of a multi-turn cable joint.

6) The South Uist wave climate produces only aft drift of the spine at the anticipated spine stiffness. The appropriate place for down-feeder cables is therefore on the upwave mooring to avoid bottoming problems.

7) A more flexible spine allows greater uncorrelated spine motion, and so results in greater mooring loads.

8) In a typical sea-state, the spine motion contributes about half the loading on the moorings. The rest is due to the action of waves on the float, sinker, and the rodes themselves.

9) Arranging the float so that it is an odd number of half-wavelengths from the spine would reduce the angular response of the mooring. The appropriate wavelength is that of the predominant mixed-sea wave period for the year.

10) Different sea states can cause conspicuously different types of loading on the mooring:
seas with small angular spreading cause large oscillations;
seas with large angular spreading cause large drift;
seas with offset principal direction cause low-frequency surge motion.

11) Joining adjacent mooring pairs to a single anchor point renders spine sway negligible, and provides a worthwhile cost reduction.

MODEL DESCRIPTION

The same spine is used in this series of tests as in previous work, namely the 125 mm diameter articulated model with electronically controlled elasticity. 40 sections are used, giving an overall length of 16 metres.

The mooring comprises sinkers and floats on lines mounted fore and aft of the spine. It is shown in perspective in figure 1.1, which is reproduced from the 1984 long spine report. It was designed to accommodate large surge displacements in the fore and aft directions; the dimensions were therefore made as great as the tank length allowed. Detailed specifications are given in Appendix C.

The mooring lines were originally tried with sinkers and floats three times larger spaced four times more frequently, giving 12 times the stiffness. The present arrangement is more economic, easier to handle, and easily accommodates spine drift.

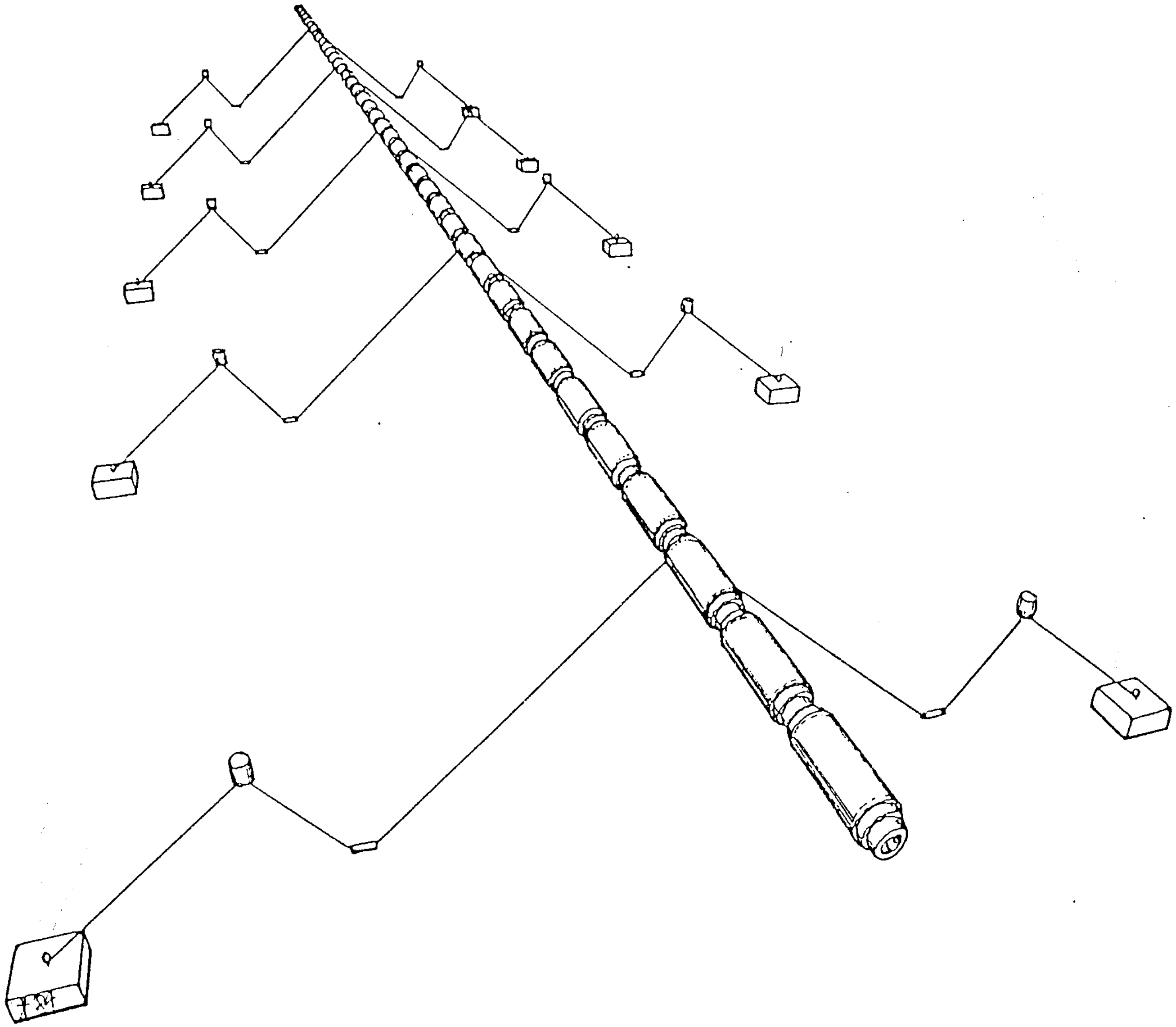

Figure 1.1 View of the mooring arrangement before modification

The mooring arrangement of figure 1.1 has the drawback of allowing considerable axial sway - the restoring force is small and second-order. Furthermore, the cylinder moves through the water along its long axis, so damping is low and the sway oscillations persist. We rearranged the moorings in mirror-image pairs of chevrons, shown in plan in figure 1.2. This greatly increased the restoring force in sway, and oscillations were no longer a problem.

At full scale, attaching the mooring lines in pairs to half the number of double-strength pile heads is significantly cheaper than the original scheme of one pile per line.

Exactly halfway down the length of the spine we retained a mooring with lines at right angles to the spine axis. This was our measurement point. Anchor gauges were placed on both fore and aft mooring lines. The upper ends of the lines were attached to a spine joiner ring, to which were also attached the fore and aft lines of the position gauge. This arrangement allowed the derivation of spine position, and all the mooring angles. The geometry is shown in figure 5.13 in Appendix C.

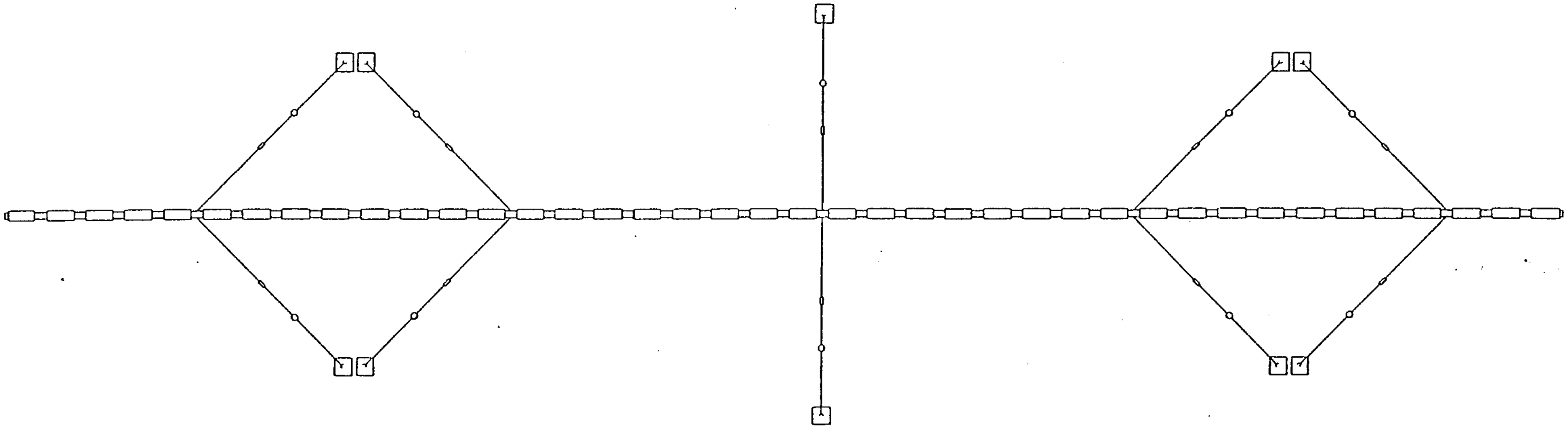

Figure 1.2 Plan of the mooring arrangement after modification

Each mooring line attaches via an eyelet bolt to the ring that joins adjacent spine units. Its bottom end may either attach to a concrete anchor block, as shown in figure 1.1, or to an anchor gauge designed to measure both the vertical and horizontal forces in the mooring line. Providing that the line remains in tension, the angle that the line makes with the horizontal is the arctan of the quotient of the vertical force and horizontal force. The tension in the line is the modulus (the square root of the sum of the squares) of the vertical and horizontal forces. These anchor gauges are described fully in Appendix A.

Although we can infer the position of the spine units relative to each other by integrating the velocity signal from each joint, we needed an absolute position measurement. The commercial ´Selspot´ equipment provides high accuracy, but at a price. We decided on the electro-mechanical position gauge described in Appendix B. It offers 0.25 mm resolution, robustness and ease of use, and can operate under water.

In Appendix C we describe the mooring in detail, and how the position and anchor gauges are used to determine its geometry experimentally. Its theoretical static angles and tensions are derived and are compared with a statics experiment.

In Appendix D we discuss the mooring dynamics and experimentally determine the frequency response.

SECTION 2 FREAK WAVE EXPERIMENTS

For this work we chose a one second Pierson-Moskowitz sea with a Mitsuyasu angular spreading function. We increased its root-mean-square wave height (Hrms) from 13.6 mm to 17.5 mm, and arranged the maximum freak wave possible (corresponding to phase coincidence of all the frequency components) to reach the centre of the spine 10 seconds after the start of sampling. The freak wave measured 227 mm peak to trough. At a scale of 107.7, this corresponds to a 24.5 m wave - slightly larger than can be expected in the Hebridean wave climate at a water depth of 100 m in a 50 year period.

The sampling rate was 20 Hz, the sampling time was 25.6 seconds (corresponding to 266 seconds at full scale). The graphs are derived from data recorded from the anchor gauges and the position gauge.

Figures 2.1 and 2.2 show time series for the vertical and horizontal motion of the spine with a stiffness of 800 Nm2.

Note that the surge time series is larger and shows substantial low-frequency drift with time.

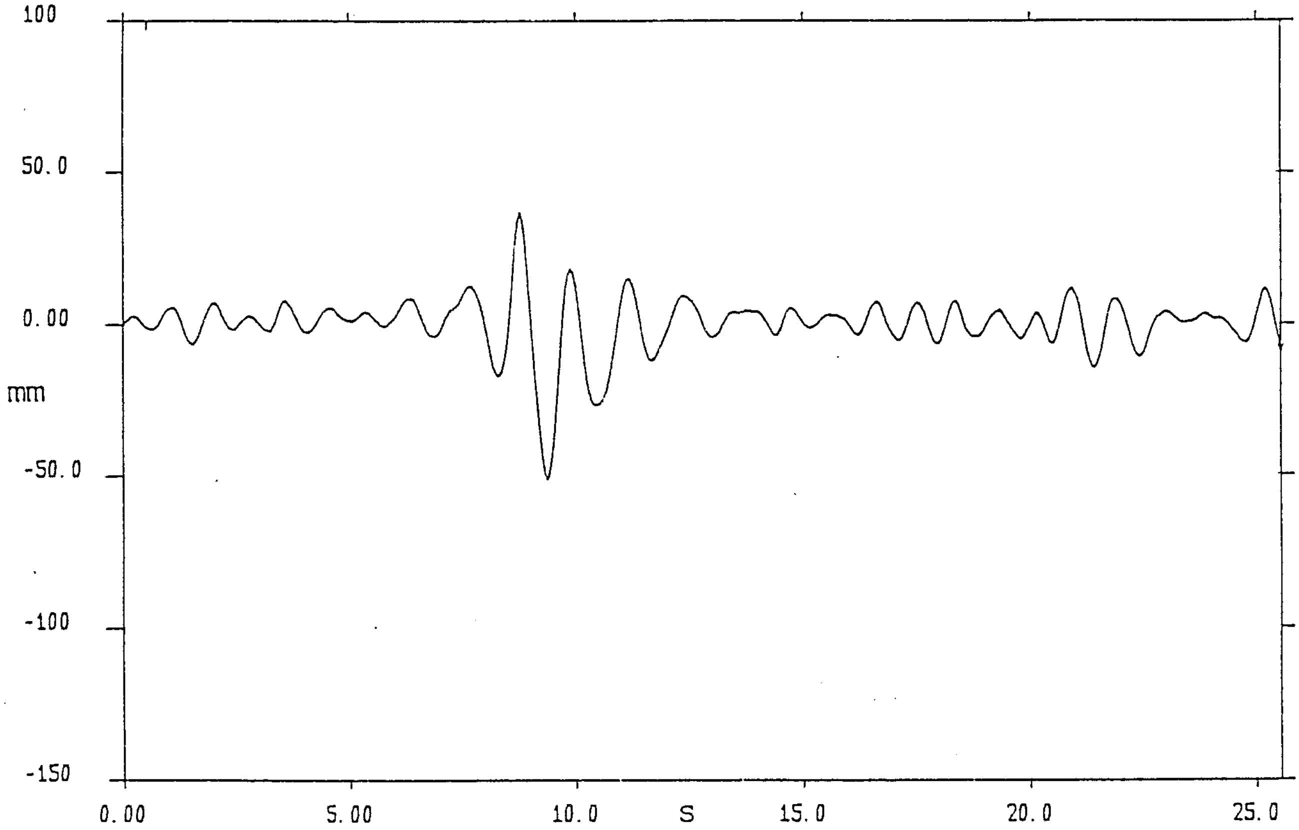

Figure 2.1 Freak wave. Heave motion EI = 800 Nm^2

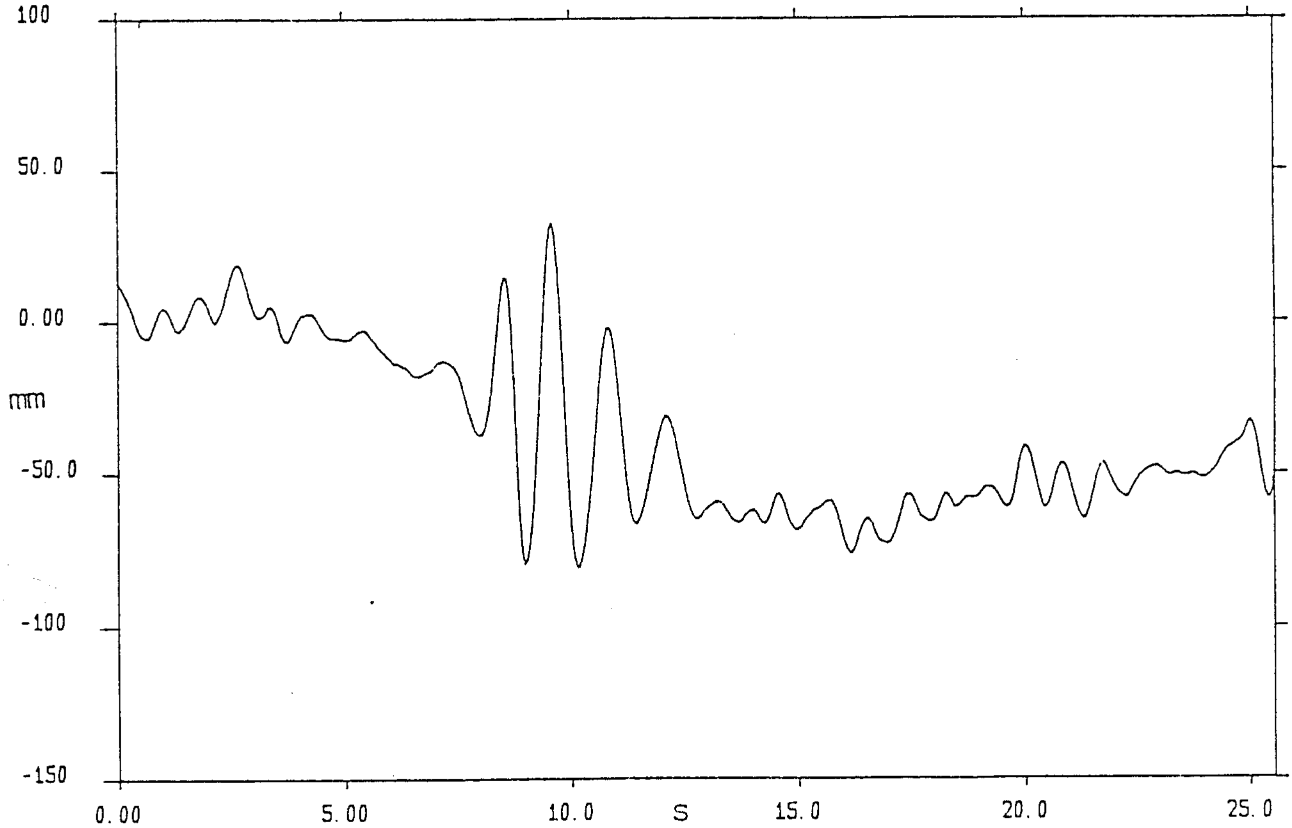

Figure 2.2 Freak wave. Surge motion EI = 800 Nm^2

Figures 2.3 and 2.4 show the effects of the same freak wave on a spine reduced in stiffness to 80 Nm2. Note that both the heave and surge time series show an increase in spine motion. At the lower stiffness, crest-averaging decreases, and local spine motion is more pronounced. In surge, after the passage of the freak wave, the spine returns very nearly to its rest position.

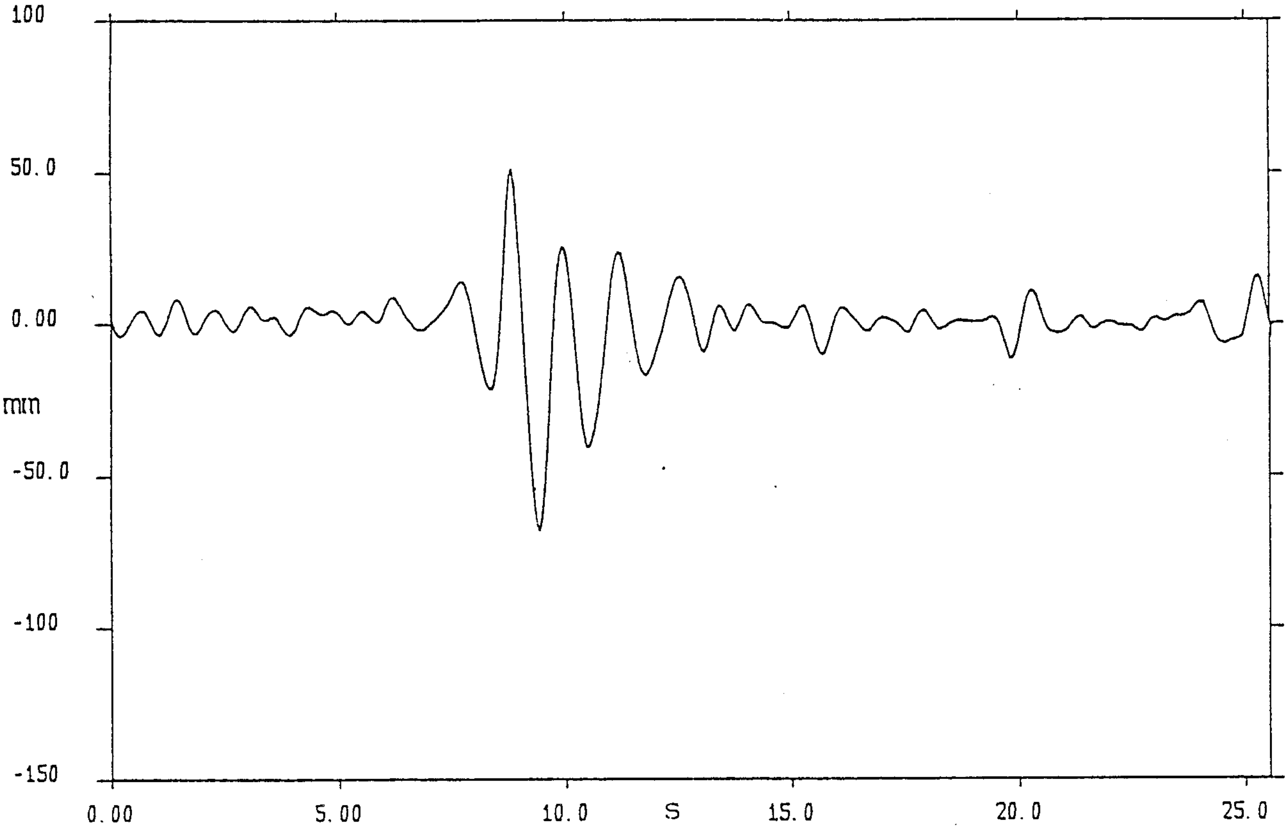

Figure 2.3 Freak wave. Heave motion EI = 80 Nm^2

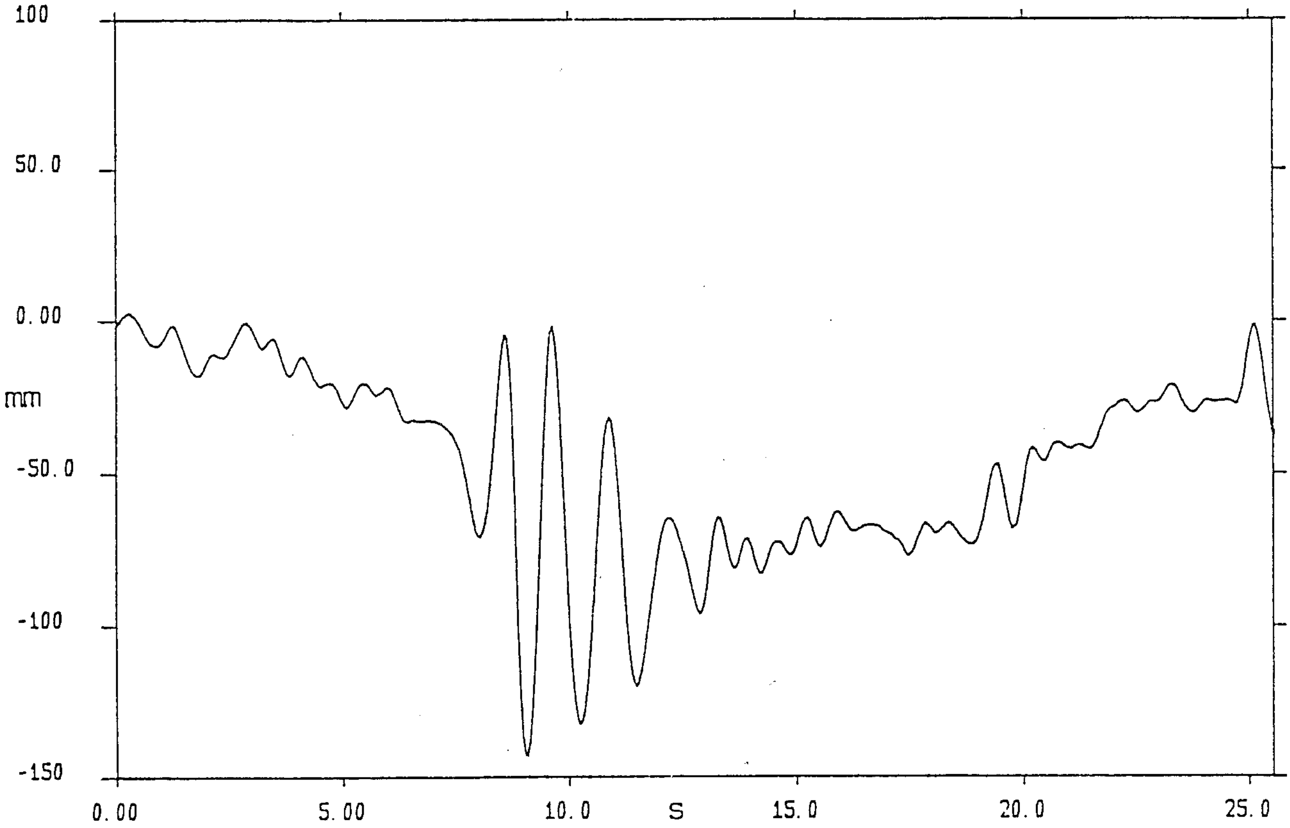

Figure 2.4 Freak wave. Surge motion EI = 80 Nm^2

Figure 2.5 shows the heave signal plotted against surge. The X and Y axes are equally scaled: the graph therefore presents an undistorted view of the motion of the spine in the cross-sectional plane. The arrows indicate the direction of motion. The spine motion due to the freak wave is centred on a point 70 mm aft of the calm-water position, and has a elliptical major radius of about 60 mm.

Surface water particles move in circular orbits, and a floating object which is small compared with the wavelength should do the same. In heave, the change in buoyancy with freeboard produces a restoring force which keeps the spine closely coupled with the water surface. This freeboard effect contributes a negligible 5 Nm2 to spine stiffness, but produces a restoring force to common-mode heave displacement of the spine of about 6000 N/m. The 10 N/m spring provided by all the moorings is comparatively tiny, yet in surge it is the only restoring force to common-mode displacement. The motional response to wave forces of the spring and mass system of the spine and its moorings has a high-pass filter characteristic. In surge, due to the absence of freeboard effects, the cut-off point will be far lower, and consequently, any low frequency response of the spine will be far more apparent.

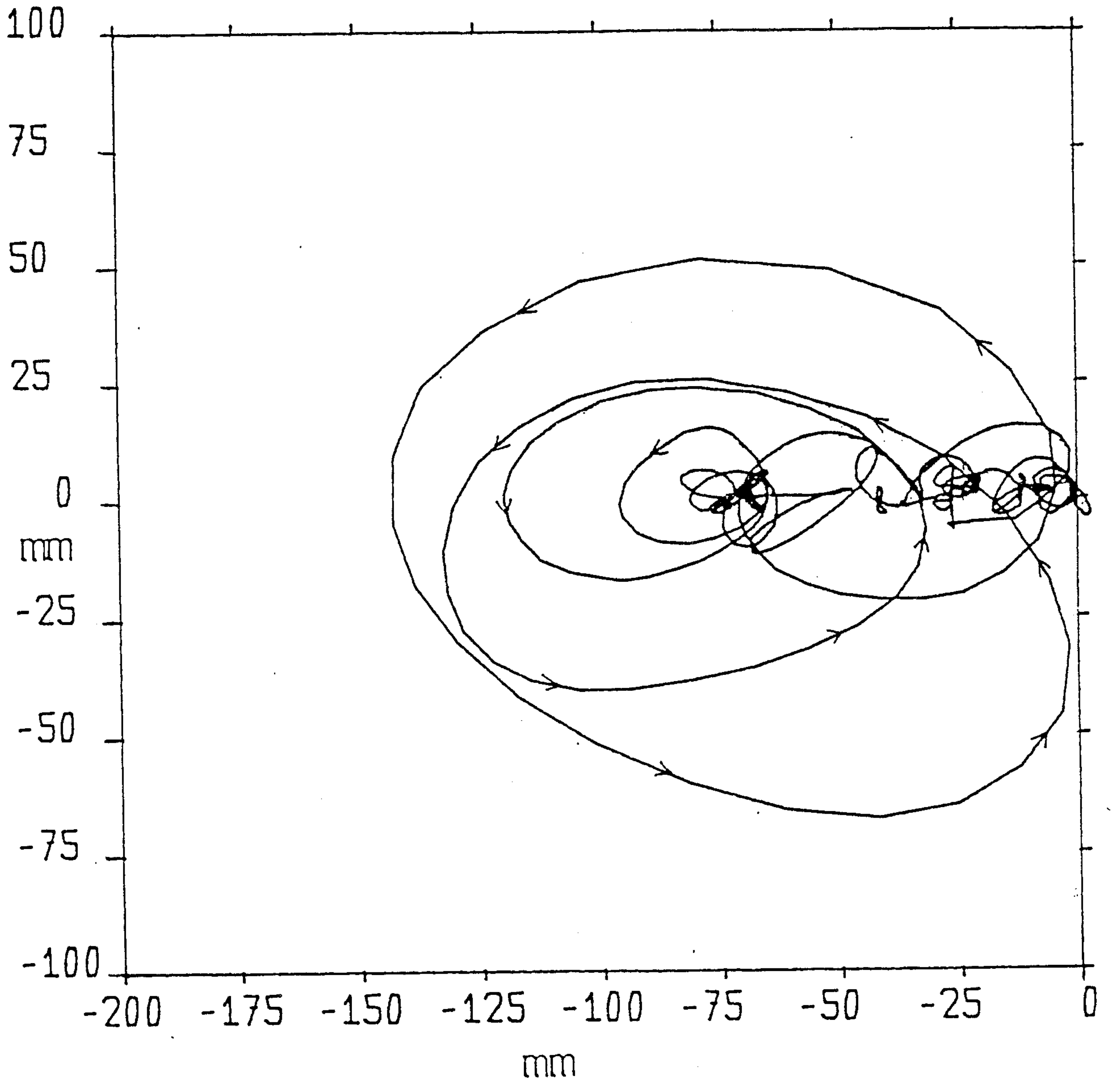

Figure 2.5 Freak wave. X-Y motion EI = 80 Nm^2

The next eight graphs represent the base angle of the mooring lines during passage of the freak wave. All the graphs have the same horizontal and vertical scales.

Figures 2.6, 2.7, 2.8 and 2.9 show the fore and aft angle time series for the two spine stiffnesses. The angles are calculated from the vertical and horizontal forces at the anchor. The angular amplitudes are greater for the low stiffness case, a reasonable result given the greater spine motion; but what is most noticeable is that the aft angular amplitude is several times the fore.

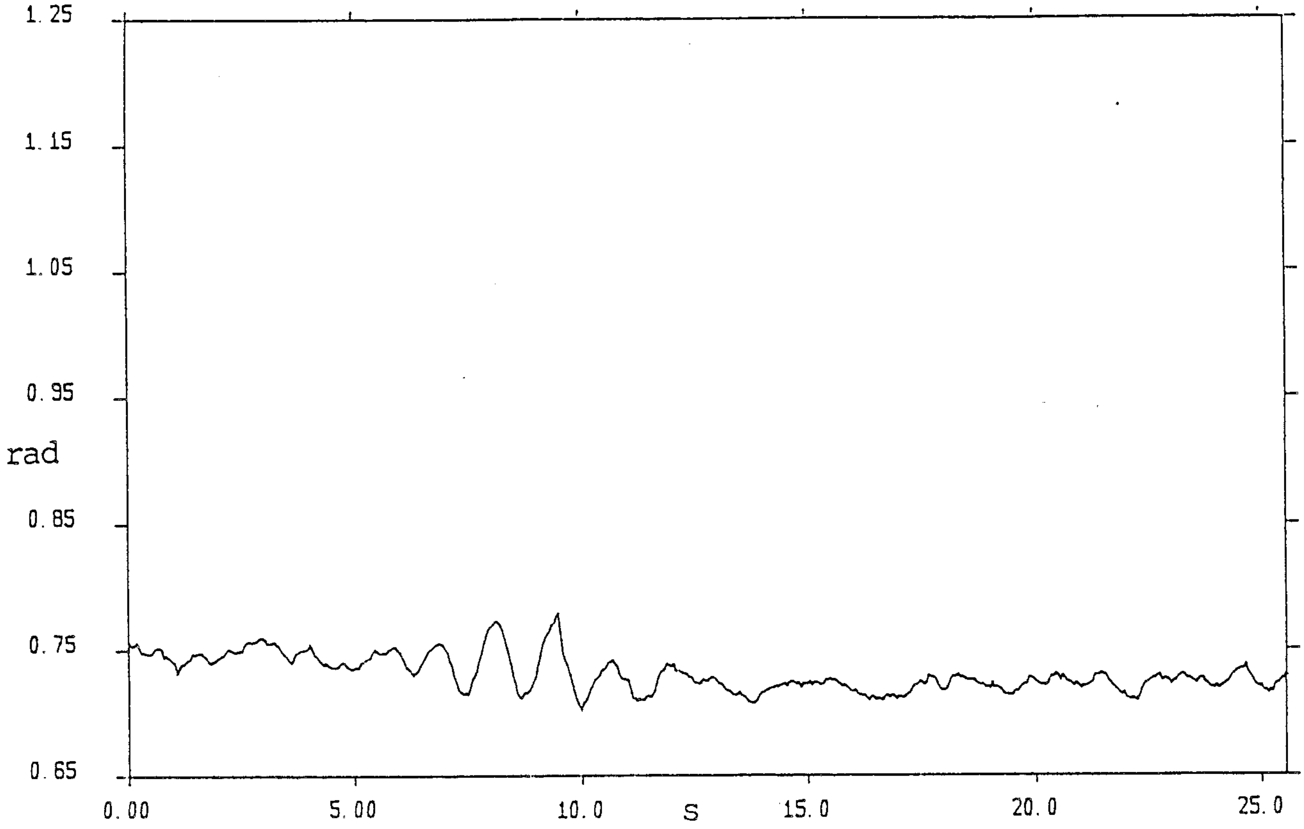

Figure 2.6 Freak wave. Fore base angle EI = 800 Nm^2

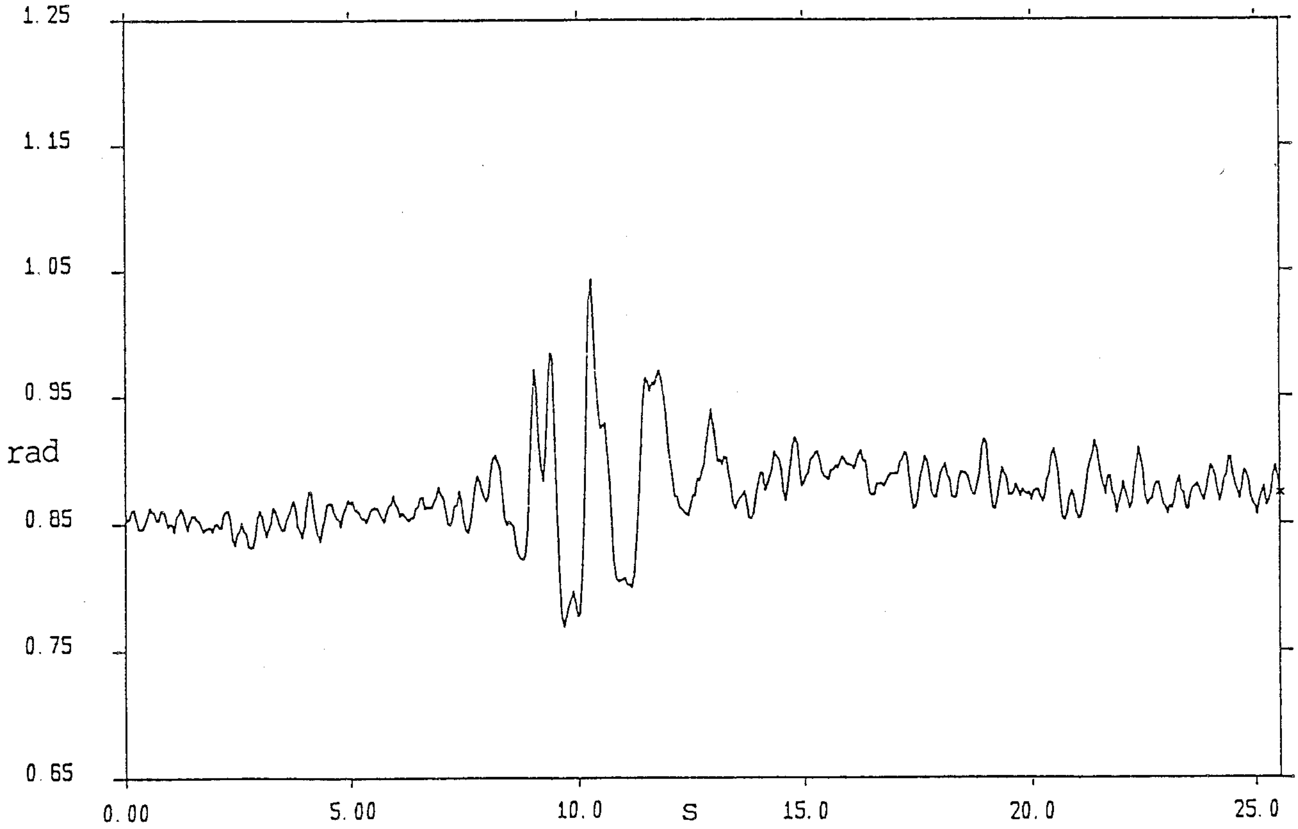

Figure 2.7 Freak wave. Aft base angle EI = 800 Nm^2

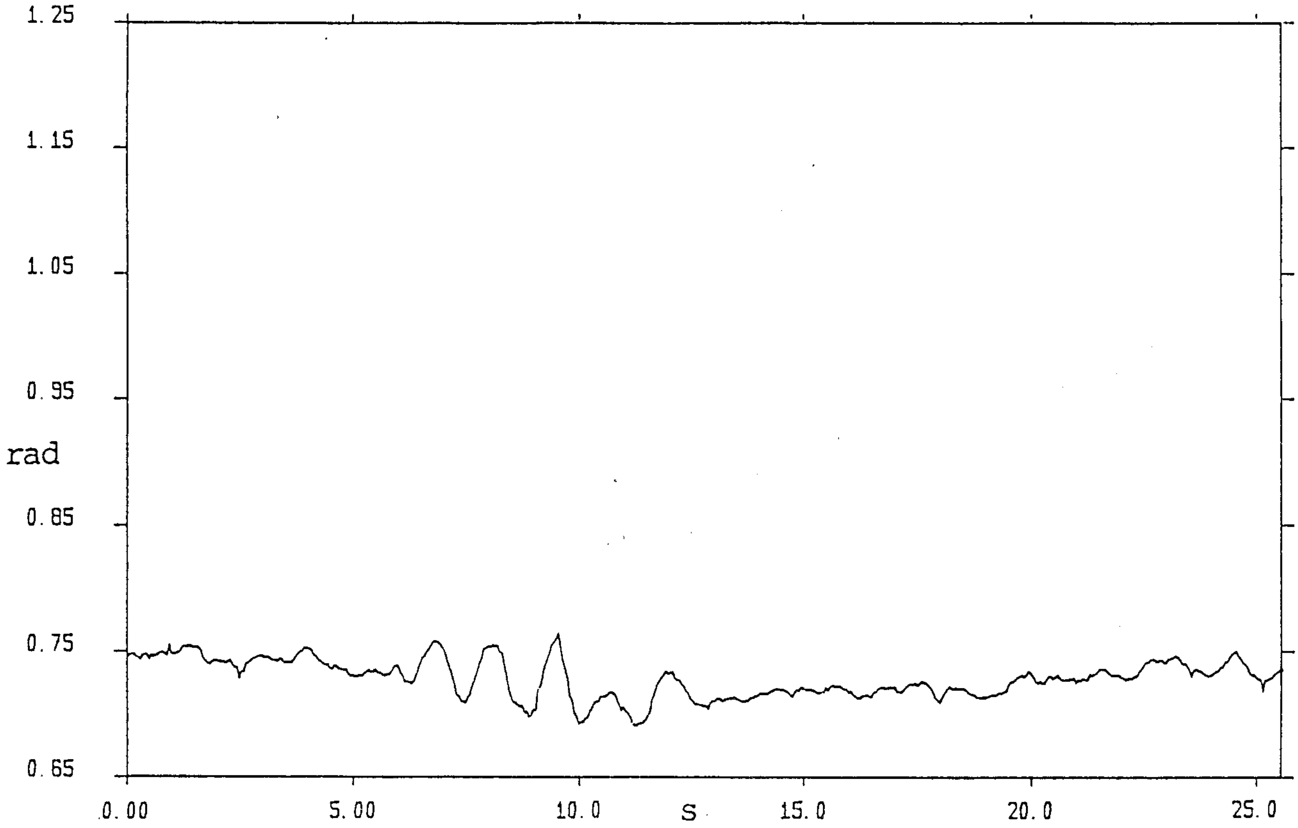

Figure 2.8 Freak wave. Fore base angle EI = 80 Nm^2

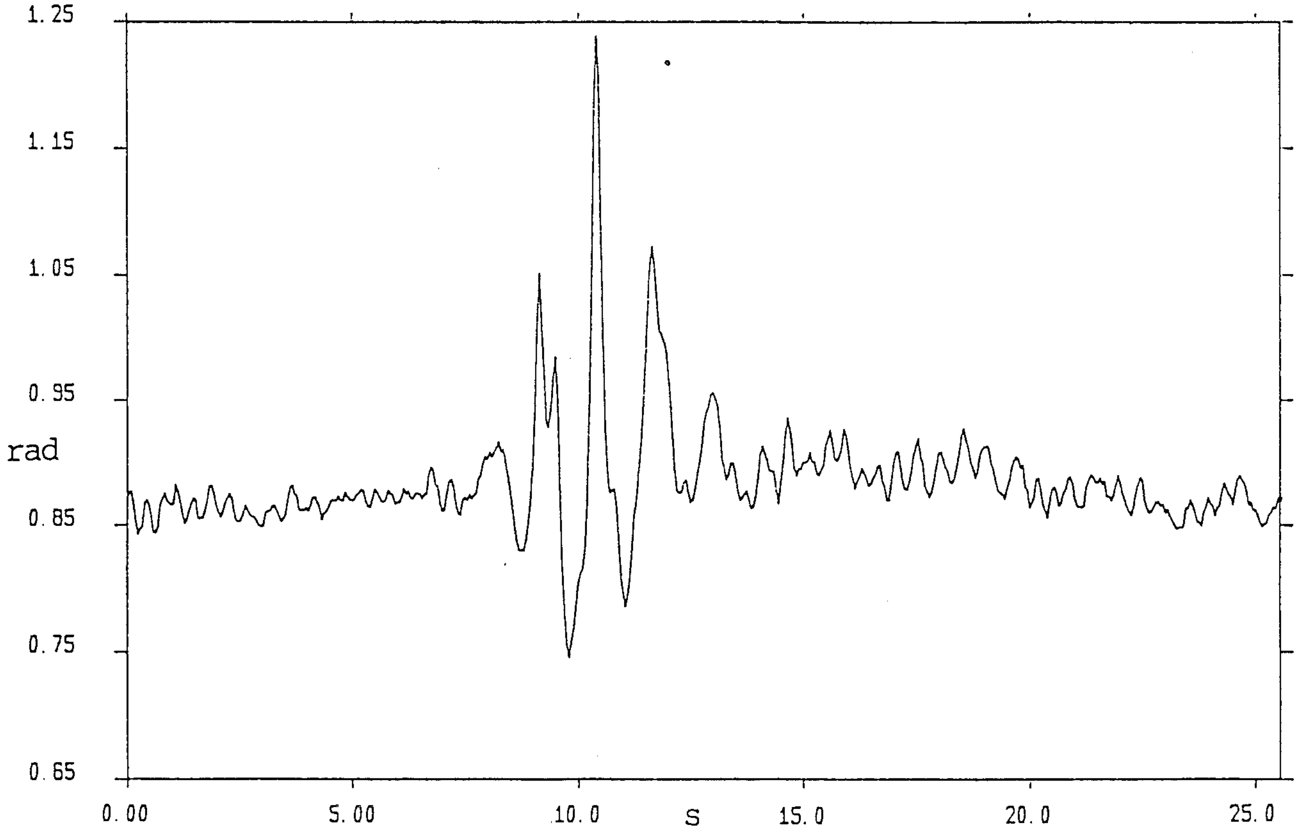

Figure 2.9 Freak wave. Aft base angle EI = 80 Nm^2

It is helpful to construct time series of the expected angle of the fore and aft gauges, given the algorithm for their geometry and the recorded instantaneous position of the spine. For the low stiffness case this yields the time series shown in figures 2.10 and 2.11. The traces are similar in appearance, though of course reversed in phase. The aft trace is slightly larger, partly because the aft line is longer, and partly because the angular response to linear motion is greater as the line compresses. Comparing these calculated traces with figures 2.8 and 2.9 one can see that they are smaller than those actually measured, substantially so for the aft gauge. It is also clear that the appearance of the freak wave part of the trace occurs sooner on the measured fore trace, and later on the aft trace than predicted by the spine motion. It would seem that the floats are being acted on by the freak wave itself in addition to the forces they receive due to the motion of the spine. It is interesting that the mean values of the fore and aft predicted angles are both smaller than the mean values of either fore or aft measured angles. This ´rising float´ effect is encountered again in the experiments with the South Uist 46 spectra.

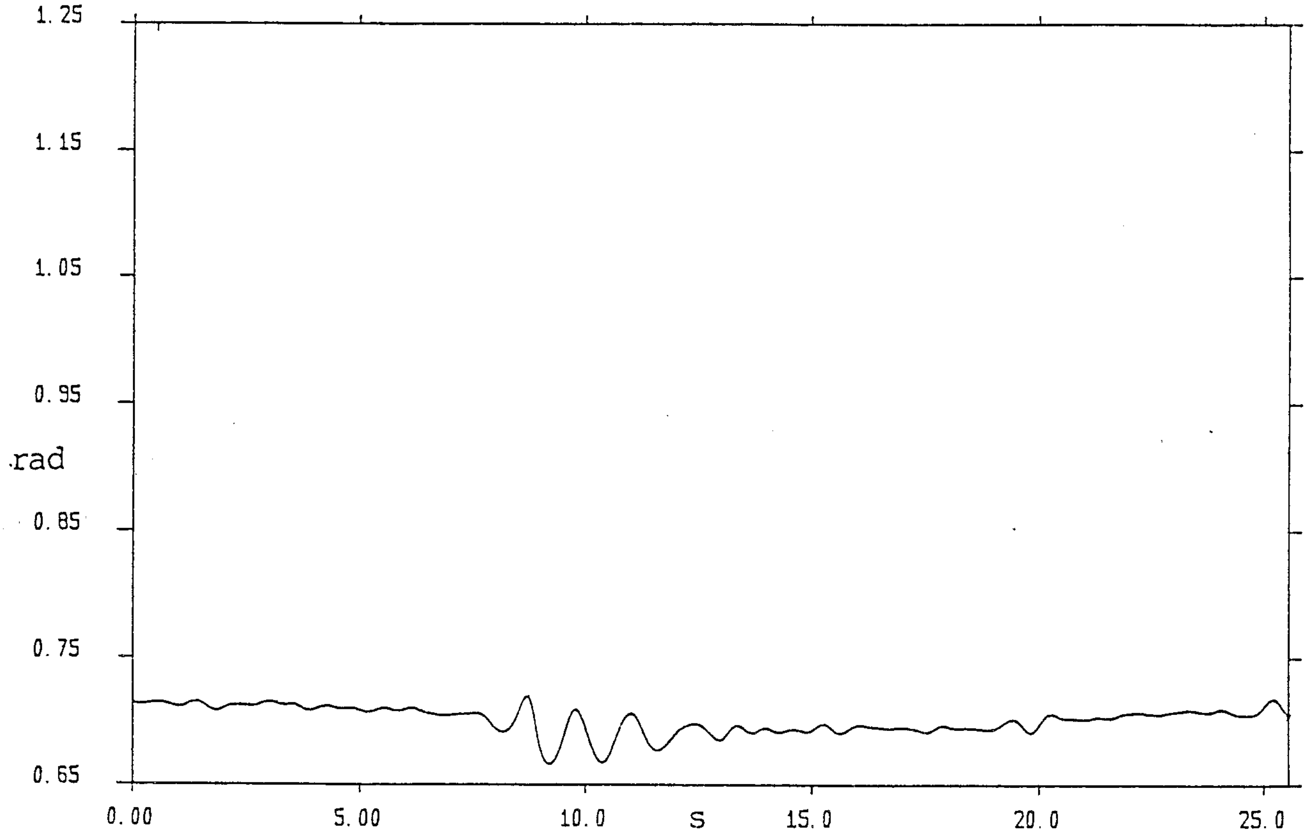

Figure 2.10 Freak wave. Predicted fore base angle EI = 80 Nm^2

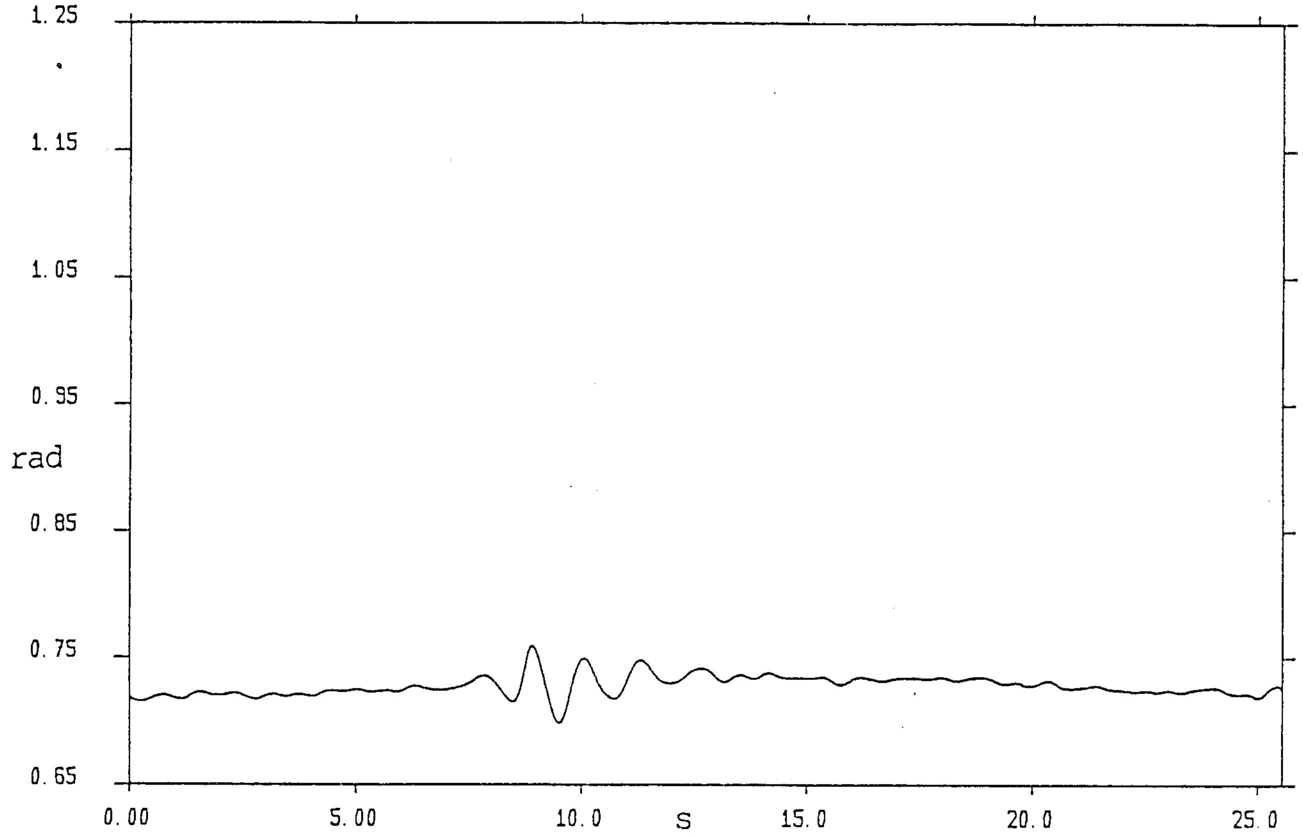

Figure 2.11 Freak wave. Predicted aft base angle EI = 80 Nm^2

To investigate wave action on the floats, we removed the spine and connected its mooring lines to a fixed point at the normal spine position. The freak wave was run again, and the fore and aft angle time series are shown in figures 2.12 and 2.13. They are of very similar size and appearance, but displaced from each other in time due to their 4 meter separation in space.

It is very interesting that the angular motion in this case is actually larger than that predicted due to spine motion (shown in figures 2.10 and 2.11). Note also that the first peak due to the freak wave in the fore time series occurs at the same time (7 seconds) as the first peak in figure 2.8, where the mooring was connected to the spine. The two peaks are of very similar size and shape, and since the predicted trace of figure 2.10 shows no contribution at this time from spine motion, we infer that the motion is due simply to wave action on the floats.

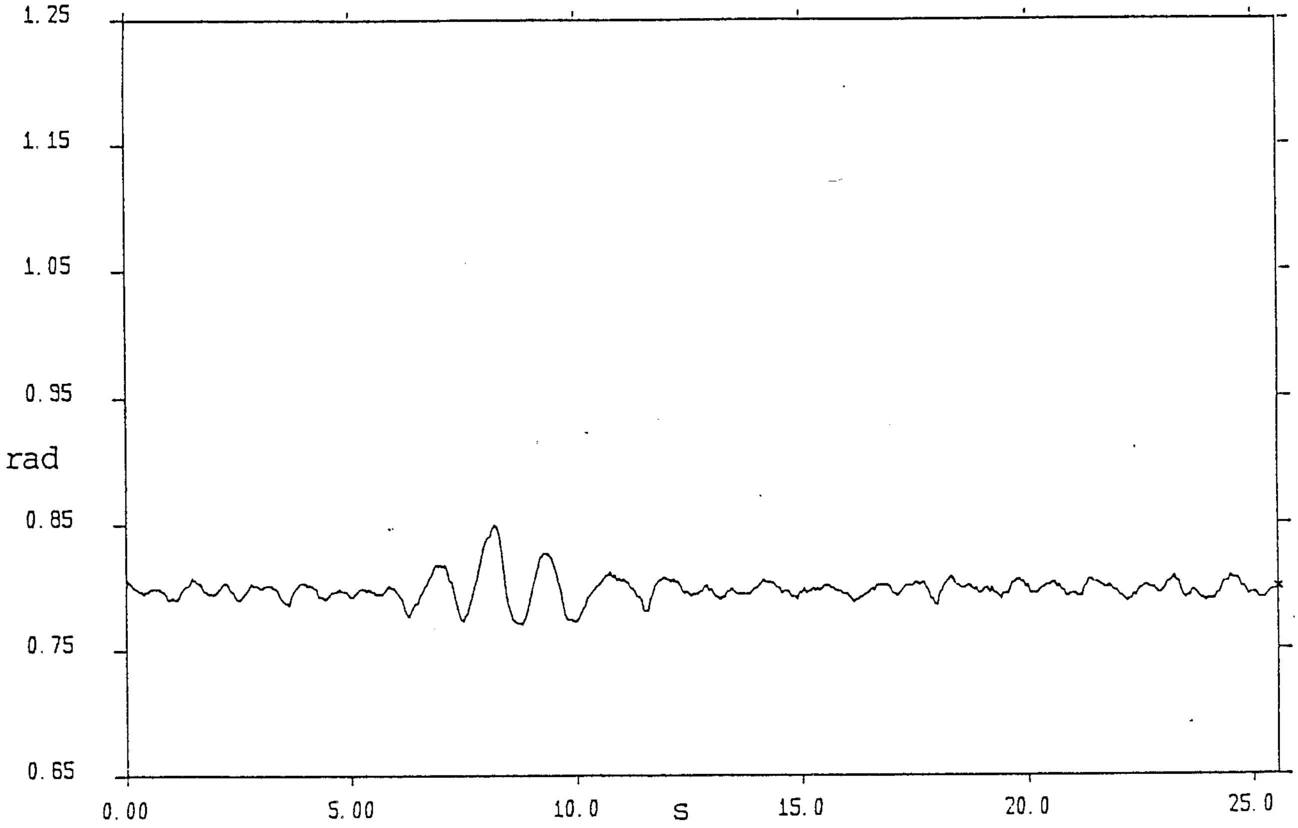

Figure 2.12 Freak wave. Fore base angle: fixed mooring

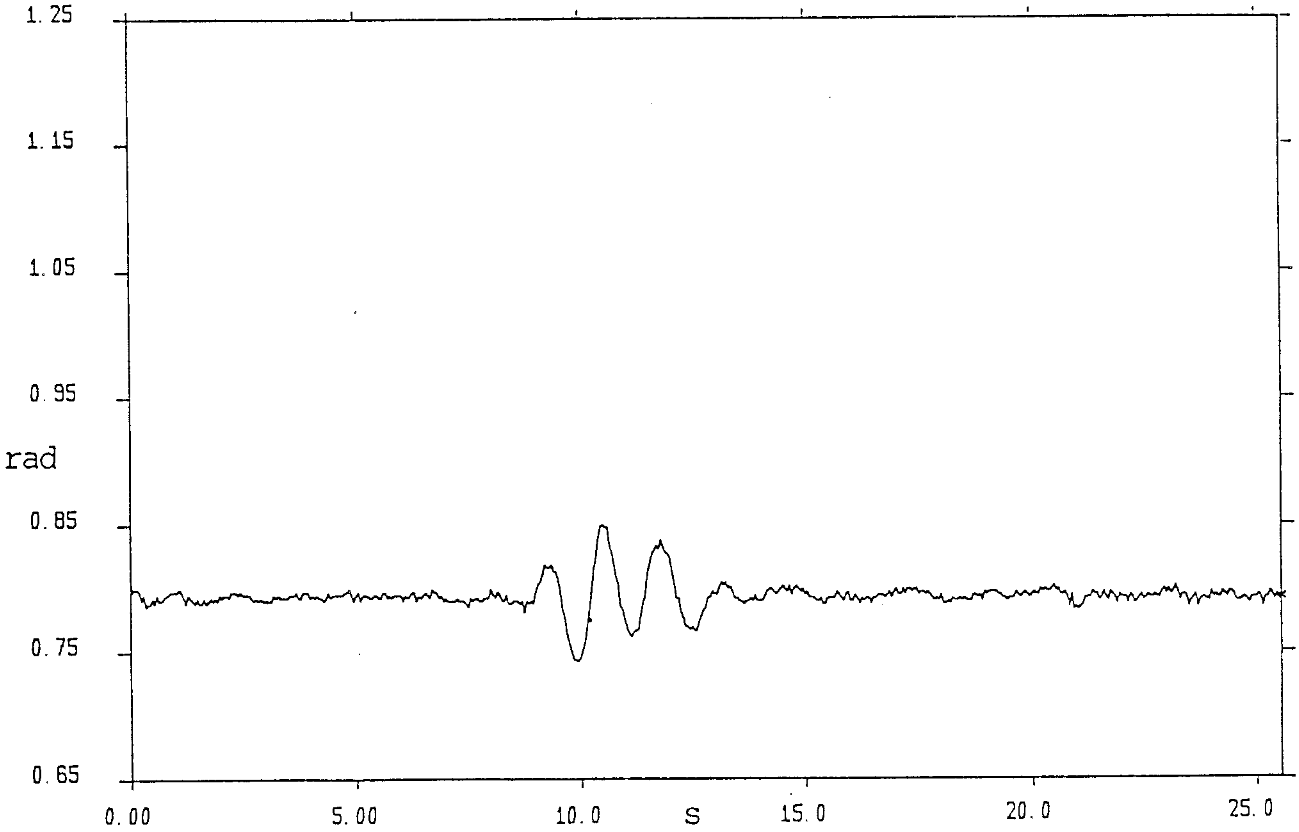

Figure 2.13 Freak wave. Aft base angle: fixed mooring

In figures 2.14 and 2.16 the heave motion of the fore and aft floats is plotted and may be compared to the elevation of the water surface plotted in figure 2.15. The floats move about a third as much as the water at the surface. Wave motion in water decreases exponentially with depth at a rate which increases with frequency; if the sum of the components (each reduced appropriately) is calculated, water motion at the depth of the float is about one seventh that at the surface. The floats are therefore moving about twice as much as the water around them.

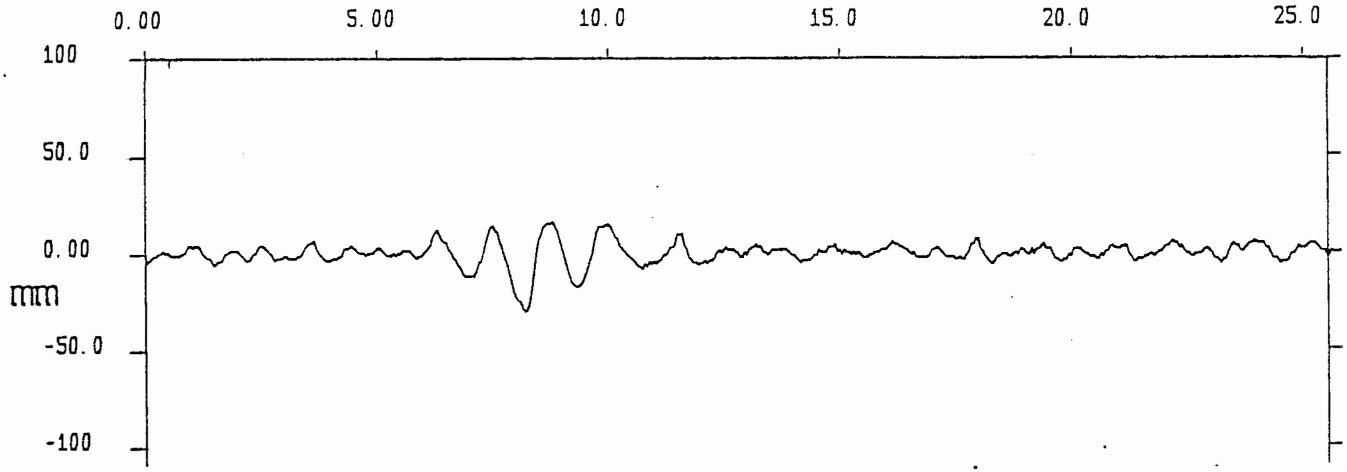

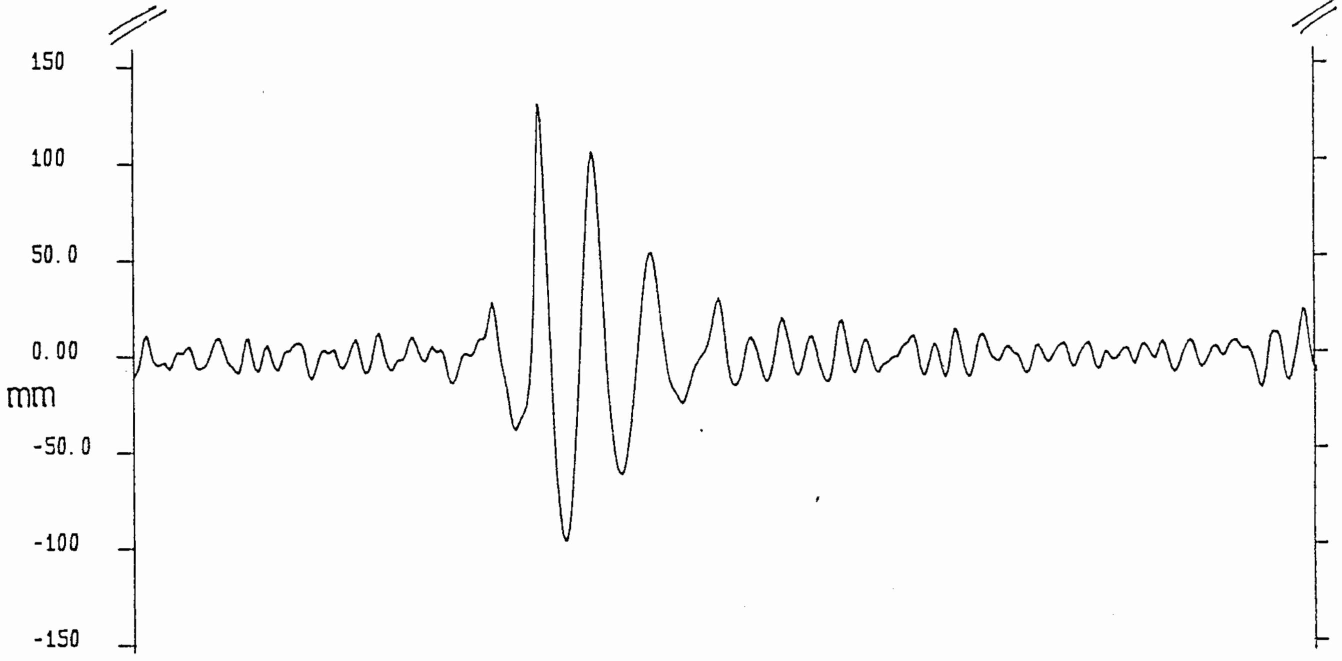

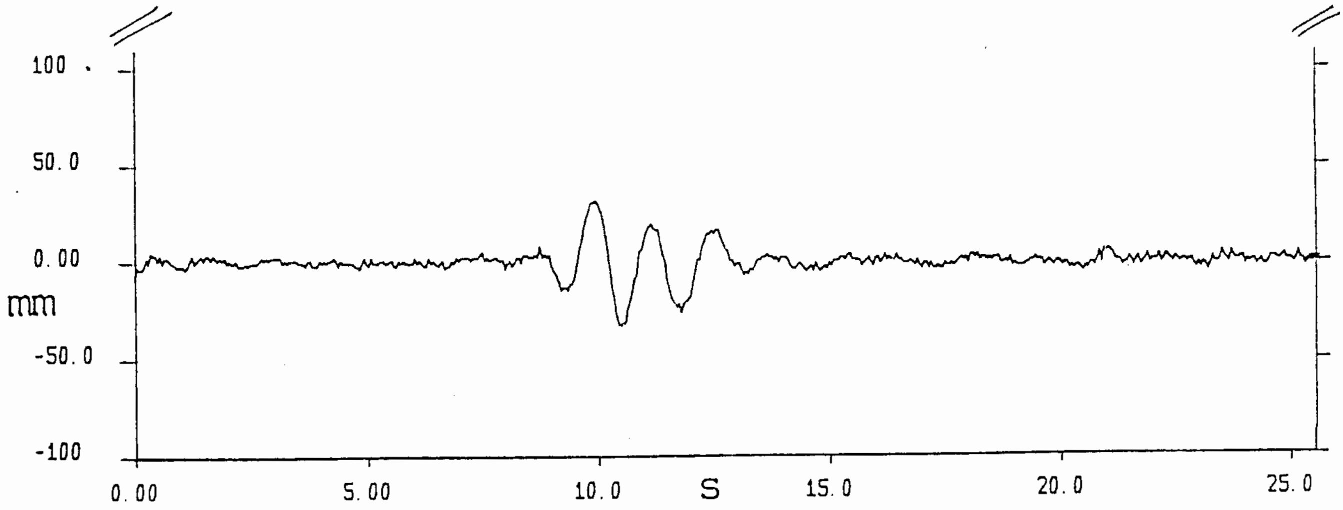

Figure 2.14 Freak wave. Fore float heave motion

Figure 2.15 Freak wave. Water surface elevation

Figure 2.16 Freak wave. Aft float heave motion

Tension time series for the base section of the mooring lines are shown on the following pages. All the graphs have the same horizontal and vertical scales.

Figures 2.17 and 2.18 show the tension when the spine has a stiffness of 800 Nm2. The variation is greater in fore than in aft - the opposite of the case with the angle time series shown in figures 2.6 and 2.7. This is a result of the increase in tension and decrease in angle of the mooring when extended, as explained in Appendix C: the fore mooring is at greater stretch than the aft, and so its tension variations are higher and its angle variations lower.

Figures 2.19 and 2.20 show the equivalent series for the spine at a stiffness of 80 Nm2. The spine motion is greater than at the higher stiffness, and consequently the tension variations are higher too. It is very noticeable that the difference between the fore and aft traces is only of the order of 25% - far less than the difference between the fore and aft angle time series.

Figures 2.21 and 2.22 show the tension variation for the fixed mooring. They are about half the amplitude of those in 2.19 and 2.20, further corroboration of the importance of direct wave loading on the mooring in contributing to mooring loads.

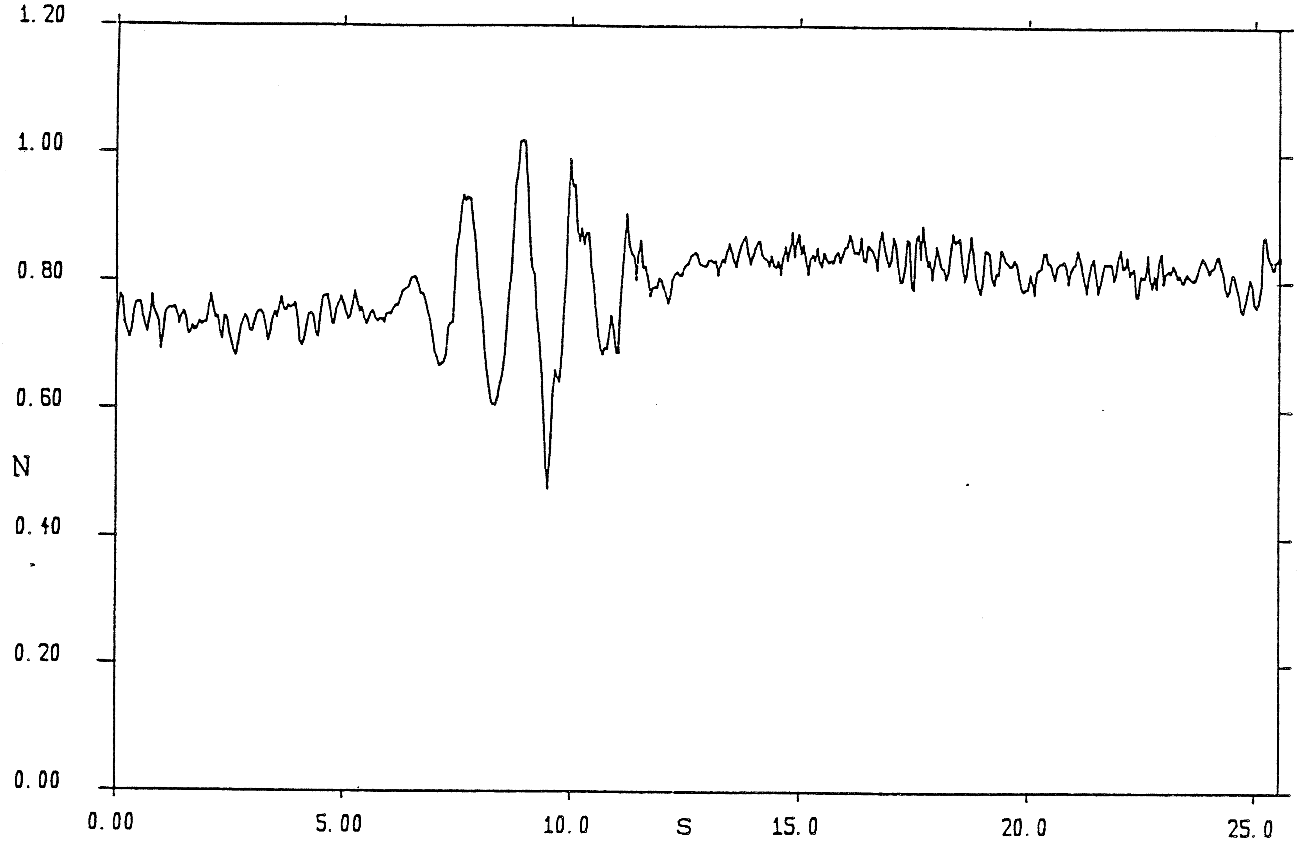

Figure 2.17 Freak wave. Fore base tension EI = 800 Nm^2

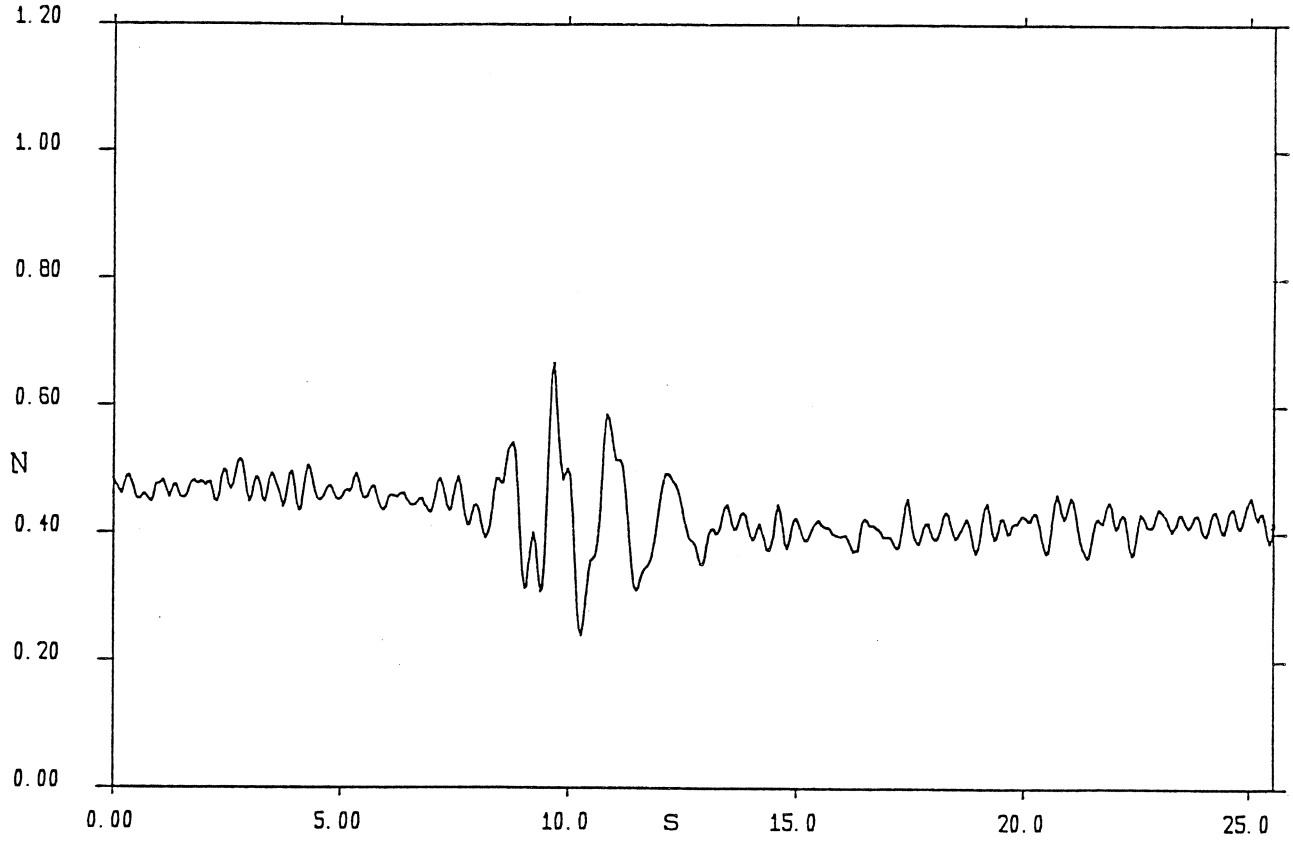

Figure 2.18 Freak wave. Aft base tension EI = 800 Nm^2

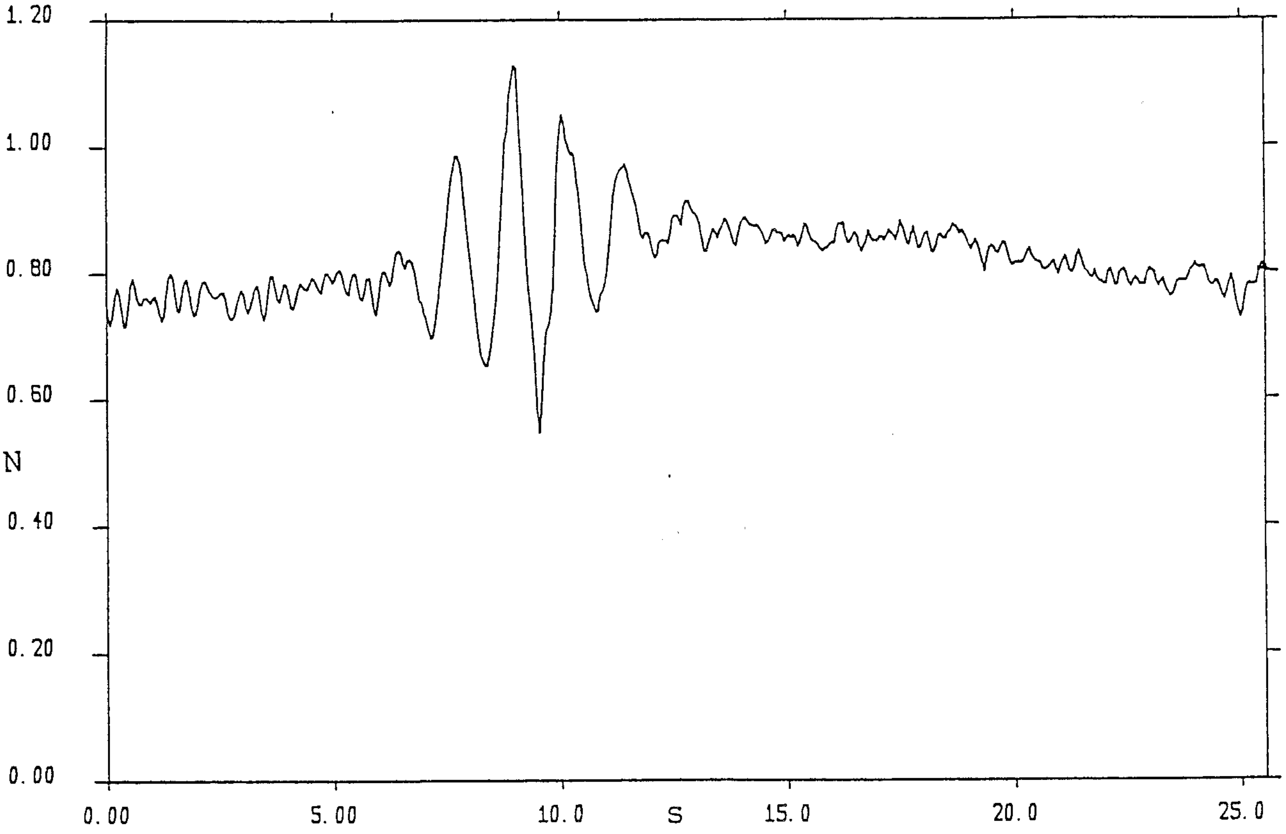

Figure 2.19 Freak wave. Fore base tension EI = 80 Nm^2

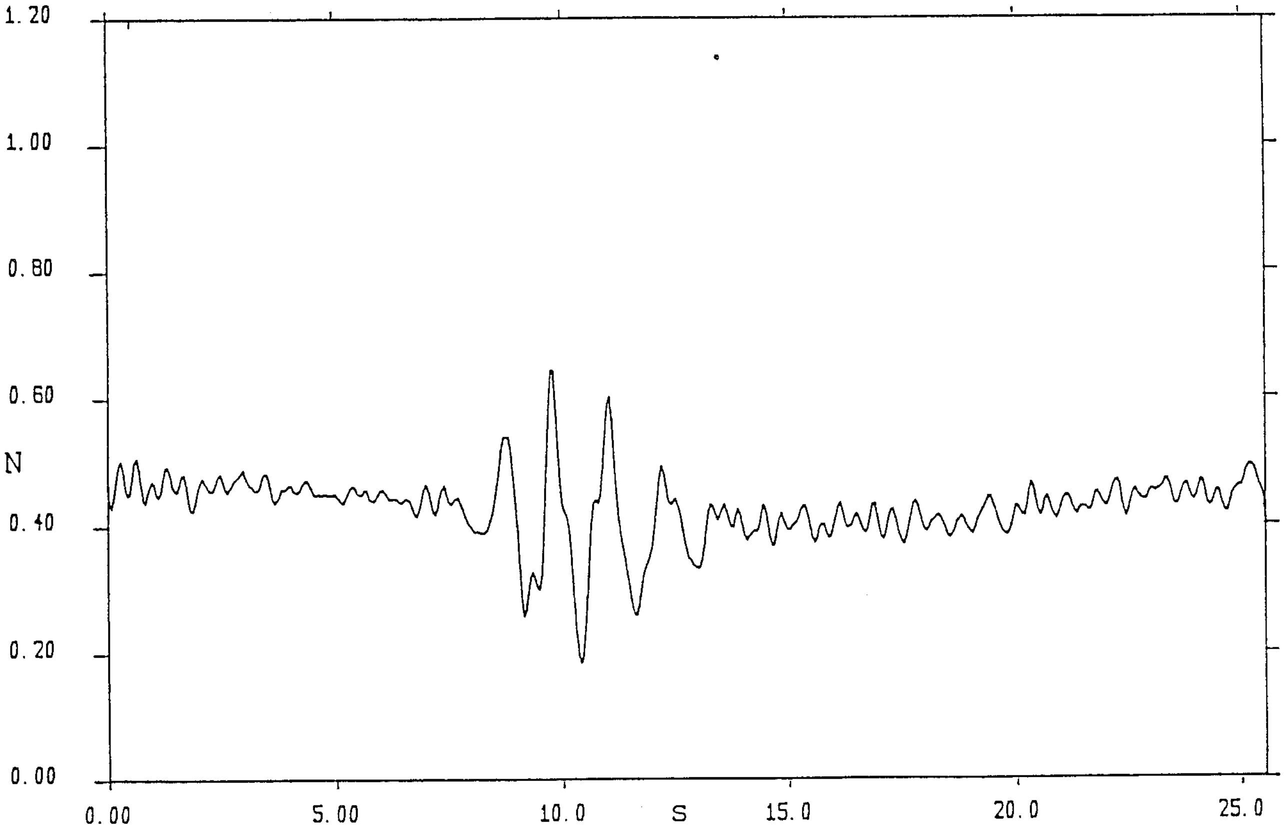

Figure 2.20 Freak wave. Aft base tension EI = 80 Nm^2

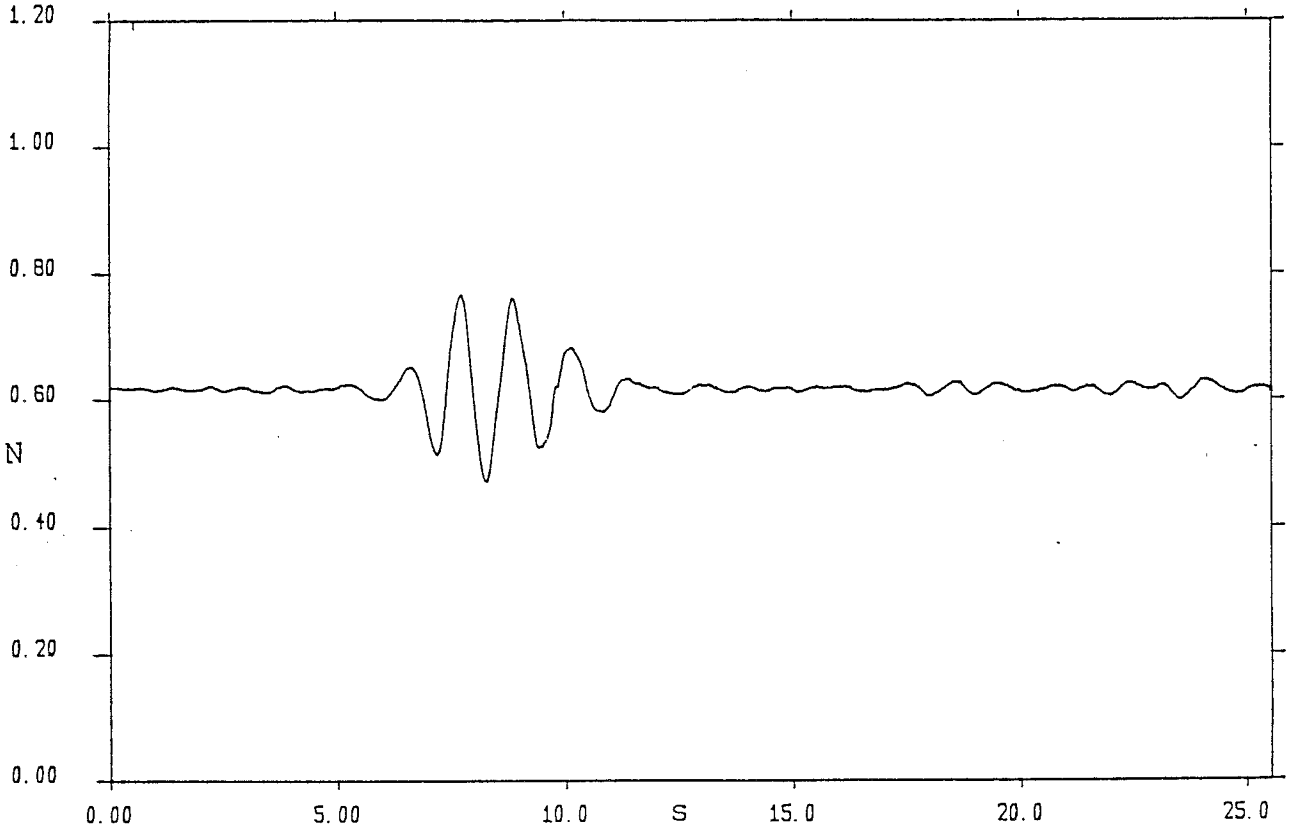

Figure 2.21 Freak wave. Fore base tension: fixed mooring

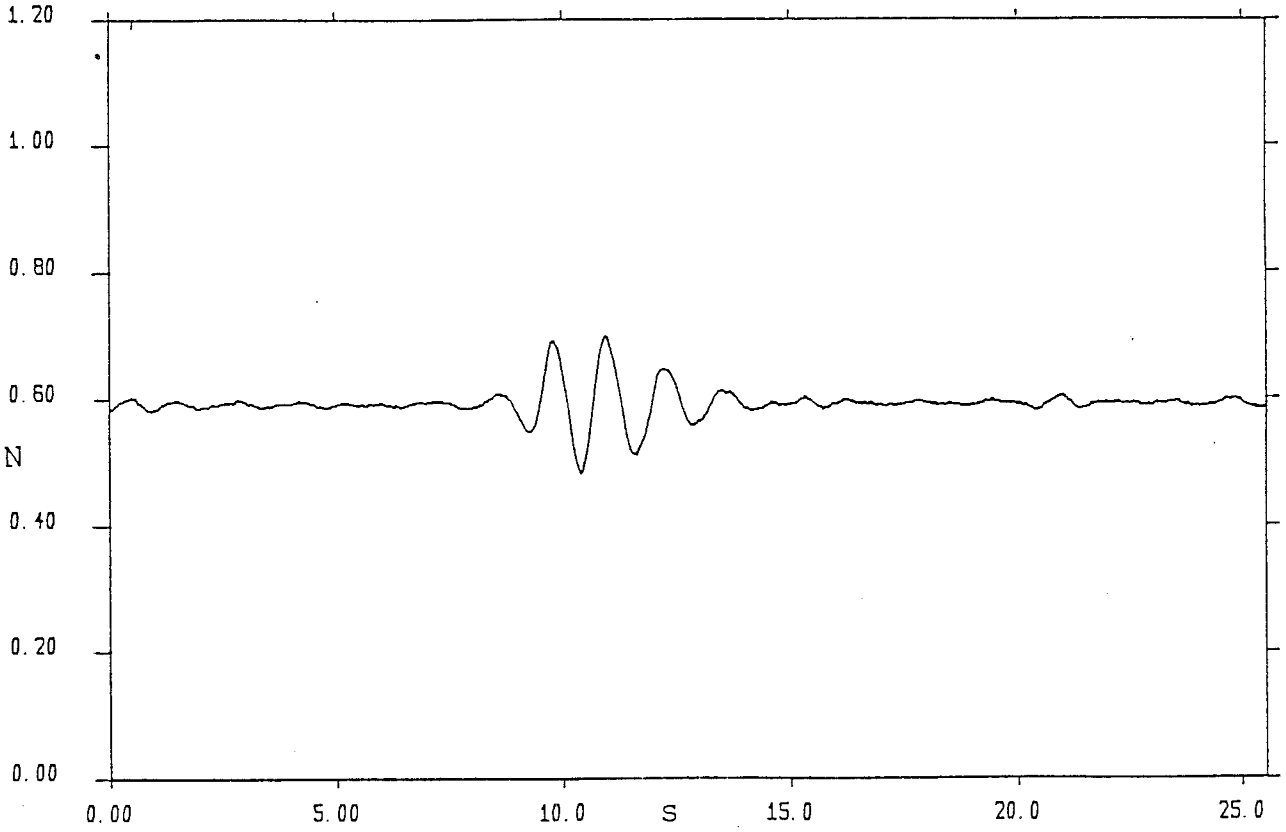

Figure 2.22 Freak wave. Aft base tension: fixed mooring

SECTION 3 TESTING IN THE SOUTH UIST SPECTRA

Having got a feel for how the moorings behave in the extreme conditions of a freak wave, we turned to more moderate sea states. We used our standard set of ´South Uist 46 spectra´.

Table 3.1 ahows their IOS number, Hrms, and weighted contribution to annual statistics. Note that the weightings do not add to 100%. The sea states excluded are mostly those of low power. Full details of the selection of the 46 spectra are given in an appendix in the 1984 Long Spine Report.

Figure 3.1 shows a ´pox plot´ of the 46 spectra; figure 3.2 is the equivalent 3-d representation. Both figures are reproduced from the 1984 report.

TABLE 3.1 CHARACTERISTICS OF THE SOUTH UIST 46 SPECTRA

This is a set of sea states chosen by the Consultants to be representative the set of 399 spectra specified by the Institute of Oceanographic Science. For each spectrum we give the IOS number; the Hrms of the model sea in mm, at 107.7 scale; and the equivalent percentage weighting over one year.

IOS NUMBER	HRMS mm	WEIGHT %
089	3.8	1.10
108	4.3	1.10
112	4.2	0.83
122	3.4	1.10
154	5.5	2.21
168	5.4	1.93
171	5.6	5.24
177	5.4	1.66
180	4.9	1.66
200	4.8	2.48
201	4.9	5.80
210	4.6	5.52
212	3.5	0.83
218	4.9	2.48
220	8.0	1.10
223	5.2	1.38
228	6.9	0.83
238	6.7	1.66
241	4.6	1.10
242	6.5	1.10
244	7.3	4.14
249	7.3	0.83
267	5.7	1.10
268	6.7	0.55
280	6.5	1.93
291	9.3	1.38
292	8.9	1.93
294	8.3	0.83
318	6.9	1.66
319	7.6	2.21
322	10.8	1.10
324	9.7	0.83
336	12.2	0.83
346	10.1	1.10
347	10.7	0.55
352	9.5	0.55
355	10.2	0.55
359	10.4	3.04
360	13.5	0.83
366	12.2	0.83
371	14.3	1.38
377	13.8	1.38
378	12.6	0.55
381	15.8	0.55
388	17.1	1.83
391	16.7	1.10
		74.67 %

the 46 SPECTRA
'a' set

IOS data adjusted for 100m water depth
and rescaled at 1/108

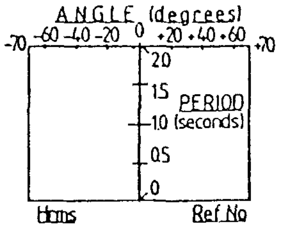

POX PLOTS
SEA SET: SU'a'

The '46 spectra', based on buoy data off the coast of South Uist, with directions synthesised from wind records. The 46 are selected to be representative of all seasons, but their weightings are not equal. For the 'a' set, the normal to the wavemaker axis represents a compass bearing of 260 degrees with the model parallel to the wavemakers. 13 of the 46 spectra are poorly represented by the 'a' version, and the 'b' or 'c' version is a closer match.

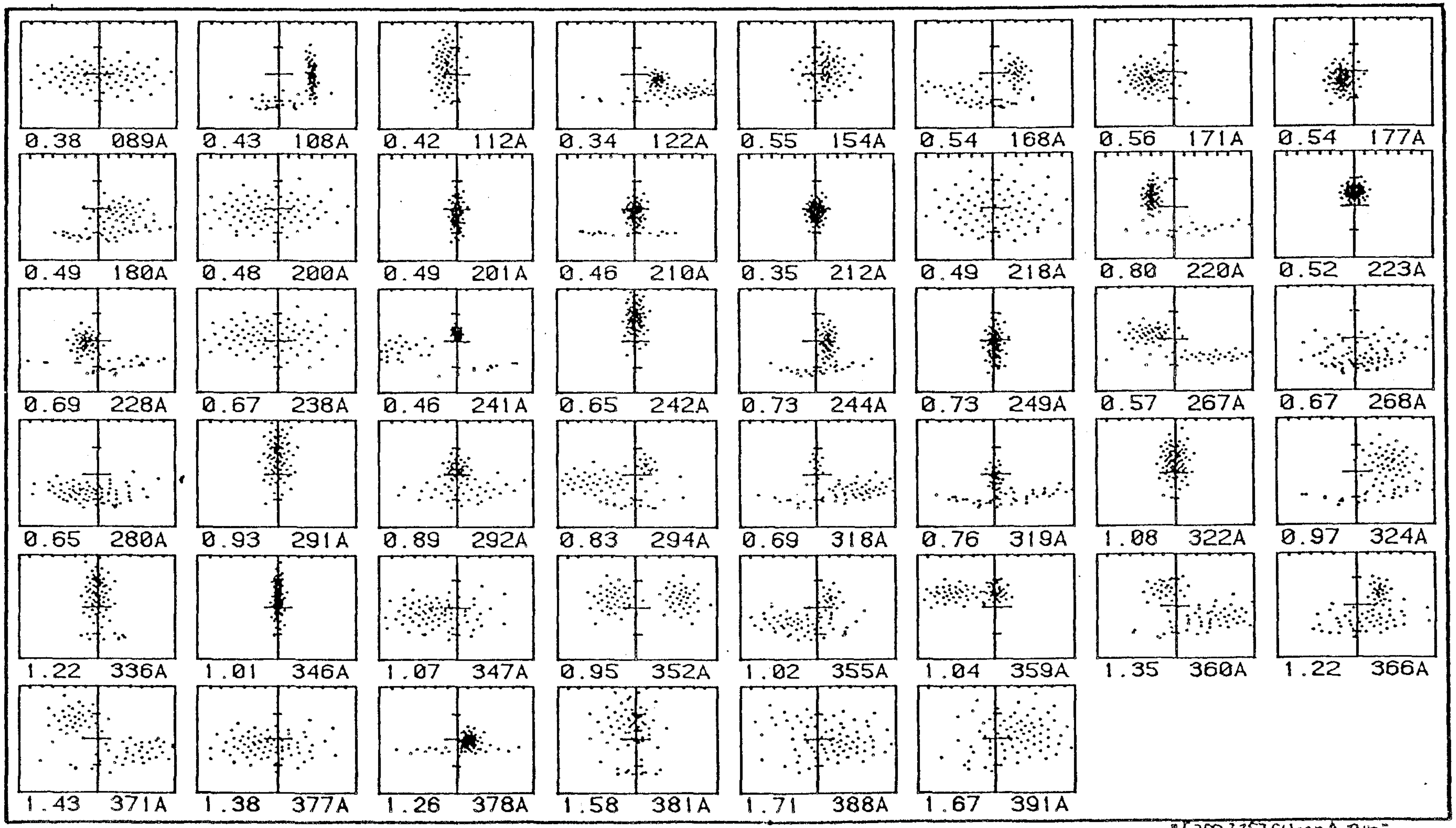

"[300,325]SUnnnA.TNK"

Nominal Westerly seas

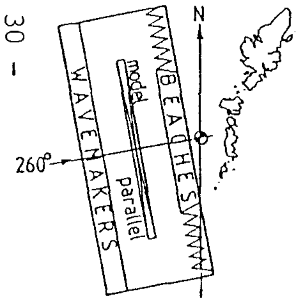

Figure 3.1 South Uist 46 Spectra: Pox plot

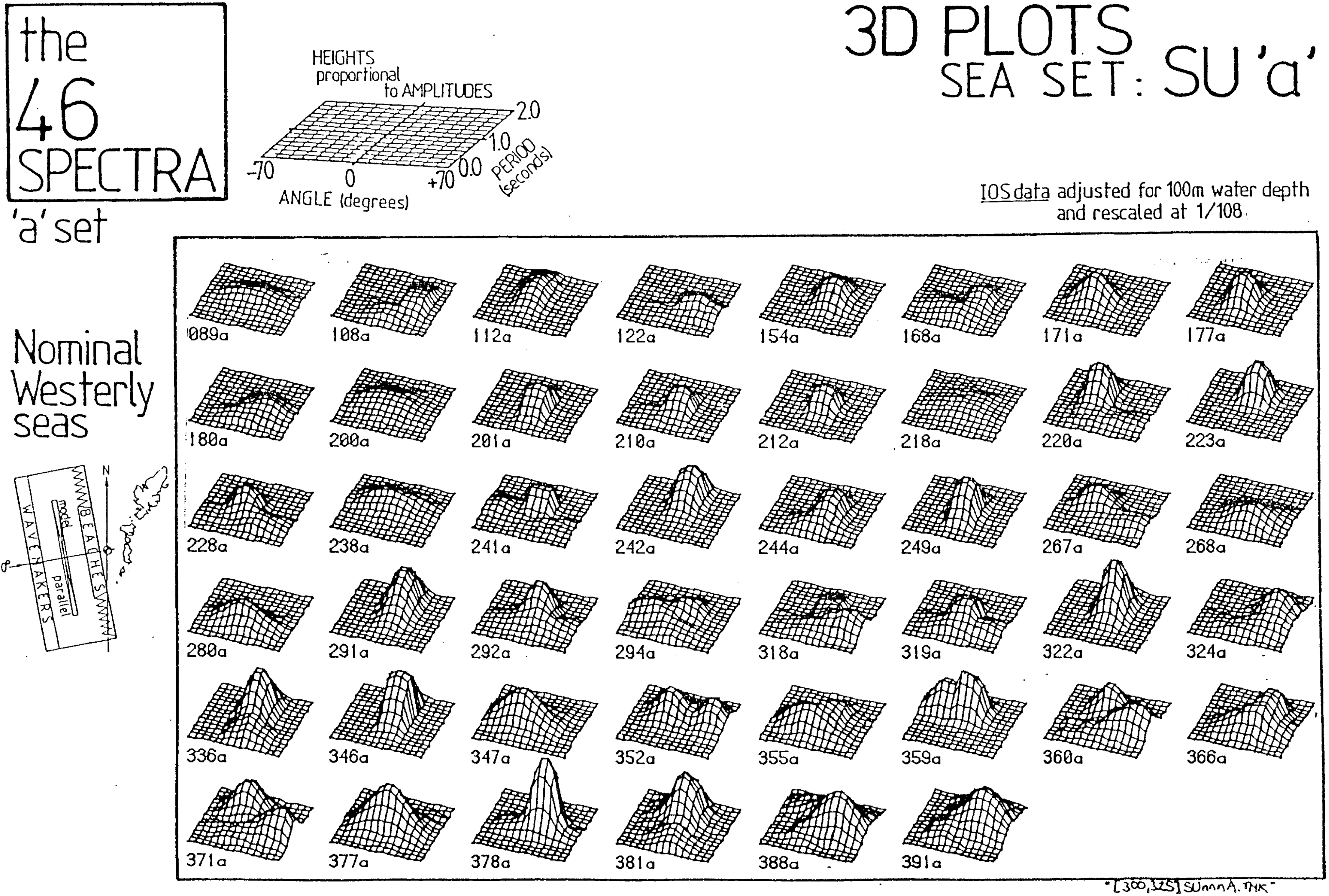

Figure 3.2 South Uist 46 Spectra: 3-D plot

For the tests in this Section we chose the low spine stiffness of 80 Nm2, because it puts greater demands on the moorings.

Both the anchor and position gauges were recorded, at a sampling frequency of 20 Hz, for 51.2 seconds.

Figures 3.3 and 3.4 show the heave and surge position time series for the 46 tests. Though the graphs cover different ranges, they have been drawn to the same scale, so that they may be directly compared. The scale was chosen to accomodate the largest excursion in the set of experiments; so inevitably in some seas, and particularly in heave, the excursions are very small.

In general, the 46 spectra show an increase in Hrms with IOS number, and the time series for the resulting heave and surge spine motion show a similar increase. There are also, particularly in surge, a number of other interesting features which are unrelated to Hrms. These become more apparent in the following graphs.

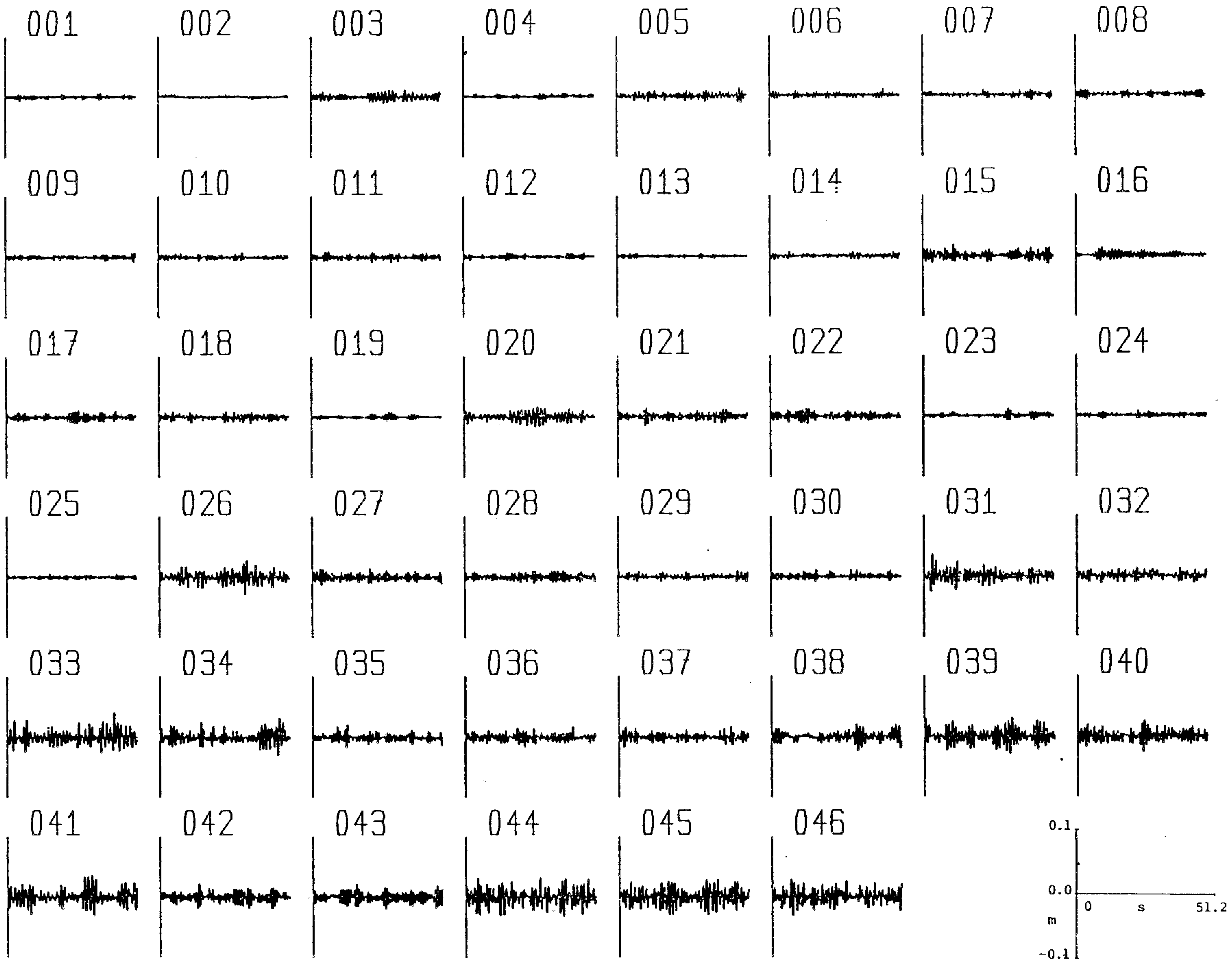

Figure 3.3 46 Spectra. Heave motion

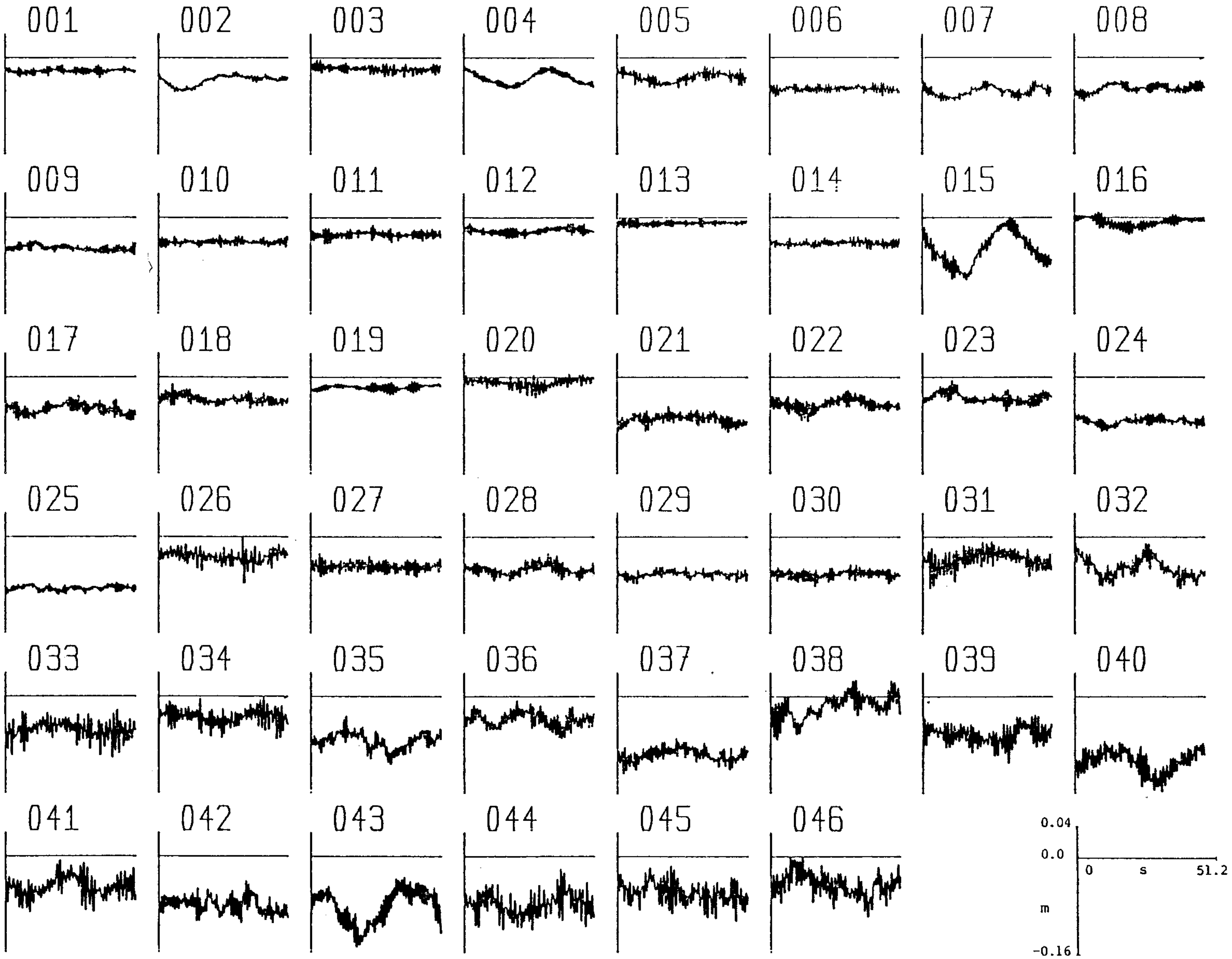

Figure 3.4 46 Spectra. Surge motion

In figures 3.5 and 3.6 the motion time series have been normalized by dividing the Hrms of the respective sea-state.

Examination of the heave time series shows that, with a few exceptions, the amount of normalized spine motion does not vary much.

Comparison of these time series with the sea-state plots in figures 3.1 and 3.2 show that the cases of above-average normalized motion tend to be produced by beam seas with small angular spreading. These circumvent the crest-averaging property of the spine, generating a large amount of common-mode motion of the spine sections.

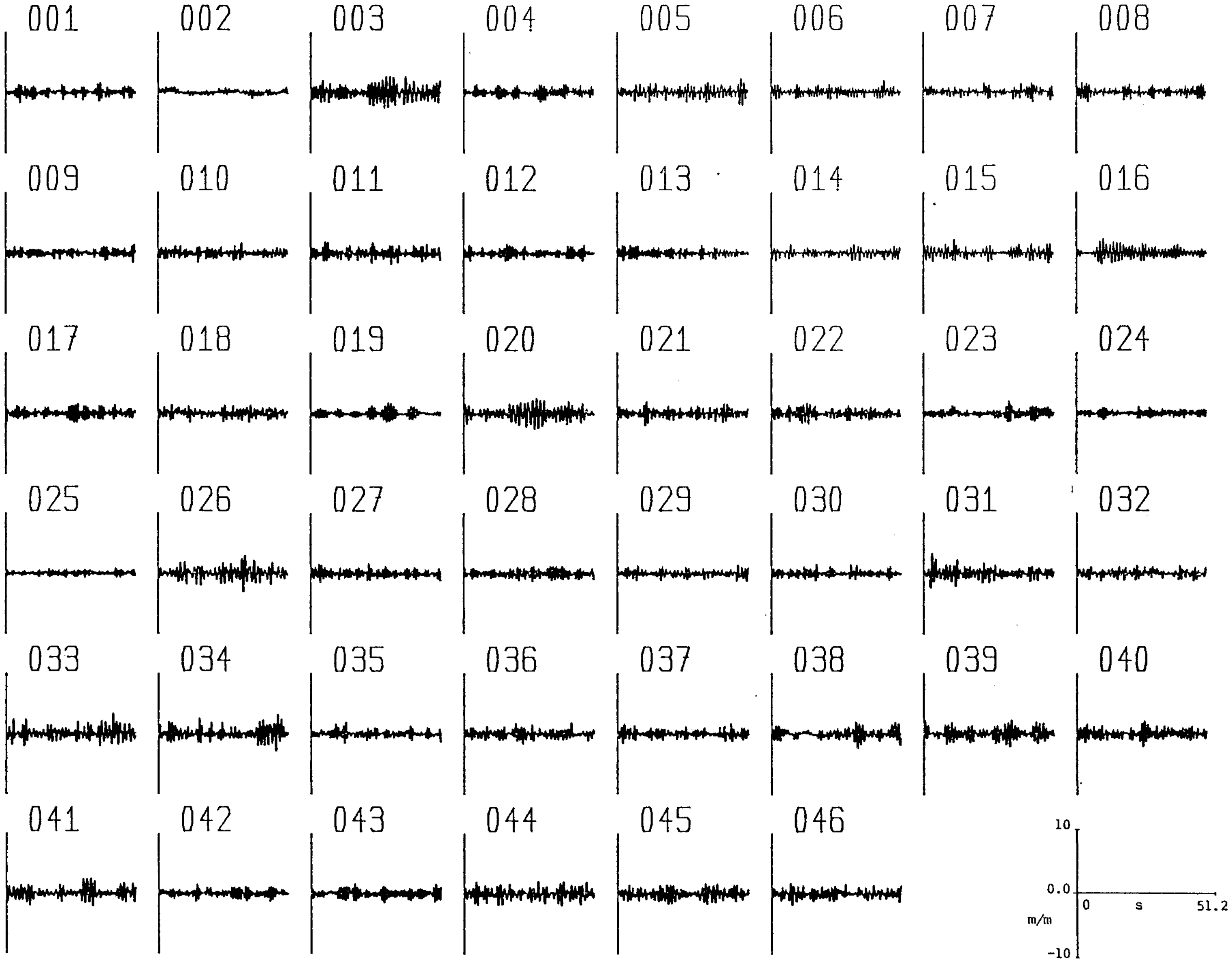

Figure 3.5 46 Spectra. Normalised heave motion

However, when one turns to the normalized position time series for surge, a more complex picture emerges. The traces look very similar to the ones for heave - but with the addition of large offsets and, in some cases, the appearance of a large low-frequency component. The latter is due simply to the mooring resonance (the mooring compliance coupled with the mass of the spine) which has a period of approximately 50 seconds, at model scale. The frequency of the observed resonance agrees with that calculated, when due allowance is made for the hydrodynamic added mass of the spine.

Again, one must compare these time series with the sea-state plots. The correlations are by no means hard and fast, but it is interesting to note that mooring resonance seems to be associated with seas offset from the principal wave direction, and that large spine drift seem to be associated with wide angular spreading.

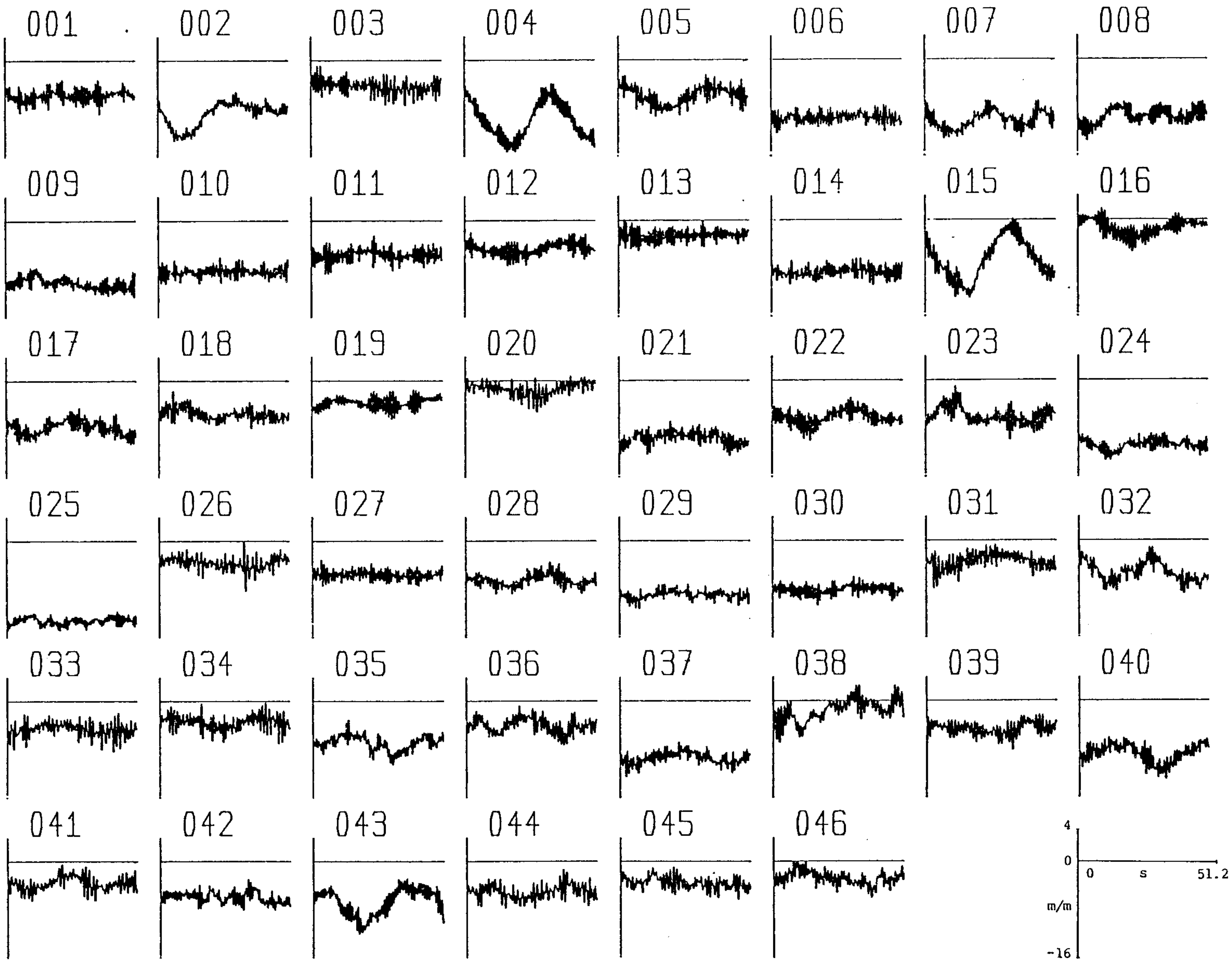

Figure 3.6 46 Spectra. Normalised surge motion

Figure 5.13 in Appendix C shows the angles included by the mooring lines. Also given is the algebra needed to derive them from the anchor gauge and position gauge records.

Angle A we term the base angle, B the second angle, C the third angle.

Figures 3.7 to 3.12 show how each of the 3 fore and 3 aft angles of the mooring respond in the 46 spectra. They have not been normalized by division by Hrms.

Note that the scale on each figure covers the same 0.4 radian range, but have varying offsets.

The graphs are similar to the surge position time series. They show the same features of drift and low-frequency response, including the 50 second mooring resonance. They also show a greater high-frequency content.

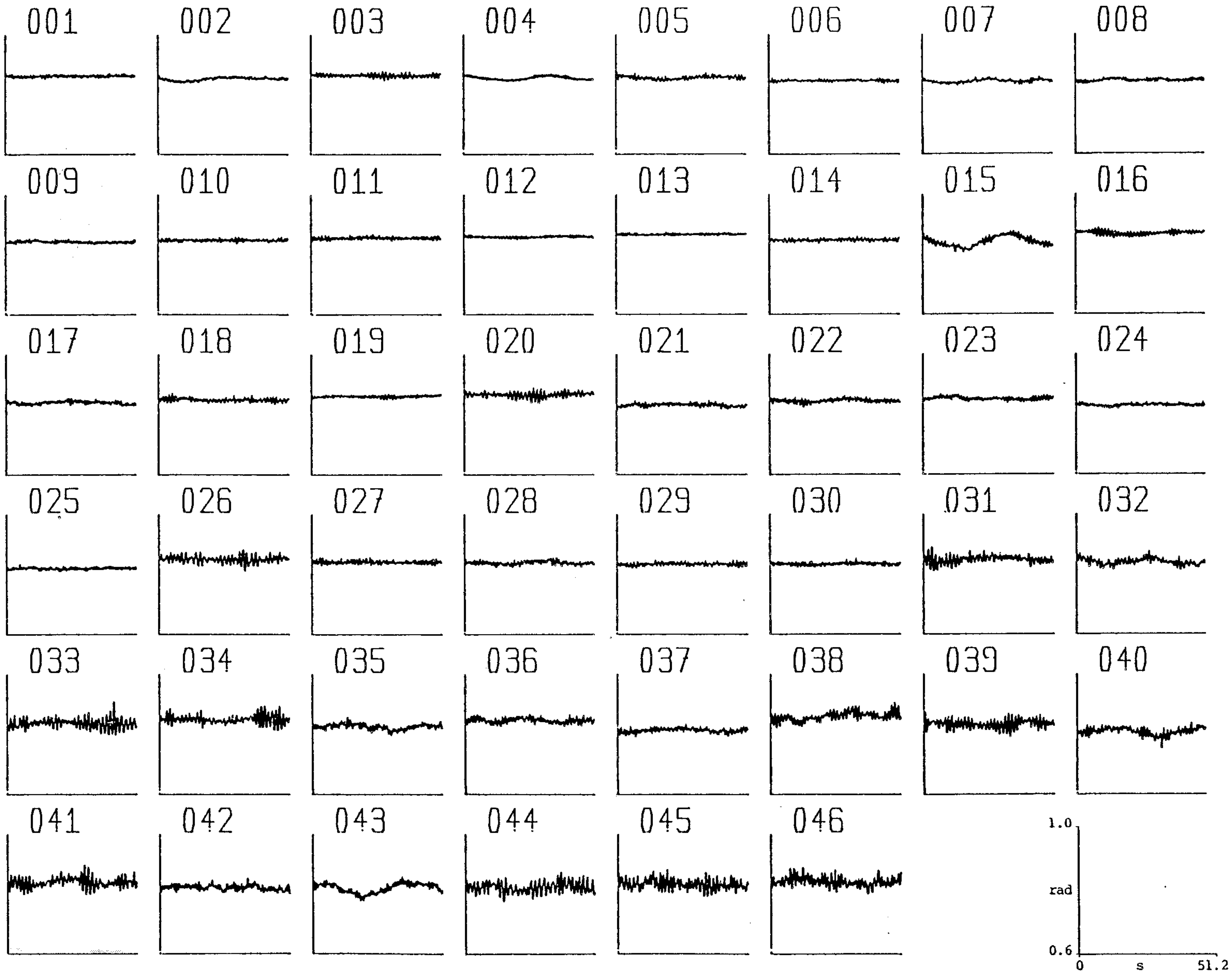

Figure 3.7 46 Spectra. Fore base angle

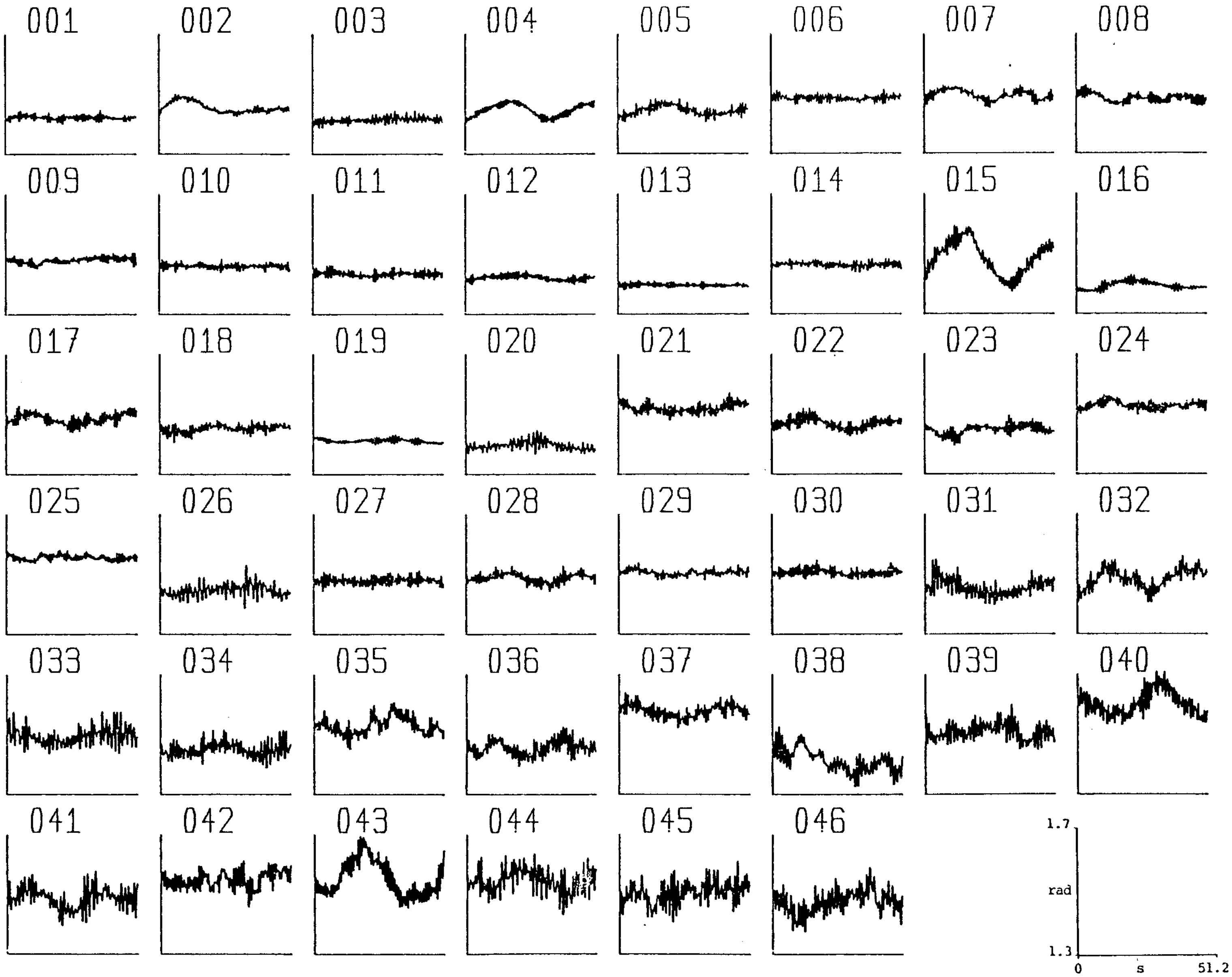

Figure 3.8 46 Spectra. Fore second angle

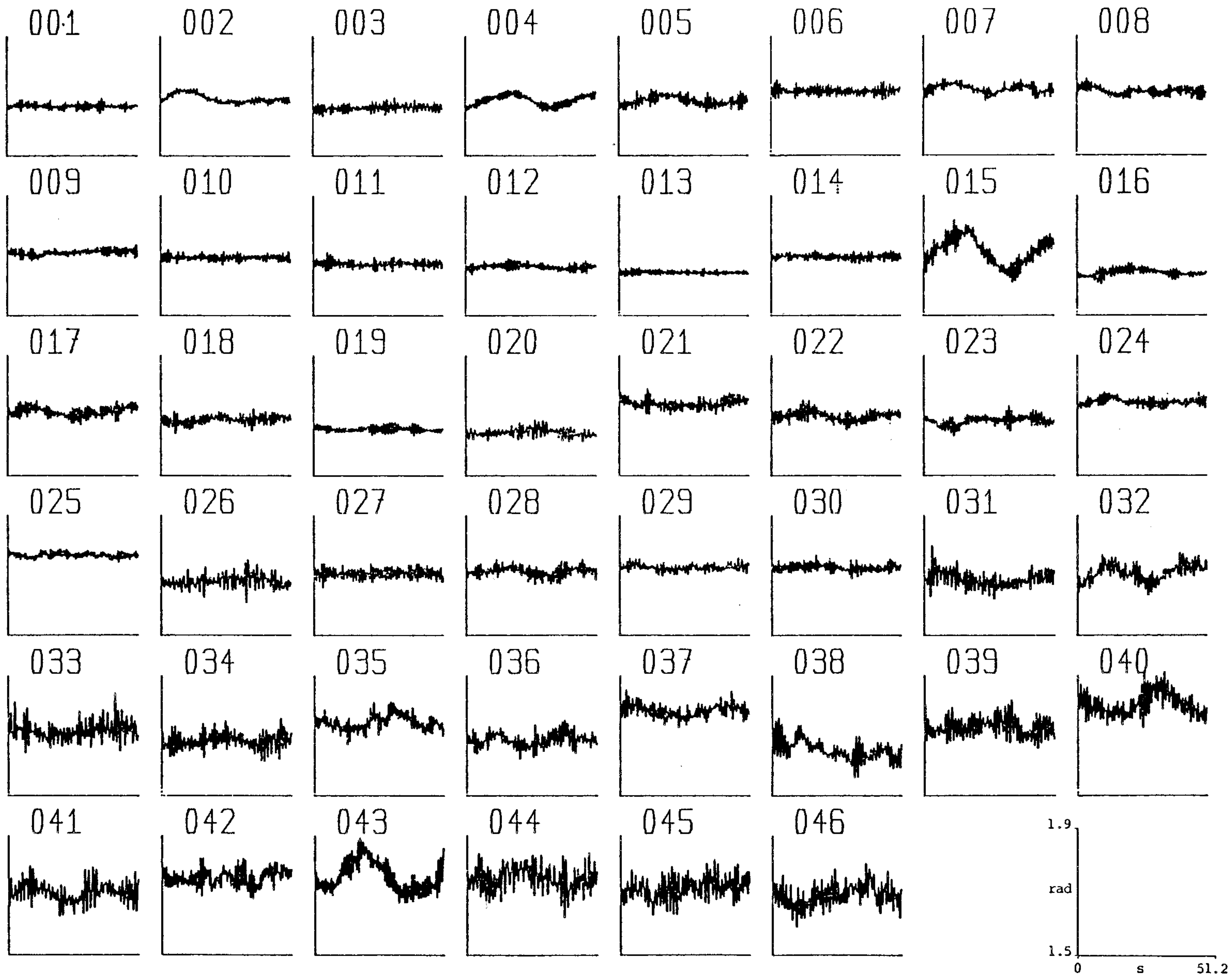

Figure 3.9 46 Spectra. Fore third angle

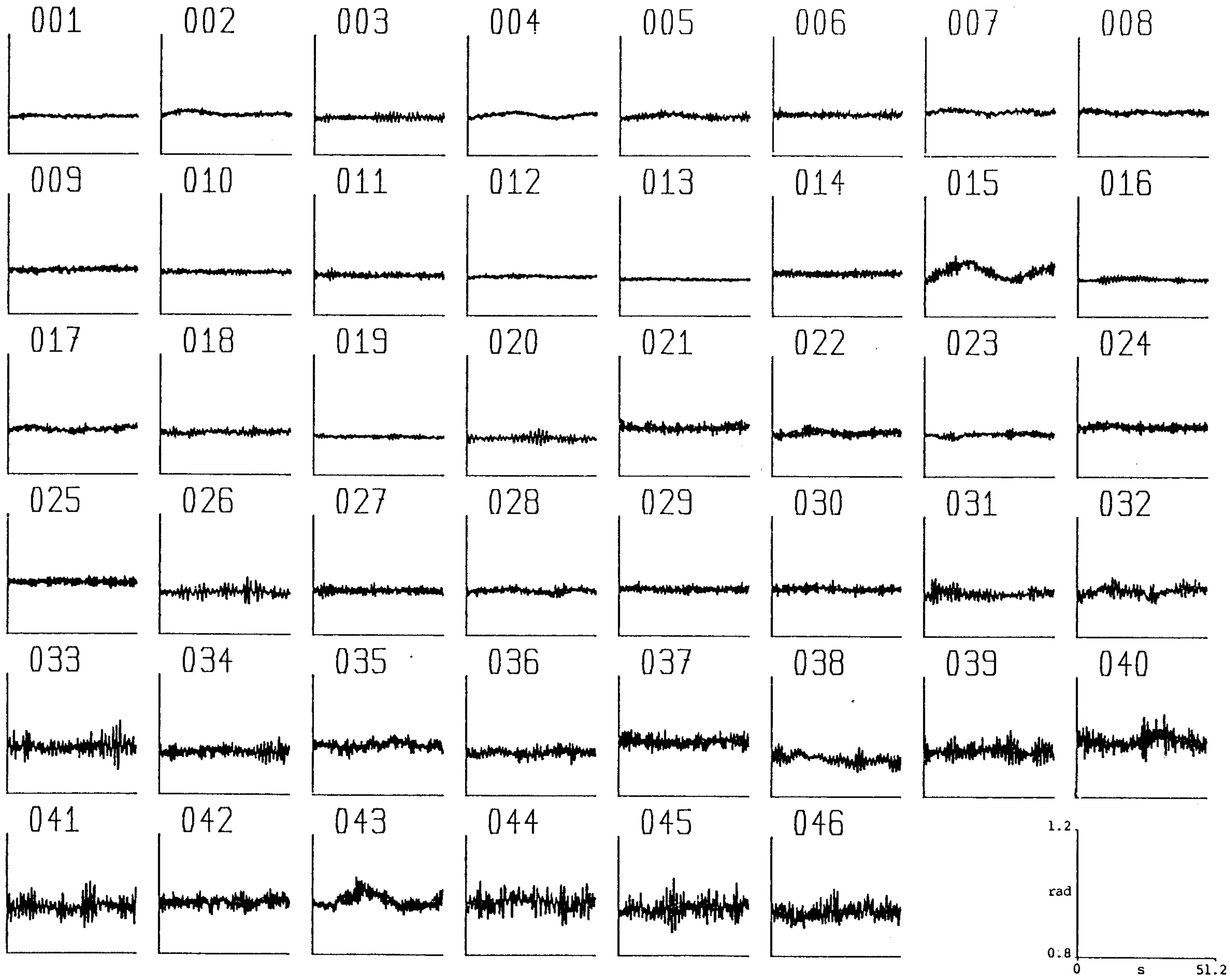

Figure 3.10 46 Spectra. Aft base angle

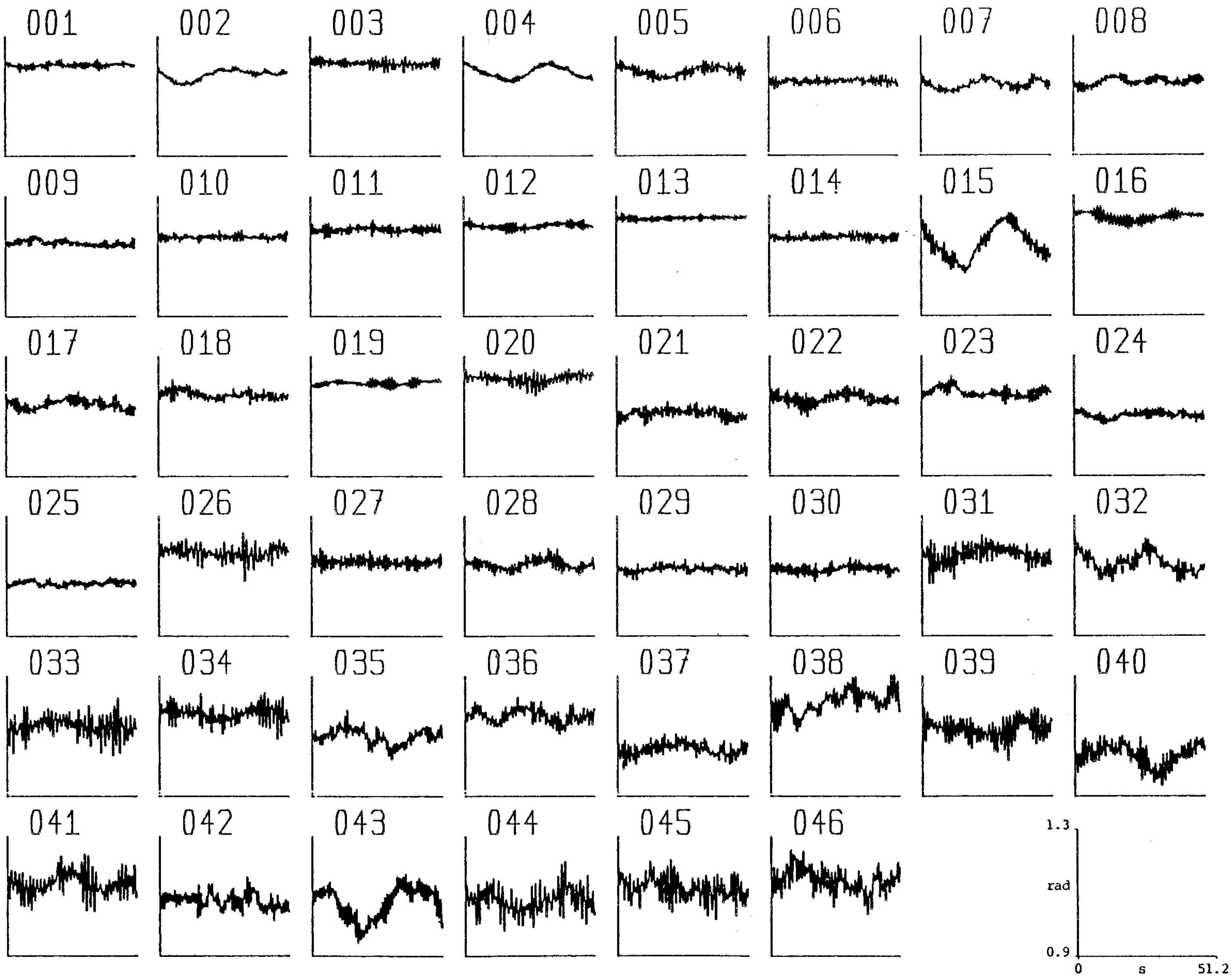

Figure 3.11 46 Spectra. Aft second angle

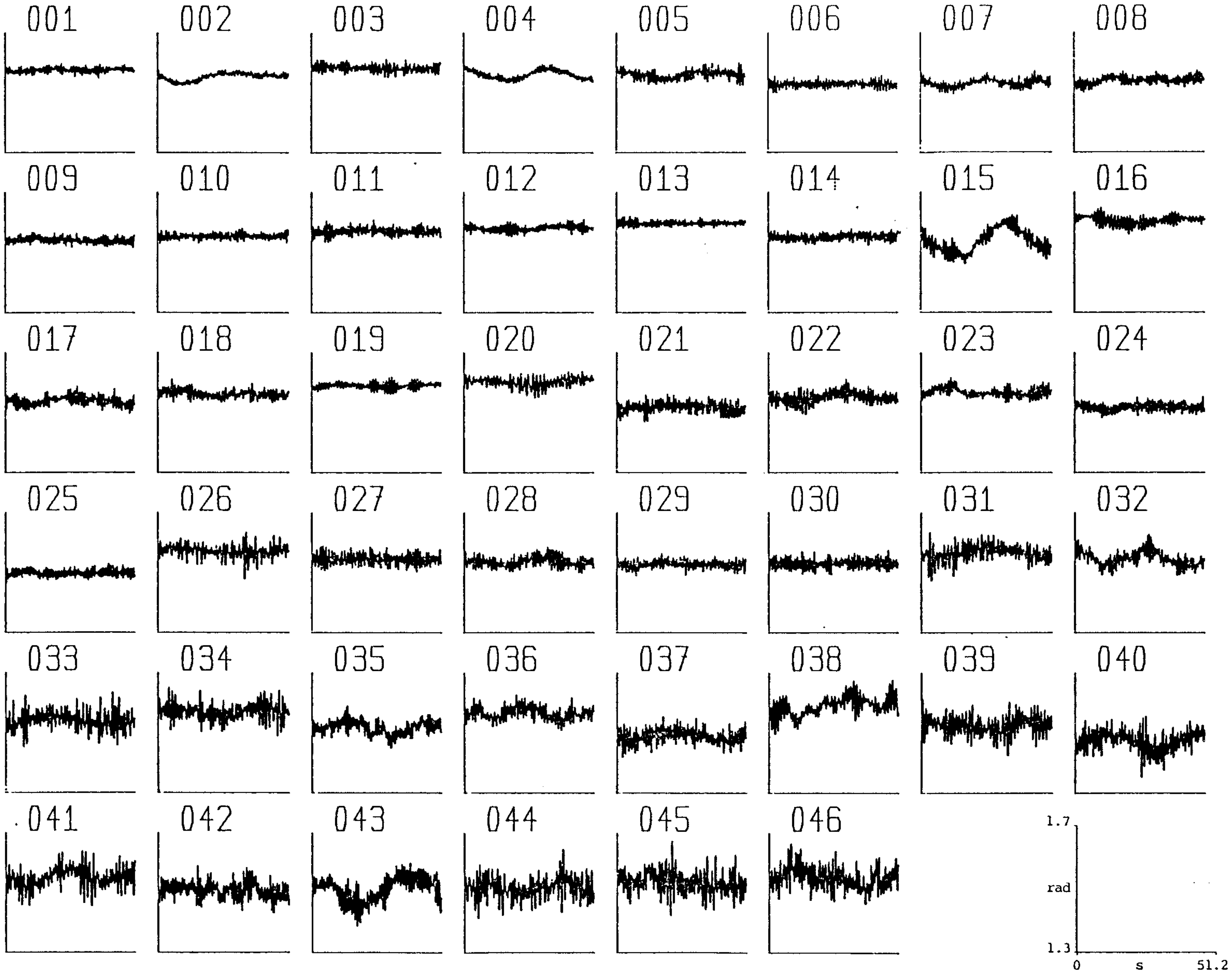

Figure 3.12 46 Spectra. Aft third angle

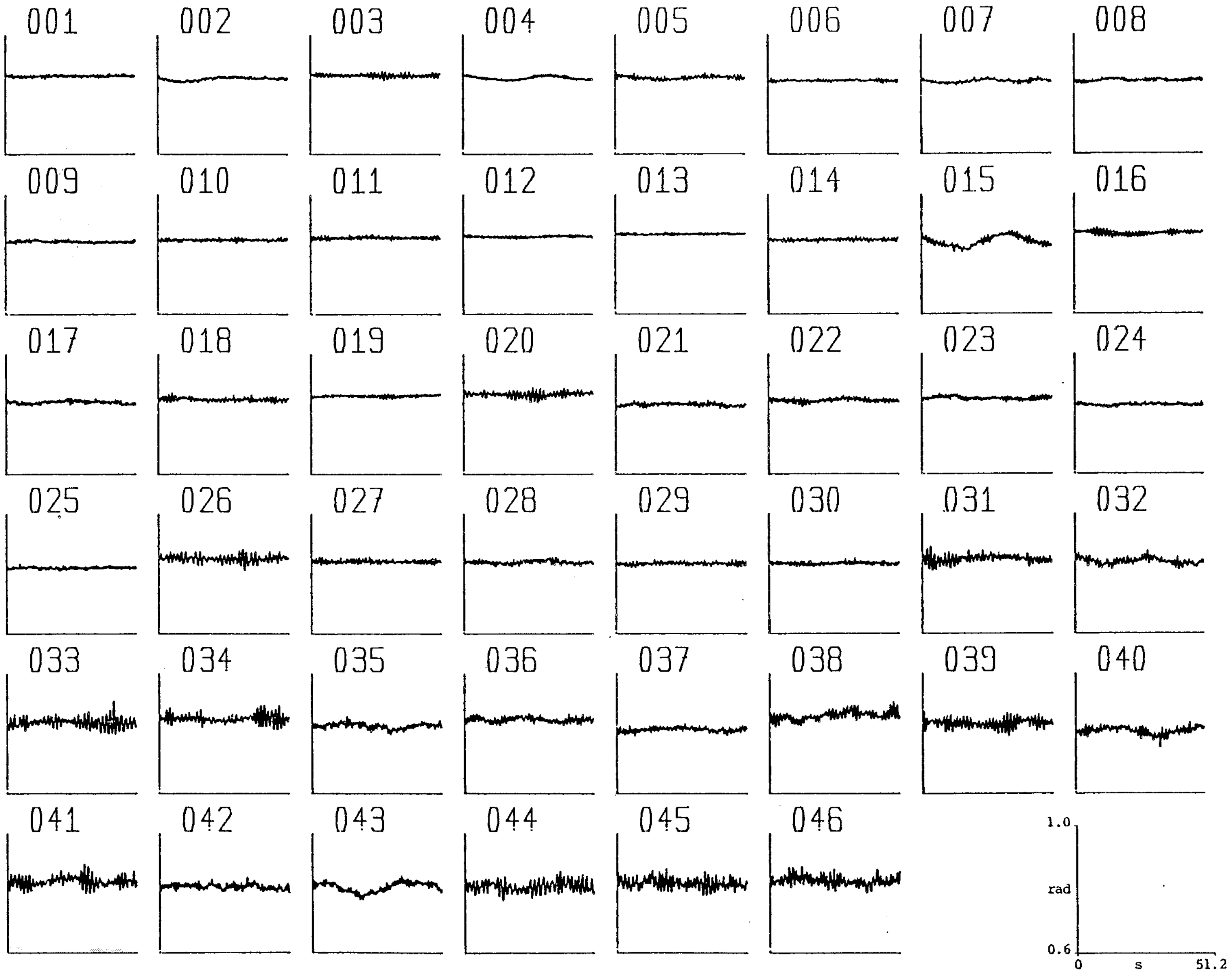

Figure 3.7 46 Spectra. Fore base angle

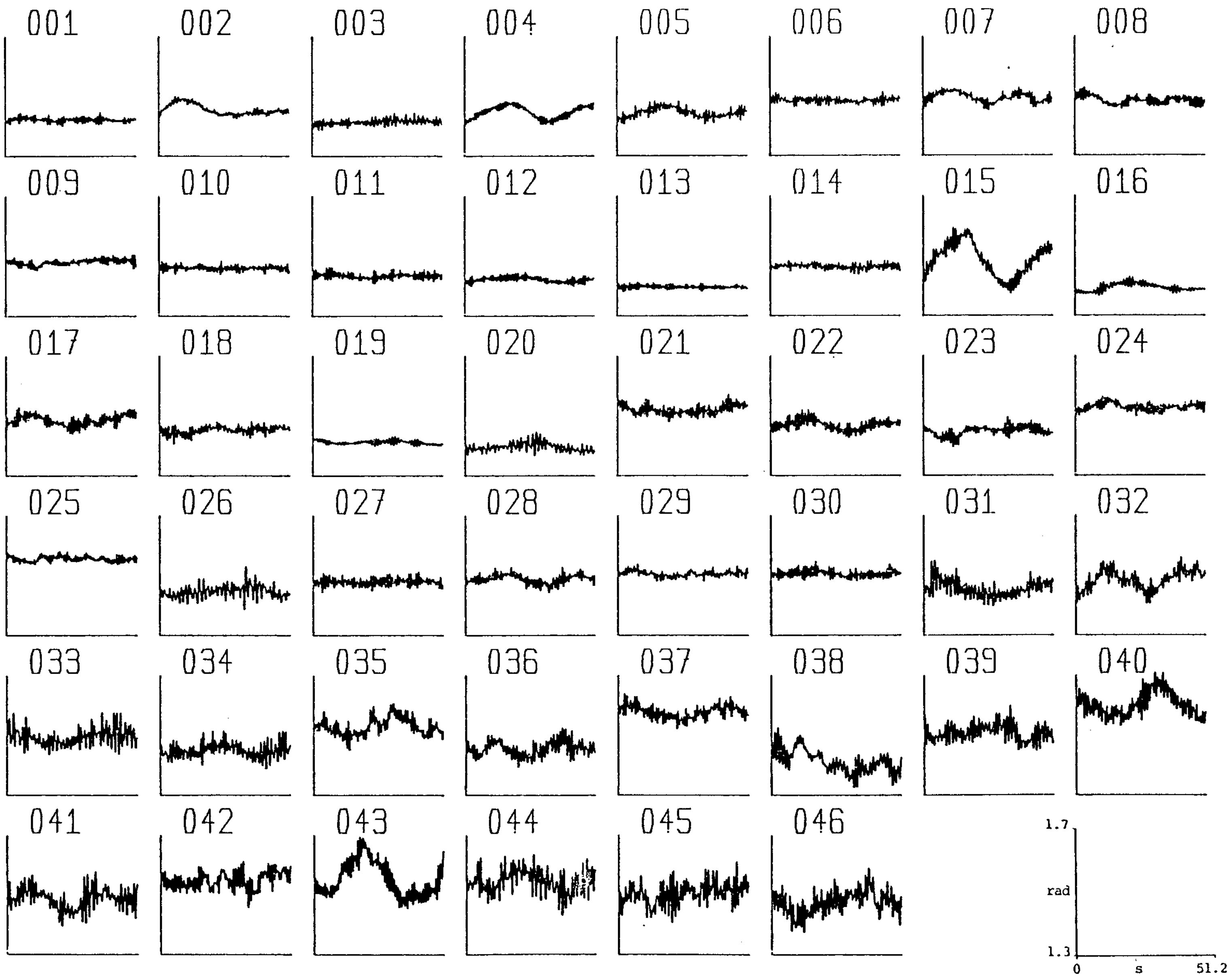

Figure 3.8 46 Spectra. Fore second angle

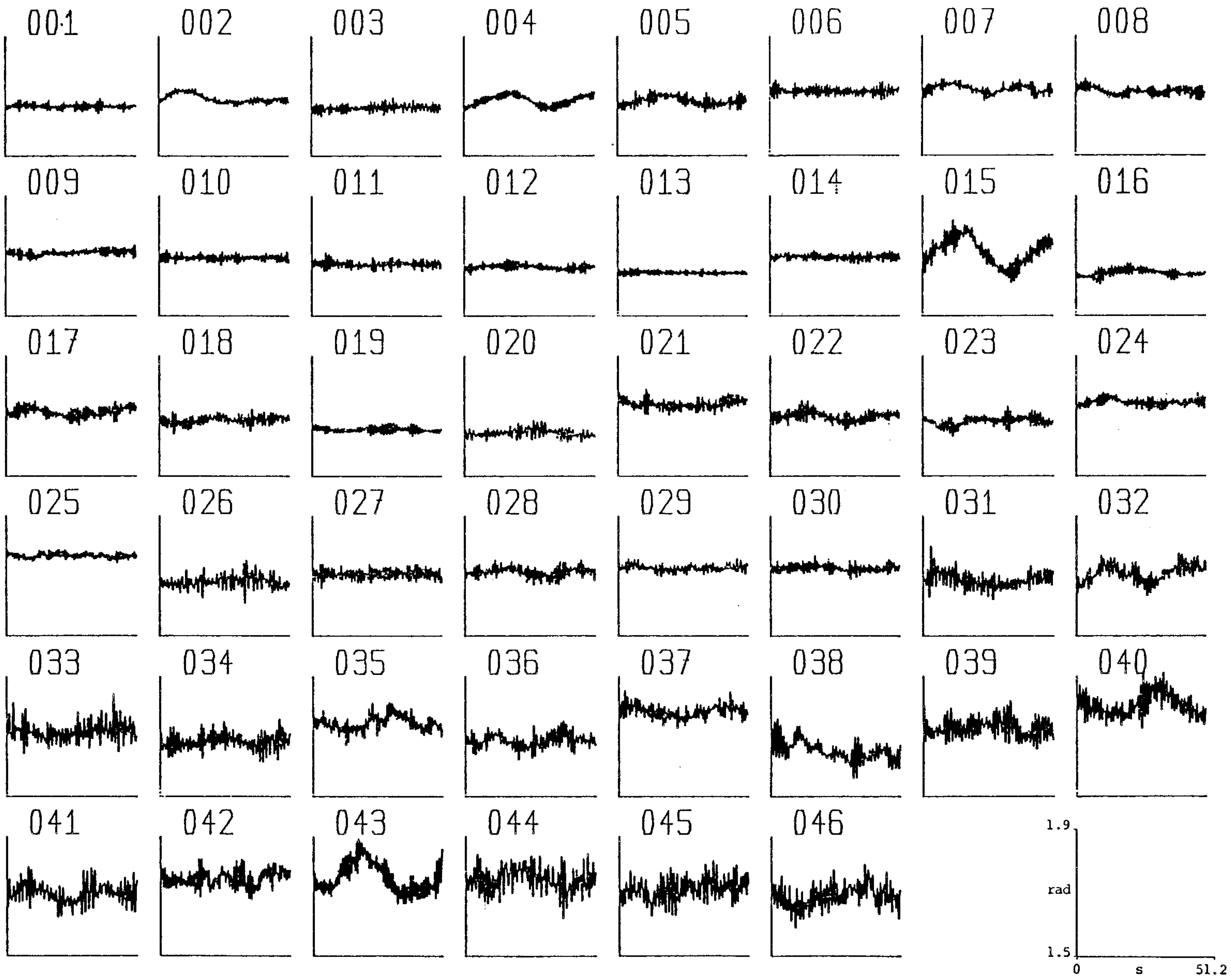

Figure 3.9 46 Spectra. Fore third angle

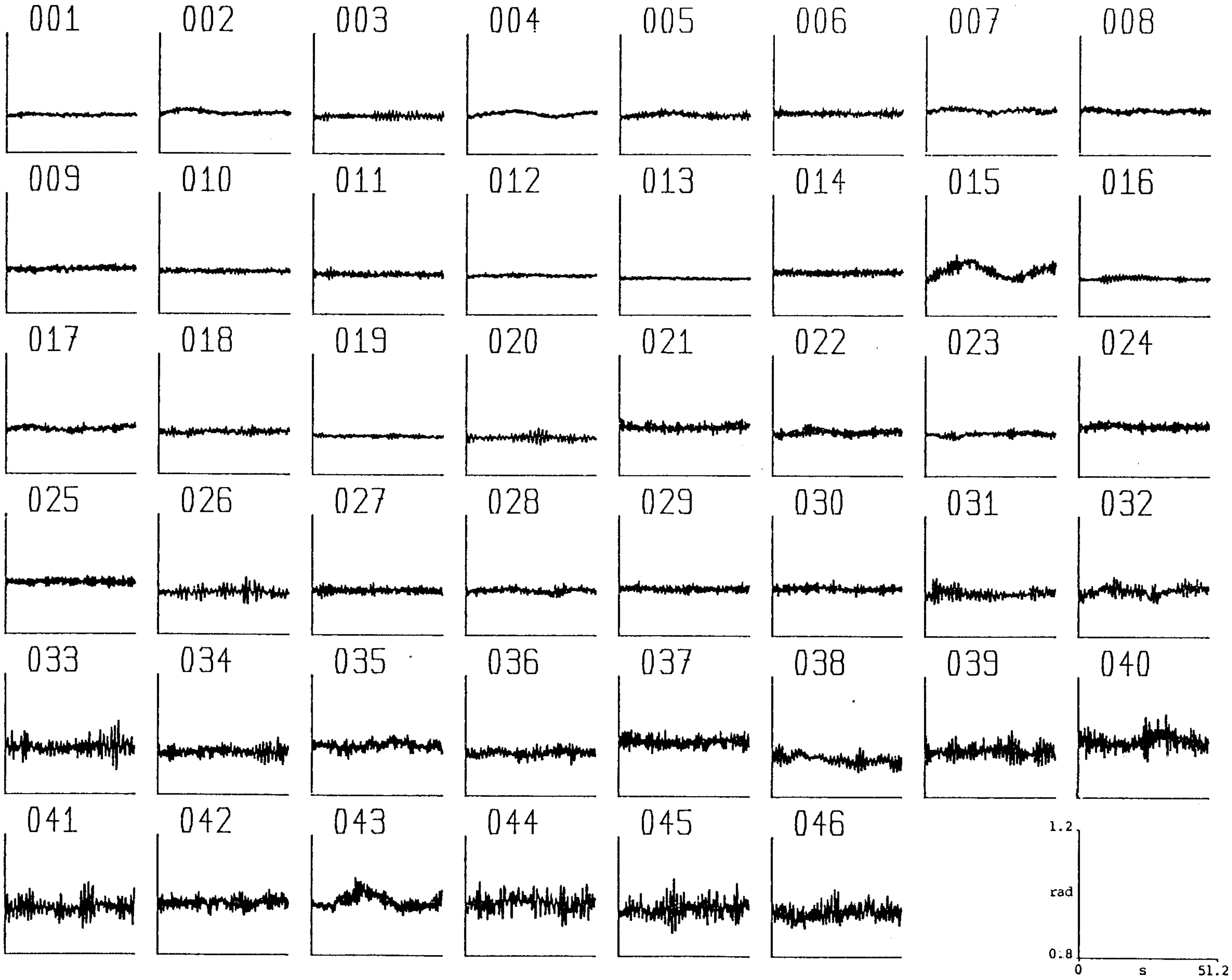

Figure 3.10 46 Spectra. Aft base angle

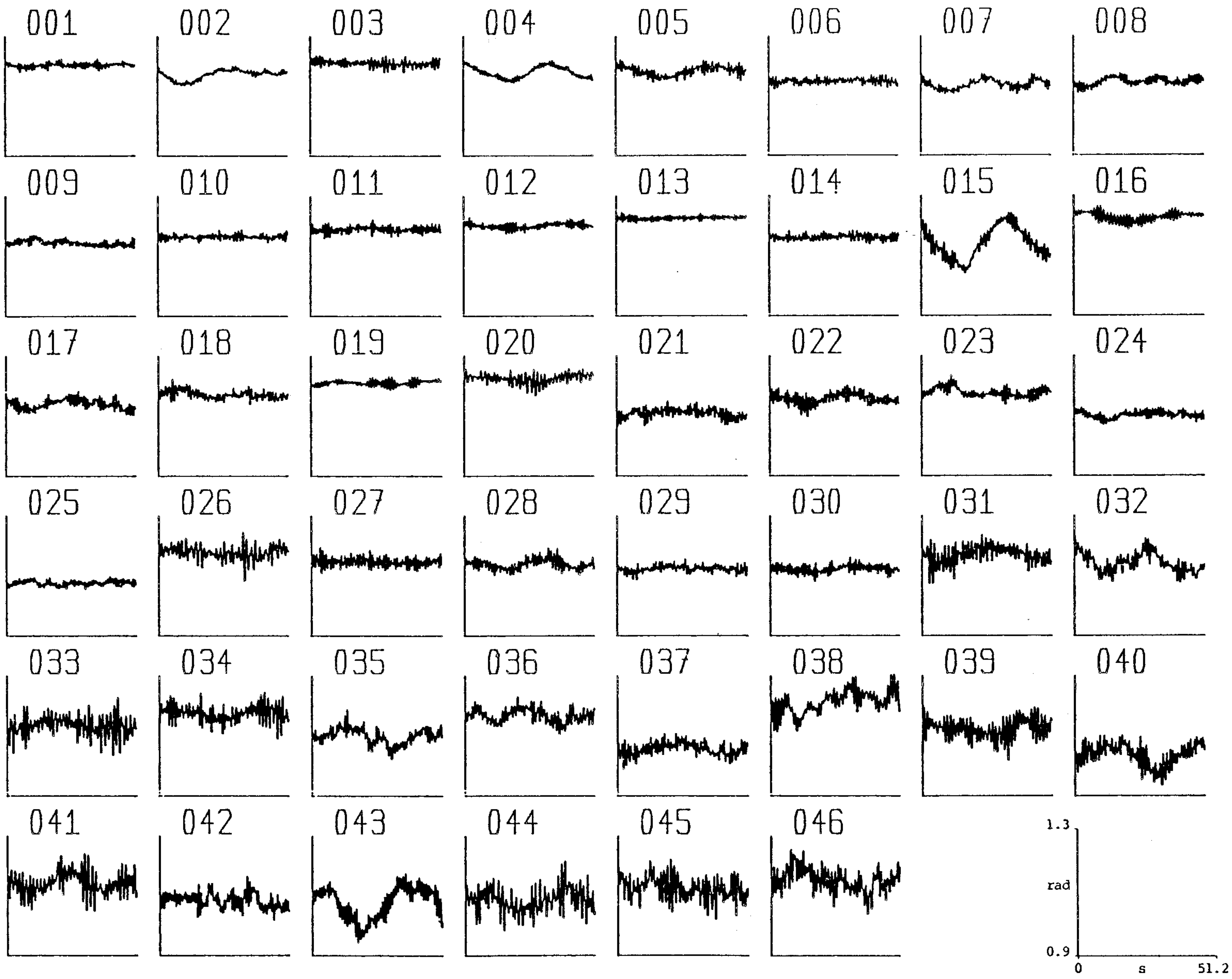

Figure 3.11 46 Spectra. Aft second angle

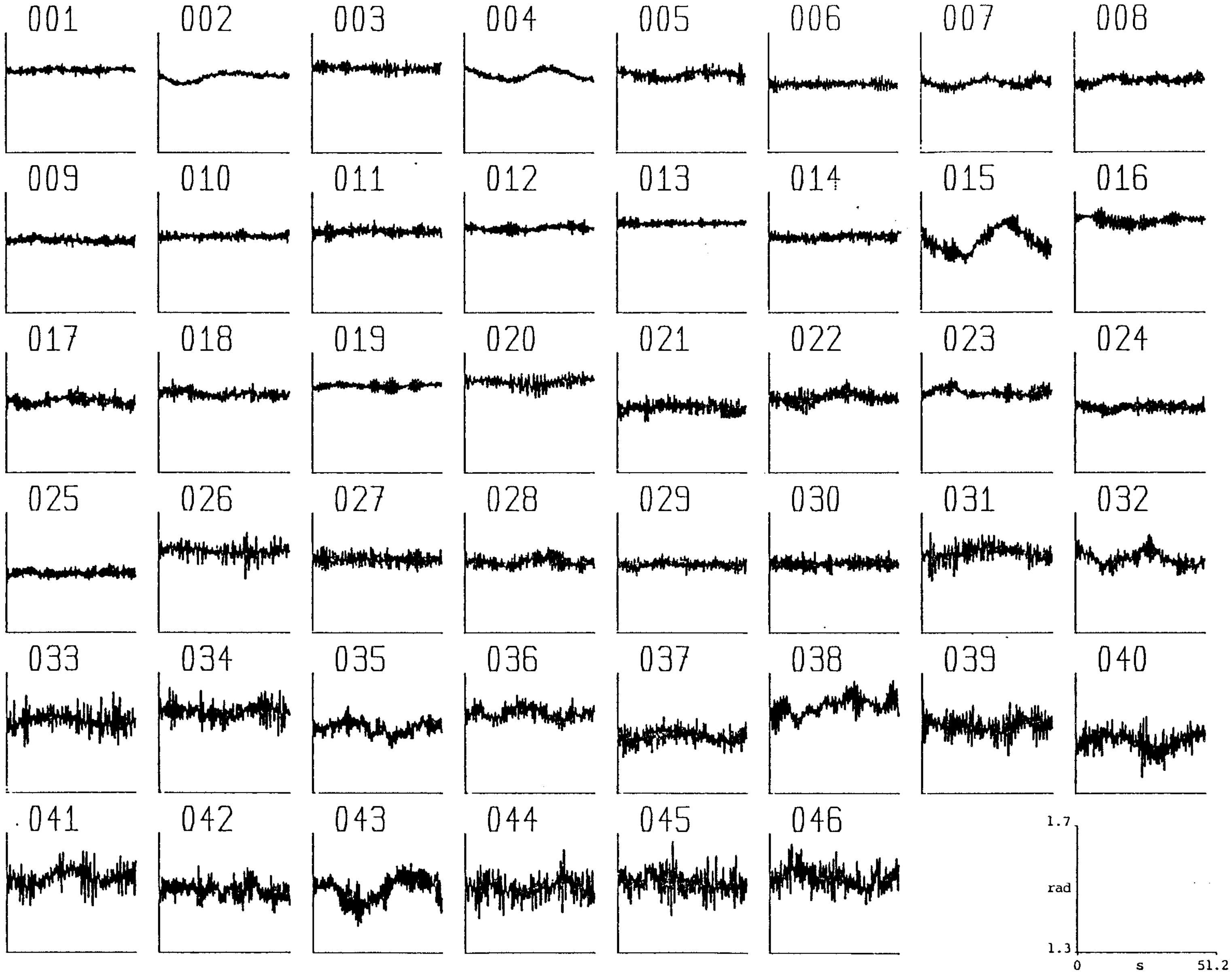

Figure 3.12 46 Spectra. Aft third angle

Figure 3.13 and 3.14 show the tensions in the first section of the mooring line for fore and aft (calculated as the modulus of the heave and surge forces obtained from the anchor gauges). Figures 3.7 and 3.10 showed the aft angles to be greater than fore, now we see that the fore tension is greater than the aft. This confirms that the fore anchor is operating at greater stretch than the aft. Otherwise, the traces appear similar, showing the same basic features of drift and low-frequency content.

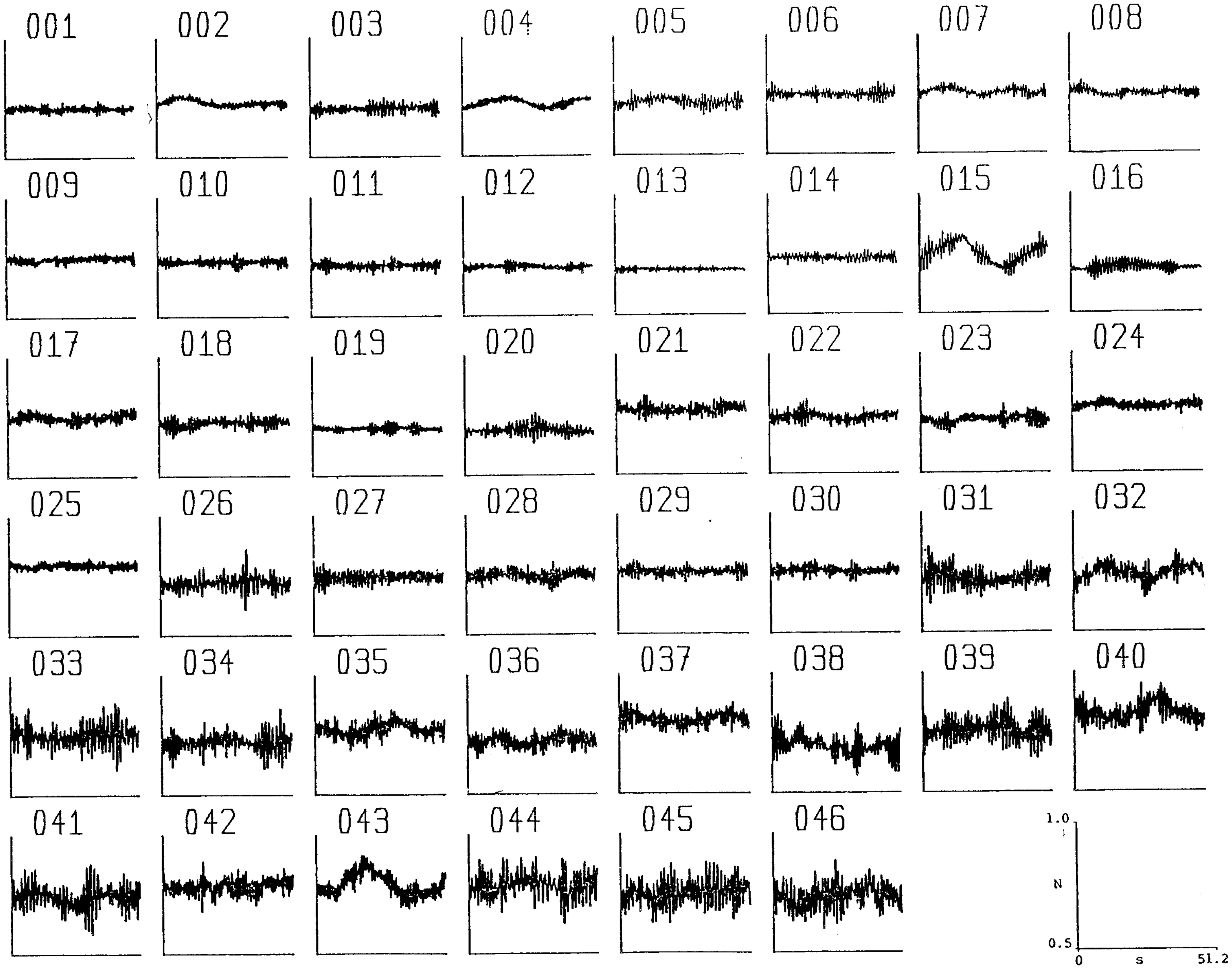

Figure 3.13 46 Spectra. Fore base tension

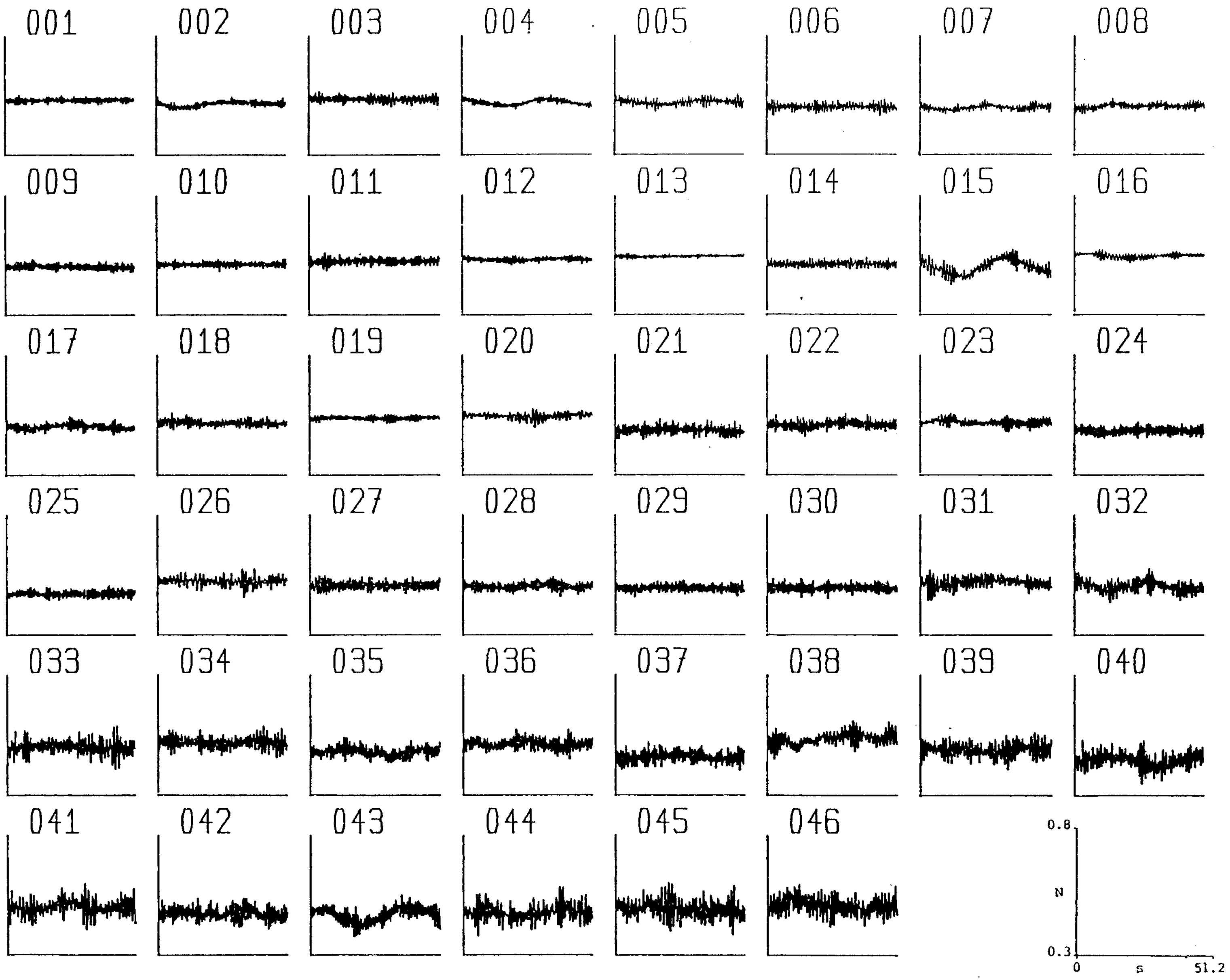

Figure 3.14 46 Spectra. Aft base tension

Figure 3.15 shows the root-mean-square variation in aft base angle versus Hrms for each of the 46 spectra. Figure 3.16 shows the equivalent for tension. Both show a steady rise, demonstrating the general relationship of mooring loading with sea size. Part of the scatter will be due to noise, which is of the order of 2 milliradians rms and 2 millinewtons rms, and part to the previously mentioned effects on mooring response of the principle direction; and directional spreading of the sea-state. The pattern of the points is similar in the two diagrams, demonstrating the good correlation of variation in angle with variation in tension.

A noticeable difference between the two graphs is that the least-squares fitted line goes through the origin in the case of the tension, but is displaced in the graph for angle. This suggests that while tension is proportional to sea size, there is a force ´break-out´ region for angle - ie, a region where angle is non-linear with wave force.

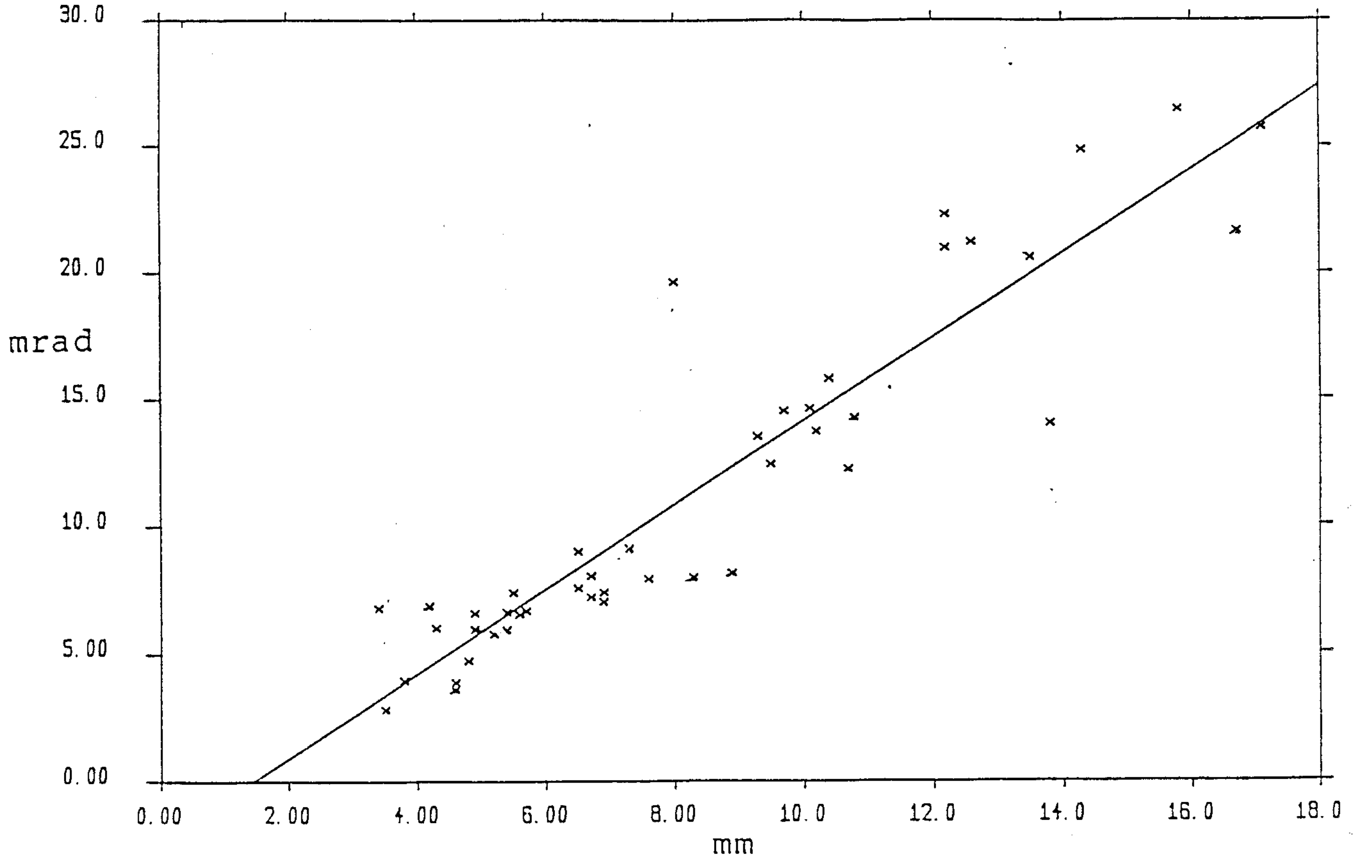

Figure 3.15 46 Spectra. Rms aft base angle against Hrms

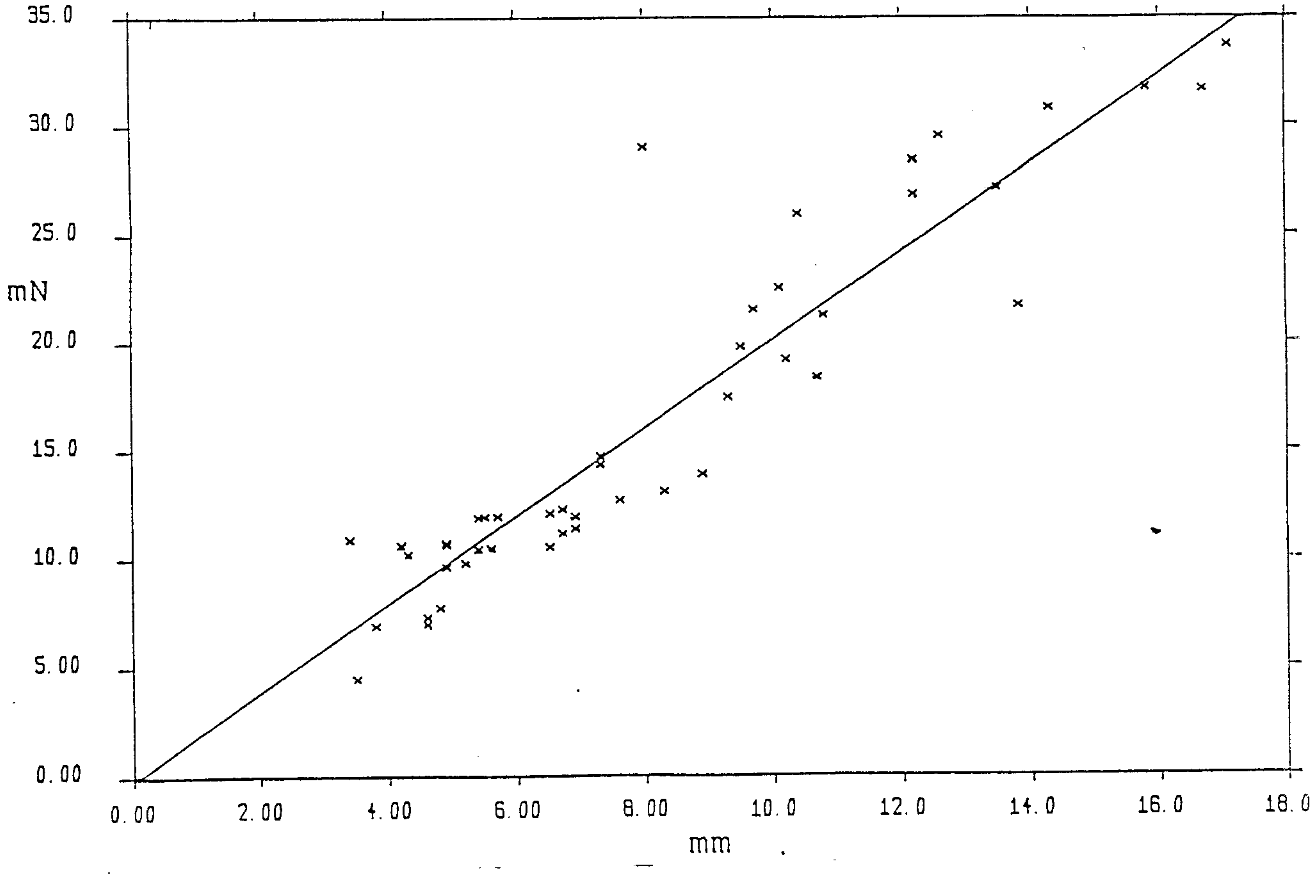

Figure 3.16 46 Spectra. Rms aft base tension against Hrms

The use of the root-mean-square is a concise and valid expression of fluctuating data. However, it becomes more meaningful to the engineer if the distribution is known to be Gaussian, in which case the rms approximates closely to the standard deviation, and may be used to predict extreme data. In the following three graphs we have drawn the normal curves corresponding to the mean and standard deviation of the data for the water surface elevation of the 46 spectra, and to the fore and aft base tensions of the moorings. The crosses represent the population of histogram cells of the measured data. In each case the horizontal scale is in units measured at tank scale against an arbitrary vertical scale of occurrence.

Figure 3.17 shows the wave elevation. The histogram data, compared with the normal curve, displays positive kurtosis, ie, a relative overpopulation of the central cells and tails of the distribution, at the expense of the cells of medium deviation. Part of this could be due to noise - but since the measured noise of the wavegauges corrresponds to 0.1 mm and the cell width is 2 mm, this is unlikely. However, when one sums a number of normal distributions of differing standard deviation, positive kurtosis must result. The 46 spectra are close enough to normal for this to be the likely explanation.

Figures 3.18 and 3.19 are the histograms of the fore and aft mooring tensions. The graphs are drawn to the same scale, and it is clear that the fore mooring has a greater standard deviation. The tension variations are greater in fore since it is running at greater stretch than the aft mooring.

These tension histograms also display the positive kurtosis of the wave elevation graph - as we would expect since the moorings are wave-driven. However, the overpopulation of the central cells is not so acute. The anchor gauge noise is equivalent to 0.5 nN in the fore case, 2.0 mN in the aft.

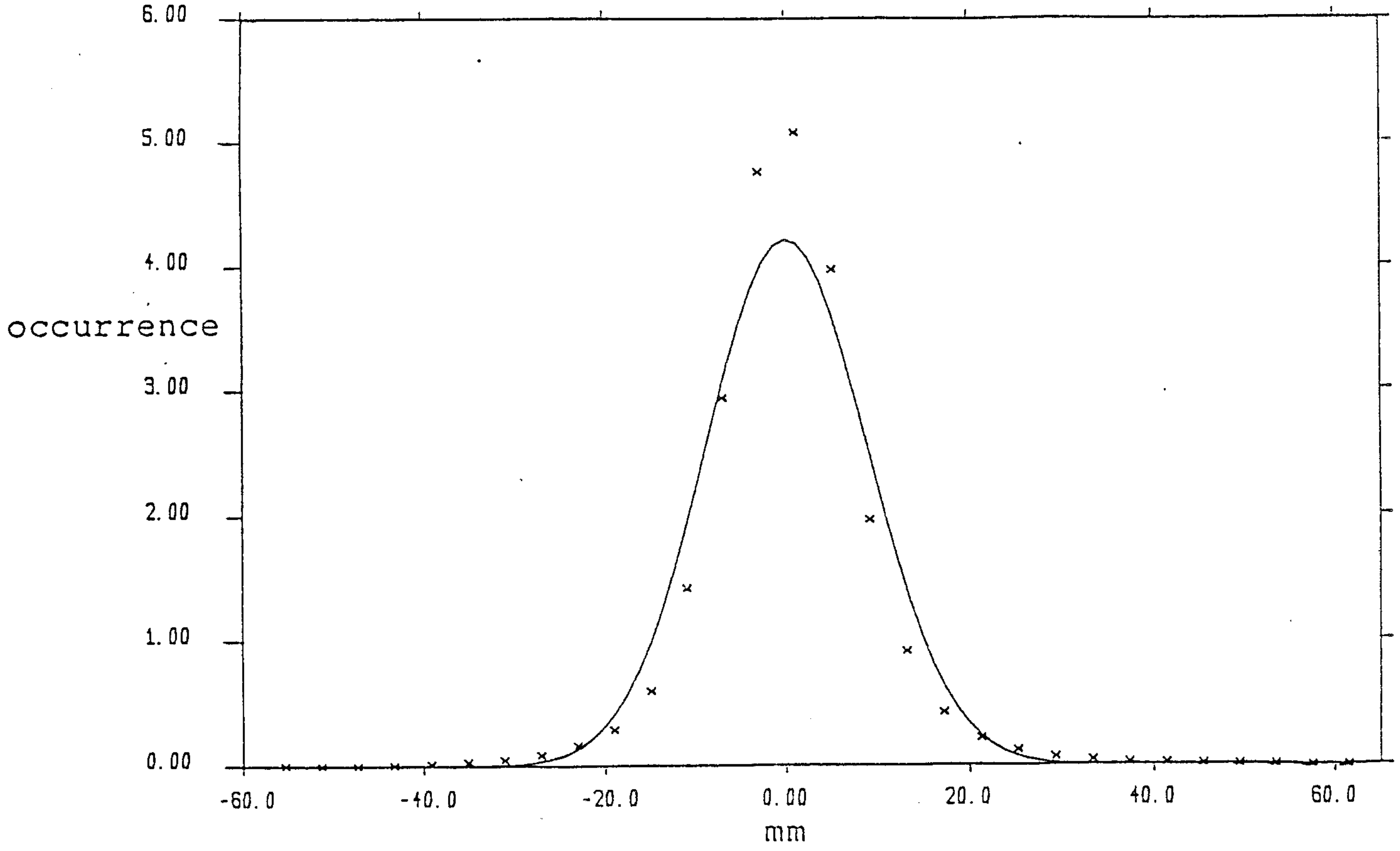

Figure 3.17 46 Spectra. Histogram of wave elevation

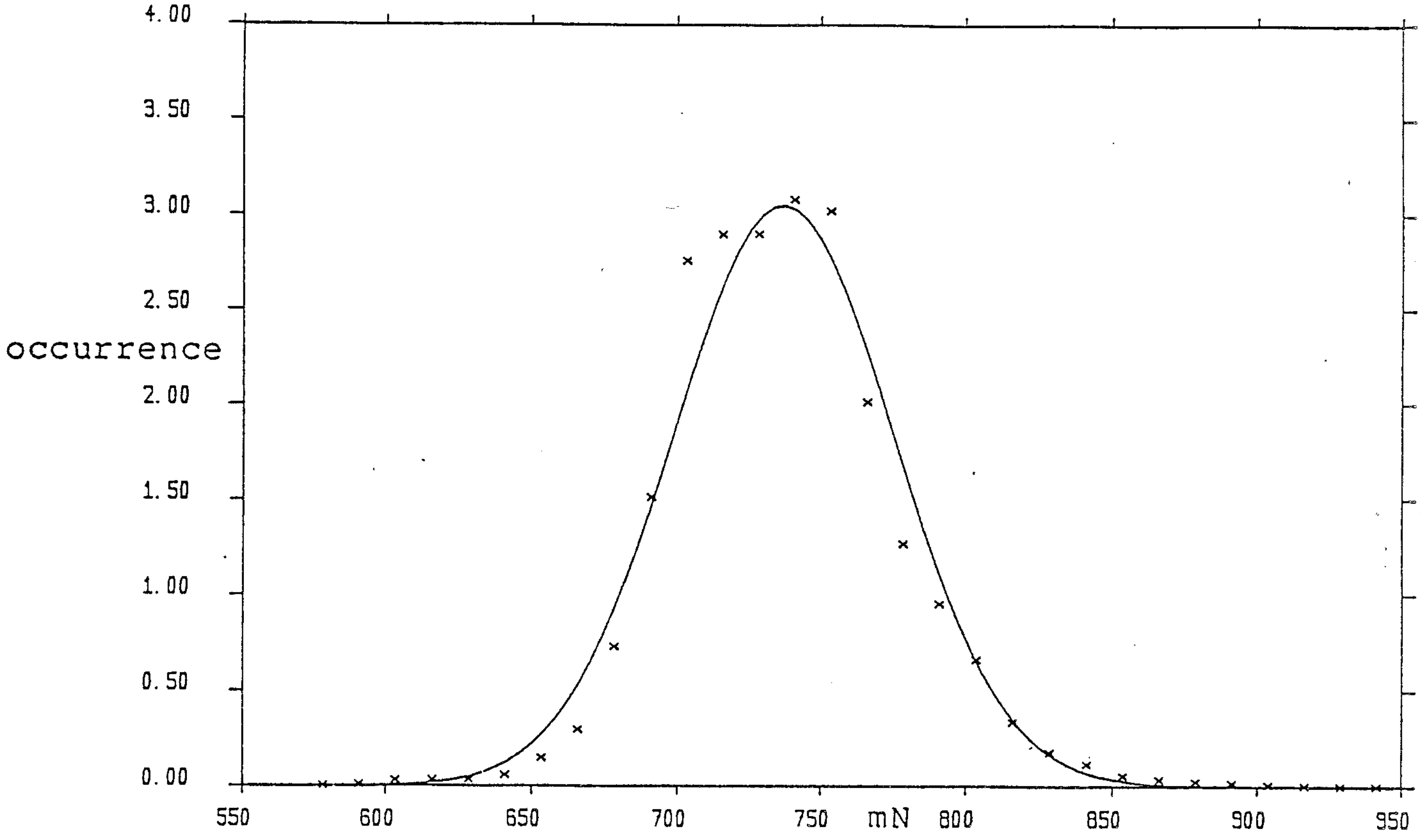

Figure 3.18 46 Spectra. Histogram of fore base tension

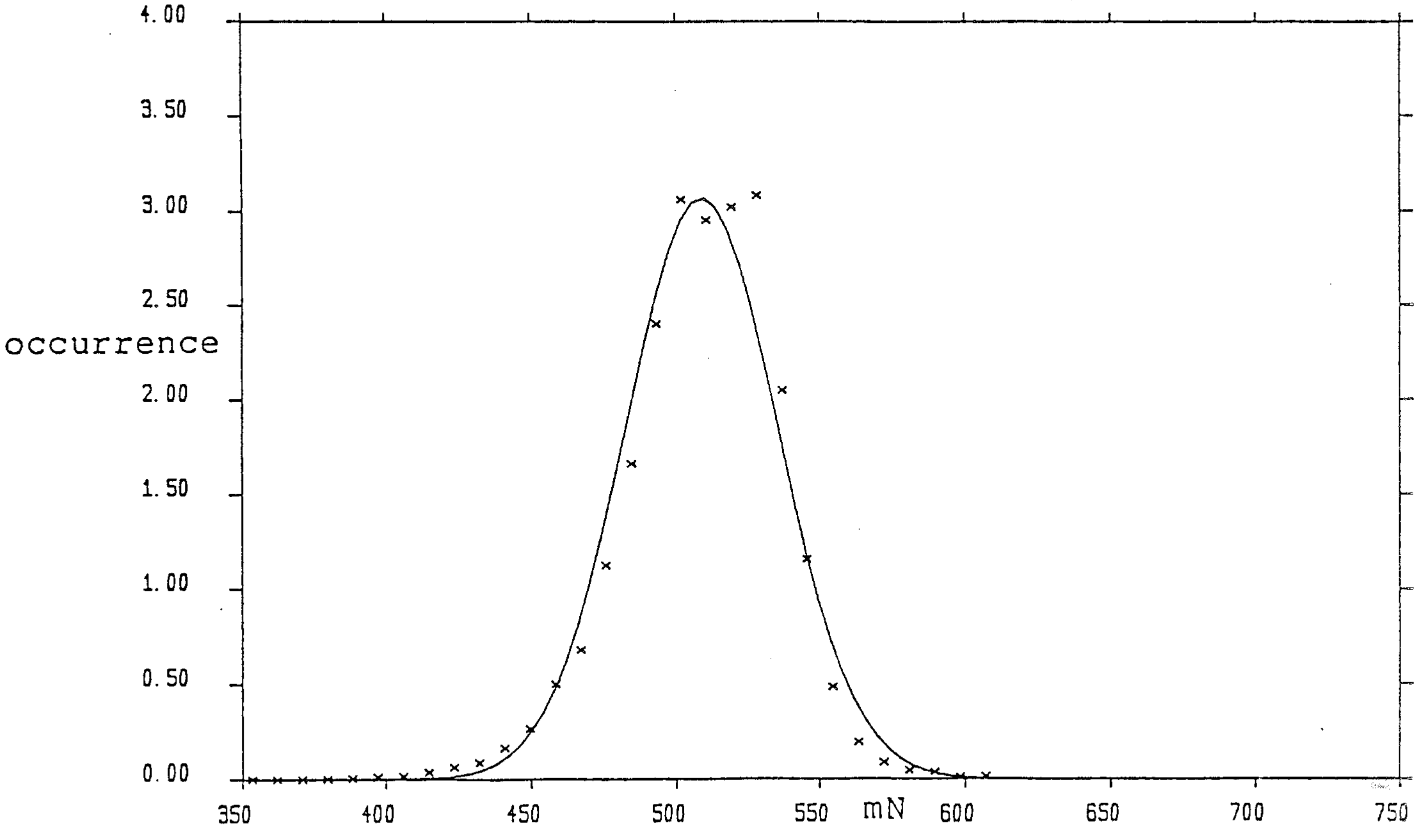

Figure 3.19 46 Spectra. Histogram of aft base tension

Also apparent is that the distributions are skewed: the fore data to smaller tensions; the aft data to larger tensions. A chi-squared test showed the effect to be significant - as does the fact that they are complementarily positively and negatively skewed. This result suggests a slightly non-linear relationship between mooring tension and wave height. This is not a surprising result: the spine motion is non-linear with wave height; and the mooring tension is non-linear with extension.

To conclude, in general mooring loads rise with sea size, and show a lower scatter in the 46 spectra than, say, spine bending moments. The normal distribution is not adequate for the prediction of extreme loads, and logarithmic distributions (eg, Weibull) are probably safer.

Weighted average results for the spine in the 46 spectra are presented in Table 3.2.

For the wave amplitude, the calm-water value is defined to be zero, and the mean value equals this. The standard deviation (which, for 1024 samples is only 0.05% different from the root-mean-square value) is 7 mm.

For spine position the calm-water value in heave and surge is again defined to be zero,

The mean value of heave position equals zero because of the extra restoring force due to spine buoyancy. The standard deviation of motion is 4.5 mm, which is less than the water motion due partly to the resistance of the spine to motion, and partly to crest averaging.

The mean value of spine surge position is some 33 mm aft of that in calm water. This is a result of the moorings yielding to Longuet-Higgins momentum forces. These drift forces also contribute to standard deviation of motion of 8.7 mm - nearly twice that in heave.

The effect of the aft drift is to increase the fore tension and decrease the aft tension; concommitantly to increase the aft angle, and decrease the fore. The standard deviation of tension variation is about 2.8% of the mean value in both the fore and aft cases.

TABLE 3.2 ANNUAL WEIGHTED AVERAGES FOR THE MOORING AND SPINE

WAVE AMPLITUDE (millimetres)

axis	calm-water value	mean value	standard deviation
heave	0.0	0.0	7.0

SPINE POSITION (millimetres)

axis	calm-water value	mean value	standard deviation
heave	0.0	0.0	4.5
surge	0.0	-33.4	8.7

MOORING TENSION (millinewtons)

tension	calm-water value	mean value	standard deviation
fore	675	722	21
aft	552	520	14

MOORING ANGLES (milliradians)

angle	calm-water value	mean value	standard deviation
fore base	684	805	7
fore second	1535	1487	18
fore third	1486	1647	17
aft base	682	879	10
aft second	1478	1276	18
aft third	1420	1518	16

An interesting result is apparent from the table of mooring angles. Relative to their calm-water values, the mean angles change substantially: the base and third angles increase; the second angle decreases. It is clear that the mean position of the floats is higher than their calm-water value: 120 mm in the aft case, 75 mm in the fore. The other angles adjust to accommodate this rise.

Note also that the standard deviation of the second angle is larger than the third, which implies that the angle of the first section of line with the tank floor varies more than that of the third section of line with the tank floor. The static analysis indicates that the variation should be the same. This is a fascinating result. It implies that the float and sinker are moving in such a way as to augment the first angle and diminish the third. The heave oscillation of the mooring, discussed in the mooring dynamics of appendix D does precisely that.

The mooring resonance therefore moves the float more than the spine motion requires it to. Furthermore, most of the spectra are centered on 1 Hz, and the float is about a 1 Hz wavelength - 1.56 m - from the spine, so loading on the float due to the spine motion, and to the waves, will be in phase.

It is clear that the mooring design could be changed to mitigate the effects of the resonance, and that it would be better to locate the float at a half, or one and a half wavelengths from the spine.

However, even at present, the annual weighted average of the second angle motion is only 18 milliradians - about 1 degree.

To gain a more exact idea of the wave forces on the moorings, we removed the spine and tied its mooring lines to a fixed point exactly as we did for the freak wave experiment. This time we ran the 46 spectra, and again recorded the anchor gauge force signals.

The tension records for the fore and aft moorings are presented in figures 3.20 and 3.21, and the angle records in figures 3.22 and 3.23, to the same scale as the equivalent experiments with the mooring plus spine. They do not, of course, show any of the low frequency and drift effects that were present with the spine.

A condensation of these data as before, to annual weighted form is presented in Table 3.3. The mean value of the tensions is slightly reduced from the calm-water value, and the angles increase slightly. But the effects are about six times smaller than for the mooring with spine.

On the other hand, the standard deviation show that the angle and tension varies about half as much as with the spine.

The conclusion is that wave loading on the moorings accounts for a large part of the mooring response, but that the rise of the floats is mainly dependant on the presence of the spine.

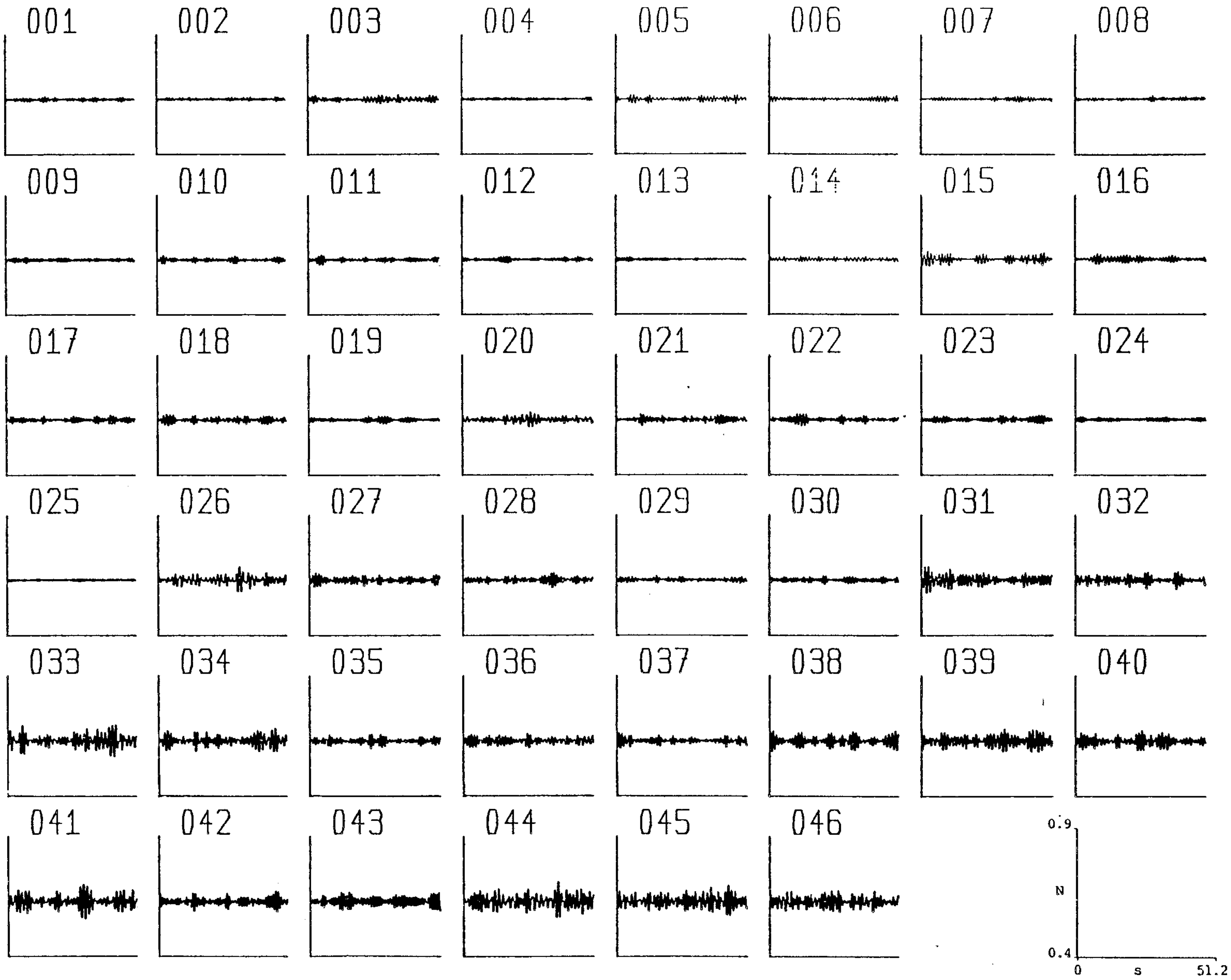

Figure 3.20 46 Spectra. Fore base tension: fixed mooring

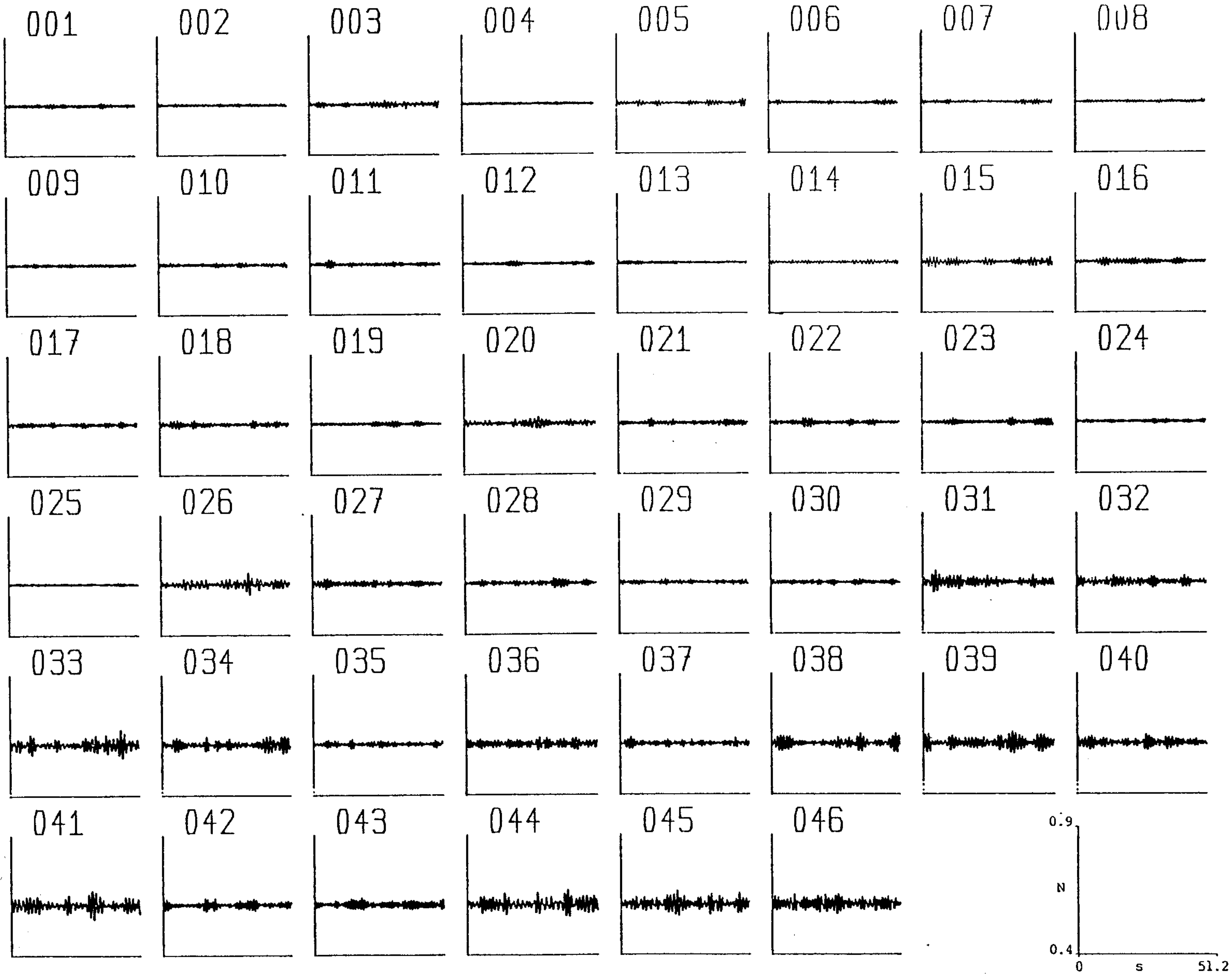

Figure 3.21 46 Spectra. Aft base tension: fixed mooring

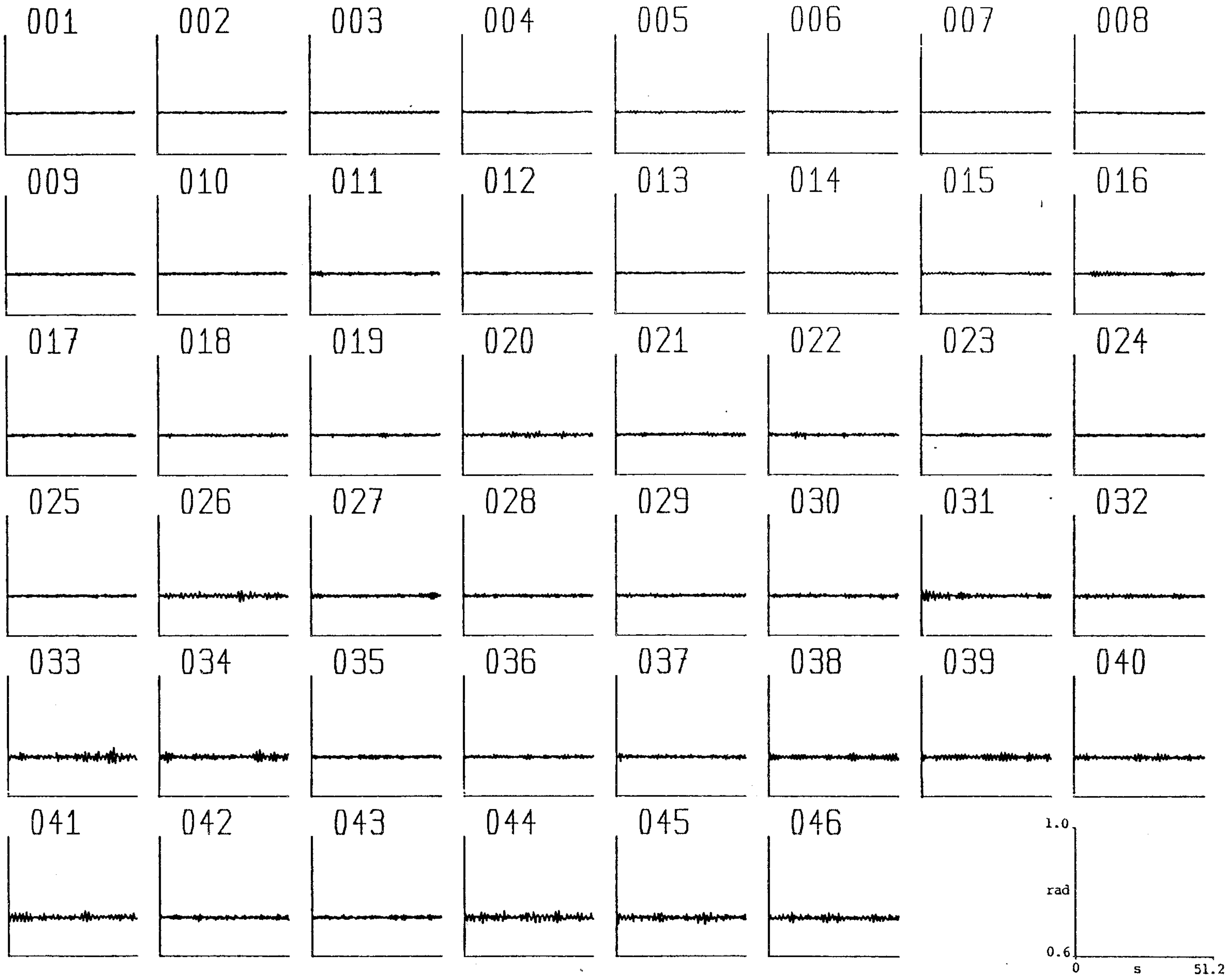

Figure 3.22 46 Spectra. Fore base angle: fixed mooring

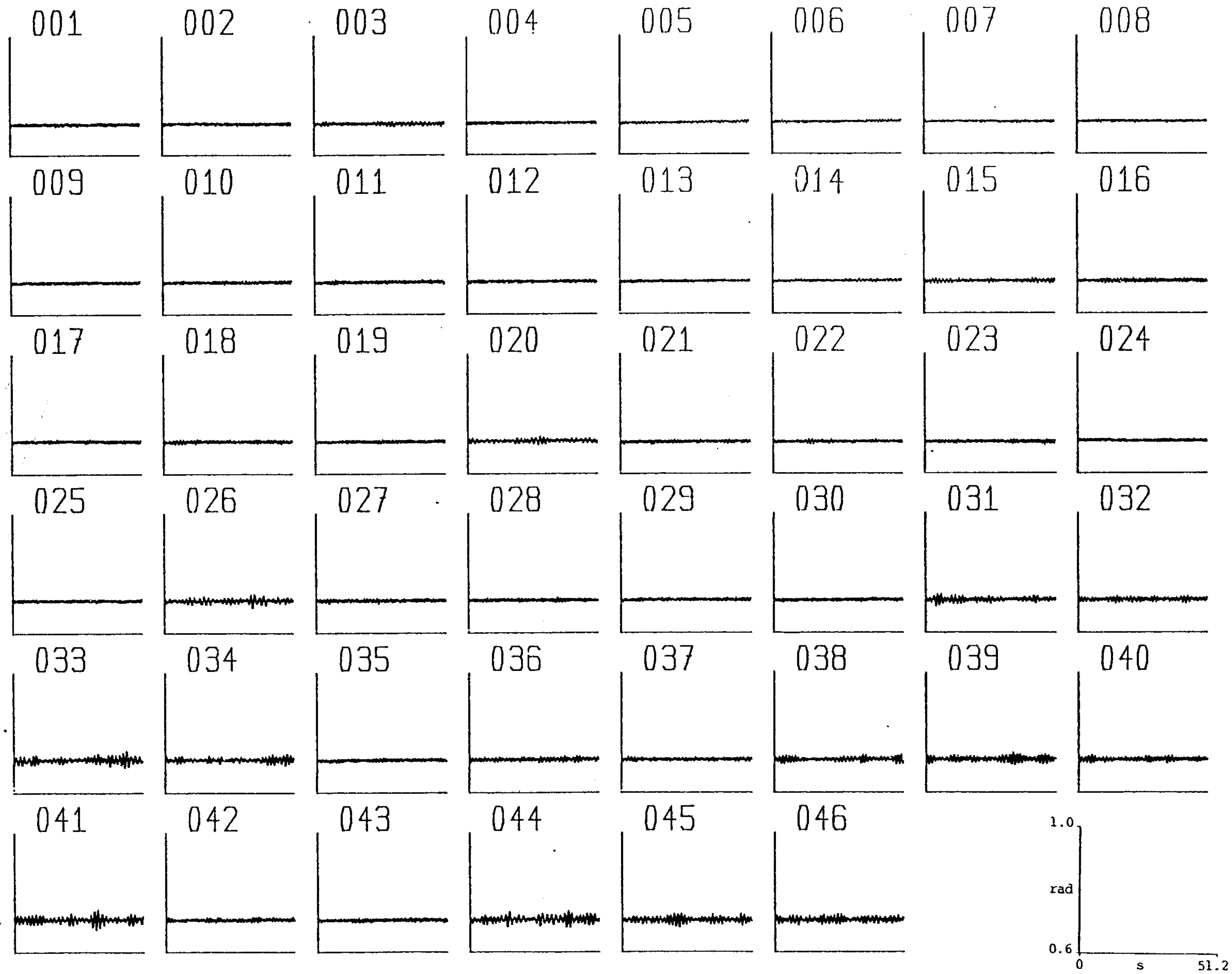

Figure 3.23 46 Spectra. Aft base angle: fixed mooring

TABLE 3.3 ANNUAL WEIGHTED AVERAGES FOR THE FIXED MOORING

MOORING TENSIONS (millinewtons)

tension	calm-water value	mean value	standard deviation
fore	634	631	9
aft	613	612	7

MOORING ANGLES (milliradians)

angle	calm-water value	mean value	standard deviation
fore	707	728	3
aft	663	697	4

SECTION 4 FATIGUE

A criterion of engineering design is that loads are kept not merely within the bounds of the static strength of the structure under consideration, but also within the limits determined by the cyclic loading, which may be many times lower.

The mooring rodes themselves may easily be made fatigue resistant enough against the tension changes in them, which are typically 3% of the static tension. Likewise, the attachments to the float, sinker and anchor can be designed to resist the bending, tension and fretting loads.

The most vulnerable components are the electrical down-feeder cables which require special care to protect them against bending fatigue. If a loose cable, dangling at random were used to connect the spine to a fixed point on the sea bed, fatigue would rapidly occur at the junction of flexible and rigid parts because deflections would be concentrated at that point.

However, if the deflections were distributed evenly over a length of cable, bending strain and hence fatigue could be reduced to arbitrarily low values. We envisage a cable geometry identical to that of the mooring with tension maintained in the same way by floats and sinkers. Deflection of the cable is controlled by the elbow joint shown in exploded form in figure 4.1. It consists of two tetrahedral frames pinned together. The lower member of each frame is split to allow the cable to pass inside it, where it is clamped along the lower half its length. The upper half of the member is flared with a defined radius of curvature to keep bending within the endurance limit of the cable. Between the frames the cable is formed into helical loops. The more loops, and the larger the diameter, the less the fatigue in the cable. In this study, we take the bend to be confined to one and a quarter turns on a 3 metre diameter form, and that the strain is equally distributed around this circumference. The cable diameter is taken to be a typical value for a 138 kV cable, namely four and a half inches, or 114.3 mm.

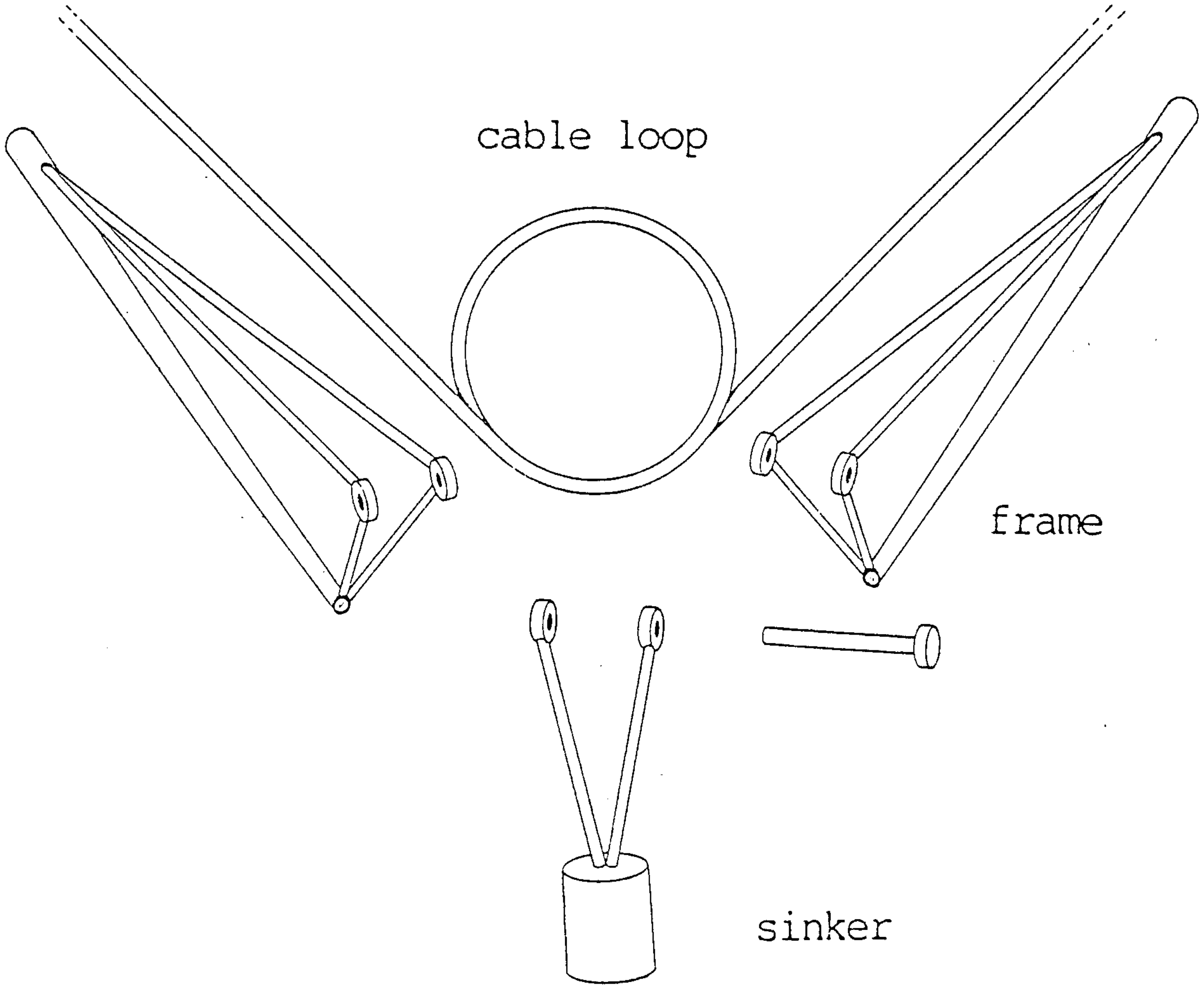

Figure 4.1 Exploded view of cable elbow joint

The frames are designed to be neutrally buoyant. A sinker or a float attached to the yoke on the hinge pin line applies a steady tension to the cable. Wave forces on the spine and mooring will cause small variations of the tension. The length of the frames is chosen so that this tension variation acting on the lever arm of the frame produces enough torque to deflect the loops through the required angle. The cable can therefore only bend within the confines of the elbow joint and the bending strain is spread over sufficient of its length to reduce fatigue to any level deemed necessary.

The results of the experiment with the 46 spectra become the input for the fatigue calculations. Since the greatest angular variation was found for the fore second angle (opposite the float), we concentrated attention on that one.

To illustrate the method we take the mooring angle records for sea number 38 as an example. Figure 4.2 shows the time series of the angle, and figure 4.3 shows the modulus of the Fourier transform. Each tooth of the transform is assigned to a histogram cell according to its size, and the cell population is increased by the number of cycles due to that frequency in the sampling period. Note that this method therefore ignores any steady state component; hence, in the example transform of figure 4.3 the DC component has not been indicated.

This process is performed for each of the 46 seas in turn, where the addition to each histogram cell is multiplied by a factor incorporating model scale, the number of seconds in a year, and the weighting of each sea state. The result is a graph in which the size of histogram cells is plotted vertically on a linear scale against a horizontal scale of the logarithm of the total number of cycles in that cell. This is analogous to the standard S/N curves drawn by materials scientists to illustrate the lifetime of a component at given strain levels. However, ours represents not the limit of failure, but the limit of the experienced loads.

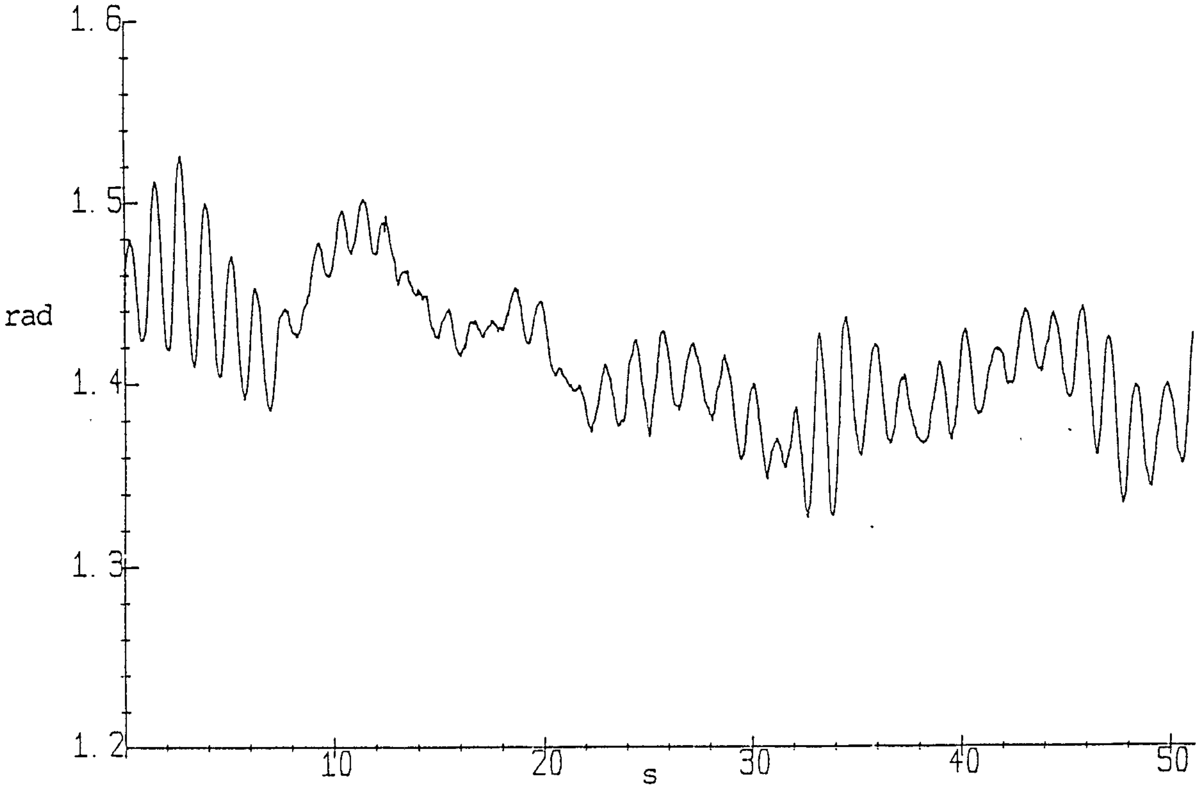

Figure 4.2 Fore second angle: time series

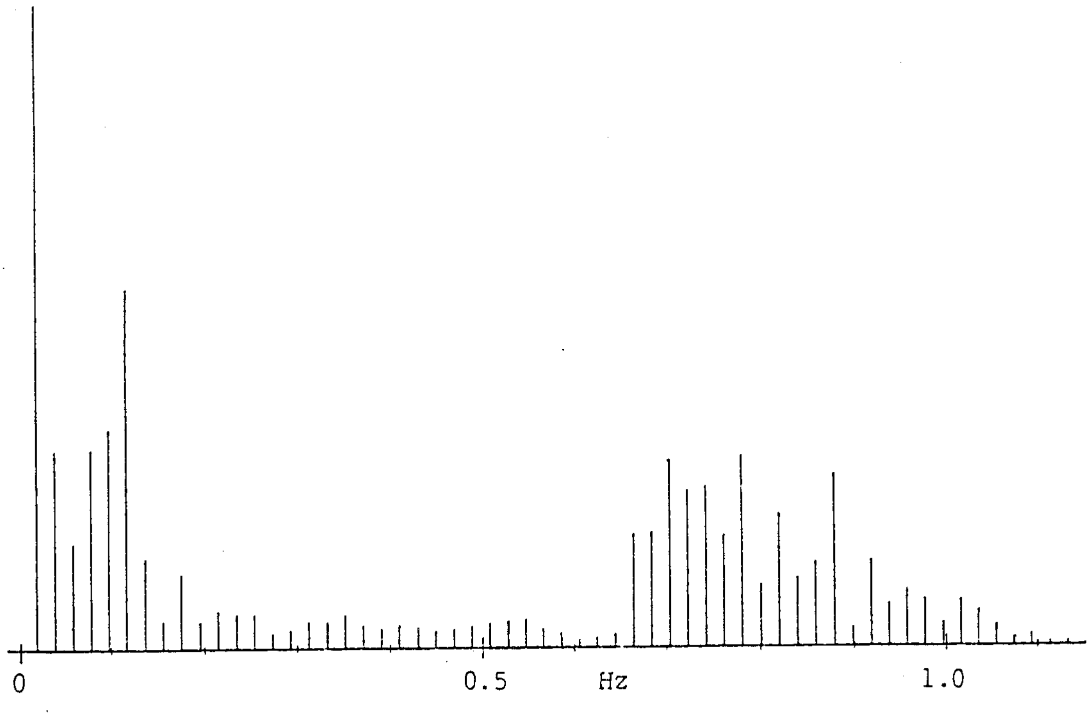

Figure 4.3 Fore second angle: Fourier transform

One must be cautious when using Fourier transform techniques. If an input frequency lies between two teeth, it will be shared between them, and to a lesser extent, more distant teeth.

Figure 4.4 shows how the Fourier distribution of an oscillation changes as its frequency is changed, in ten steps, from exactly coincident with one tooth (at 0.9961 Hz) to exactly coincident with the next one (at 1.0156 Hz). The rule is that the sum of the squares of the teeth (ie their energies) remains equal to that input.

When the input frequency is exactly between two teeth, the smearing effect is a maximum: the side bands are at a maximum, and the two central teeth have dropped in value by a factor of 1.56.

The effect of this smearing on the construction of the histogram will be - at worst - to reduce the maximum size of cell by a factor of 1.56; and to increase the population of smaller cells. To be on the safe side, we should multiply the vertical scale by 1.56. If we leave the horizontal scale the same, we overestimate the low amplitude cells. These will also contain the residual noise of the sampled channels; the lowest cell is therefore best disregarded.

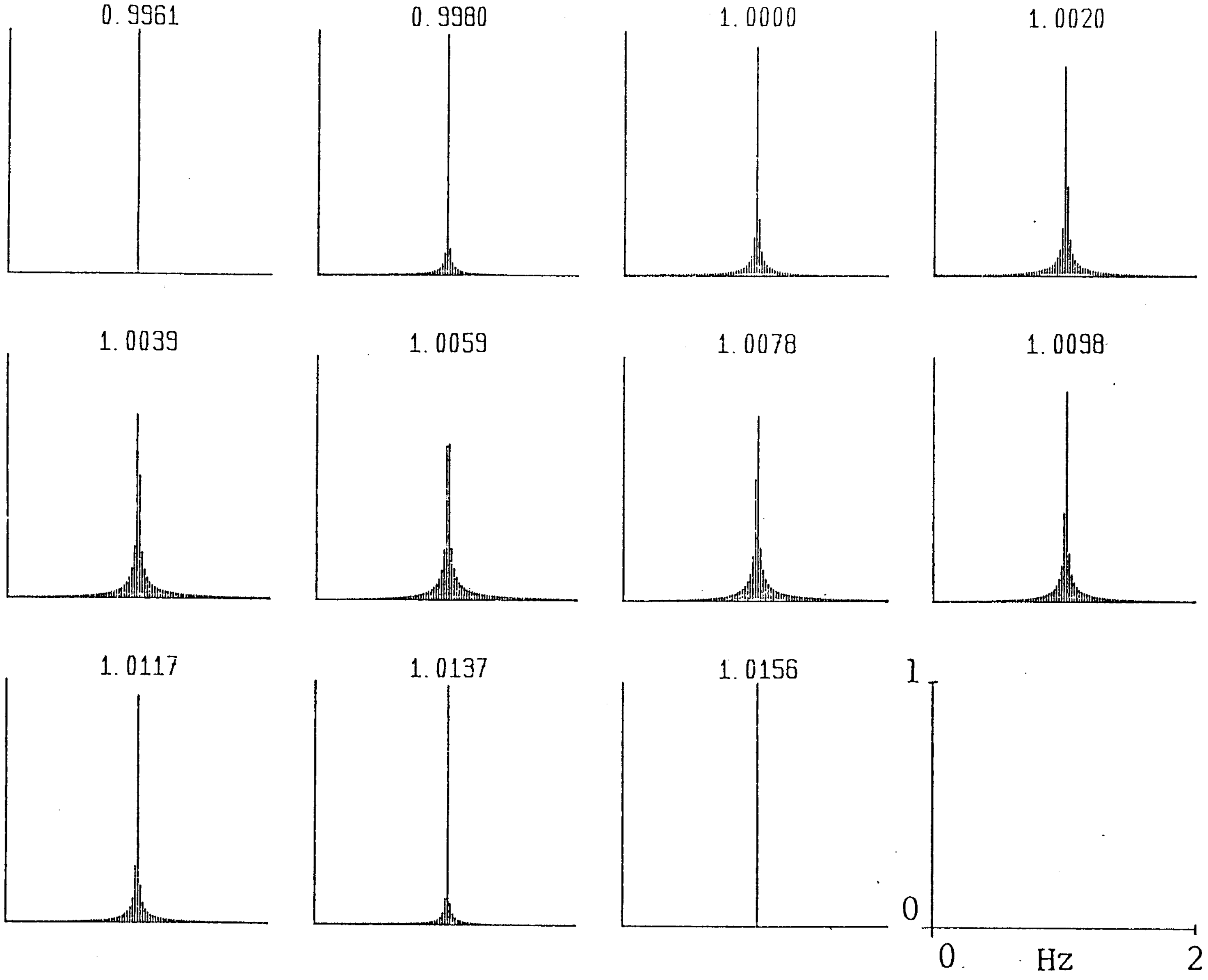

Figure 4.4 Fourier transform of ´between tooth´ frequencies

Figure 4.5 shows the final graph of cycles for the fore second angle over a period of 25 years. The maximum angle is below 100 milliradians - about 6 degrees.

It is possible to calculate the corresponding amount of strain for the cable in question from the cable parameters and experienced angle according to the formula:

$$\text{strain} = \frac{d\,A}{2\,\text{pi}\,D\,N}$$

A = angle
d = cable diameter = 114.3 mm
D = bending diameter = 3.0 m
N = number of turns = 1.25

The corresponding strain is indicated on the right hand scale of the graph. The maximum is less than 500 microstrain - a very low level. Experiments carried out by Pirelli (reference 2) on cable fatigue in sea water at 40 thousand microstrain showed levels of failure at between 1 and 10 million cycles. The cable harness joint ensures that for 25 years in the South Uist wave climate cycle numbers higher than 10 million will only be associated with less than 100 microstrain.

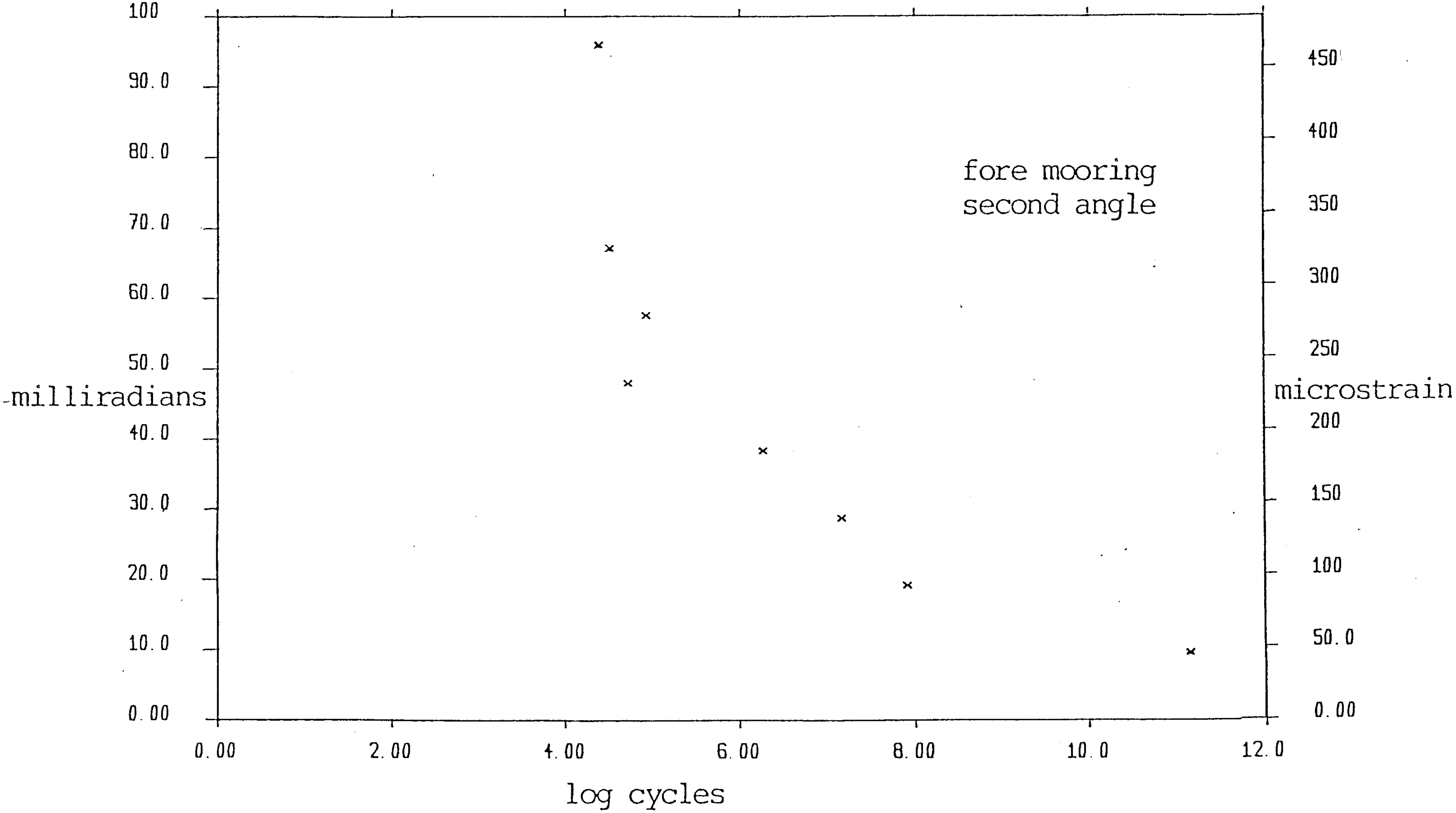

Figure 4.5 Mooring angle cycles over 25 years

SECTION 5 THE APPENDICES

APPENDIX A THE ANCHOR GAUGE

The anchor gauge consists of a length of 1/4" square-section light alloy bar clamped at one end, and ballasted by a massive steel plate. Sets of strain gauges, cemented to the bar with oven-cured epoxy, are arranged in pairs on each face. The two pairs of gauges on opposite faces are connected in bridge arrangement and supplied from a constant voltage source in a separate box of conditioning circuitry. A schematic diagram of the electronics is shown in in figure 5.1.

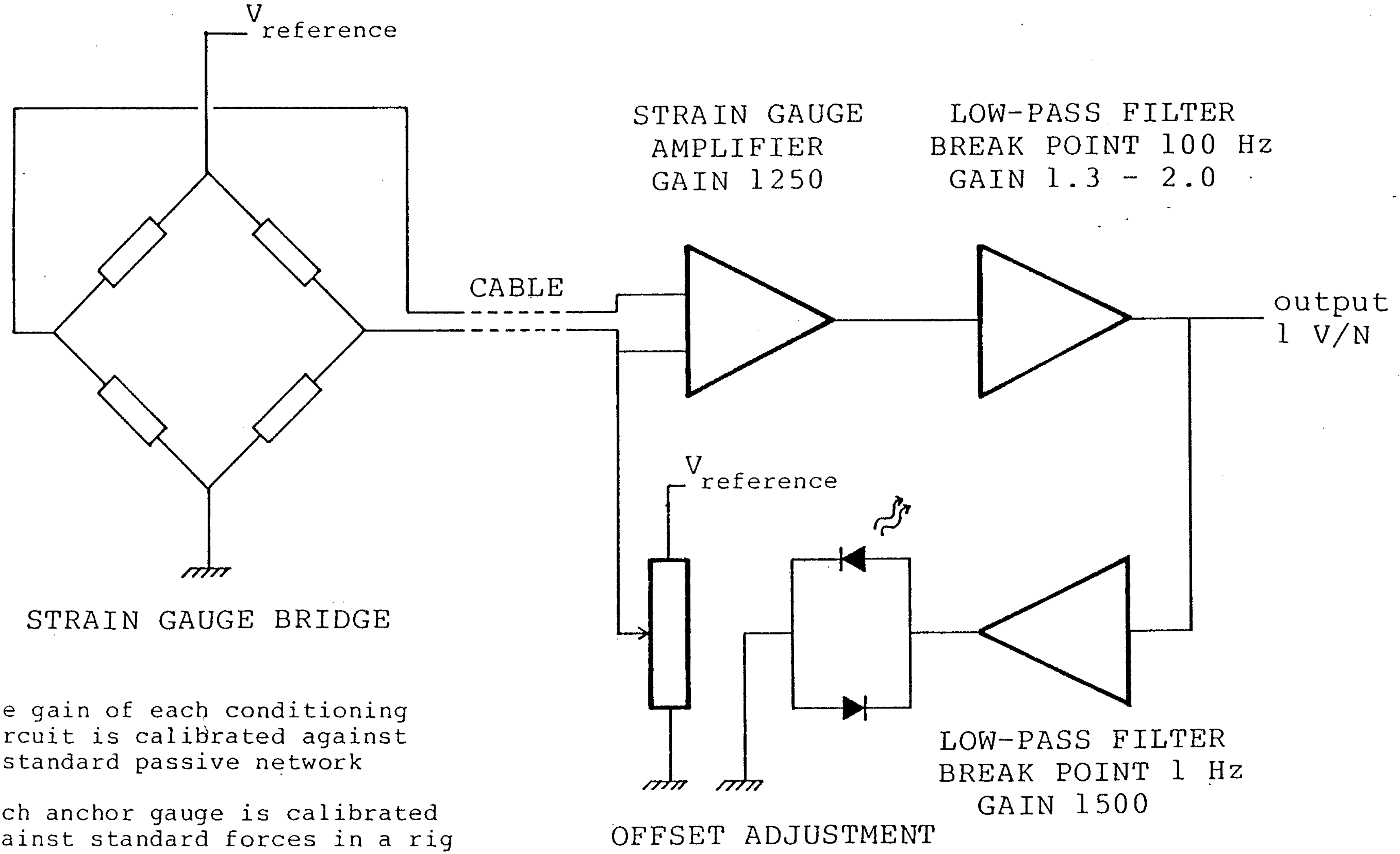

The gain of each conditioning circuit is calibrated against a standard passive network

Each anchor gauge is calibrated against standard forces in a rig

Resistors are added in its plug to parallel either the input or feedback resistor of the second operational amplifier until the correct calibration is achieved

Both LEDs unlit at balance point

Figure 5.1 Schema of anchor gauge electronics

A close-up photograph of the bar shows the disposition of the wiring and the strain gauges. They are covered with flowable RTV silicone rubber to prevent ingress of water, with heat-shrunk plastic over the top for mechanical protection. The wiring is connected to the exit cable via a small piece of ´Veroboard´ which is both insulated and waterproofed by embedding it in more silicone rubber which fills a recess milled into the base.

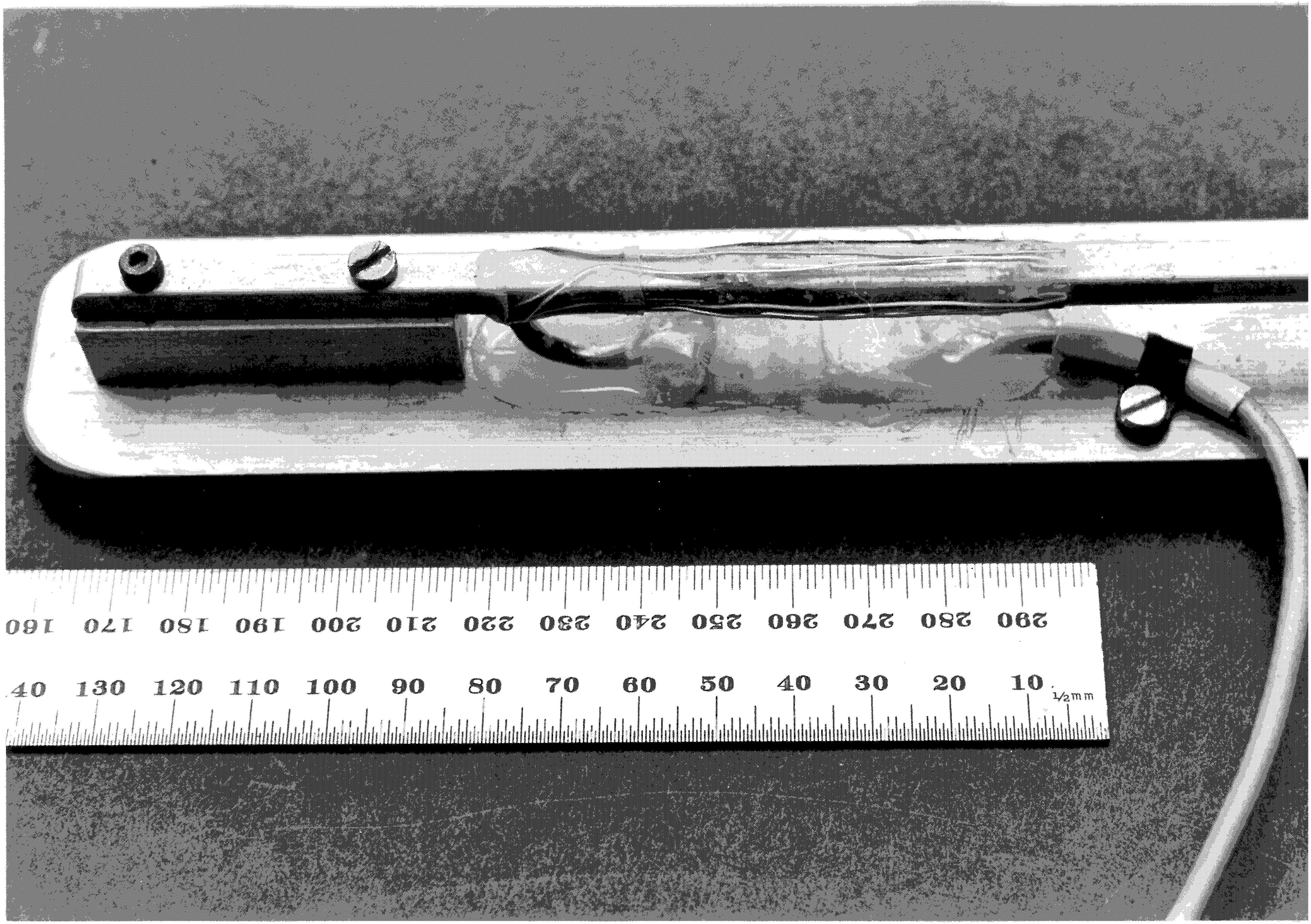
160 170 180 190 200 210 220 230 240 250 260 270 280 290
140 130 120 110 100 90 80 70 60 50 40 30 20 10
½mm

The final assembly. The ´U´ shaped loop allows convenient retrieval with a boat hook. The guard ring around the moving end of the bar acts as a strain limiter to protect the gauge during handling.

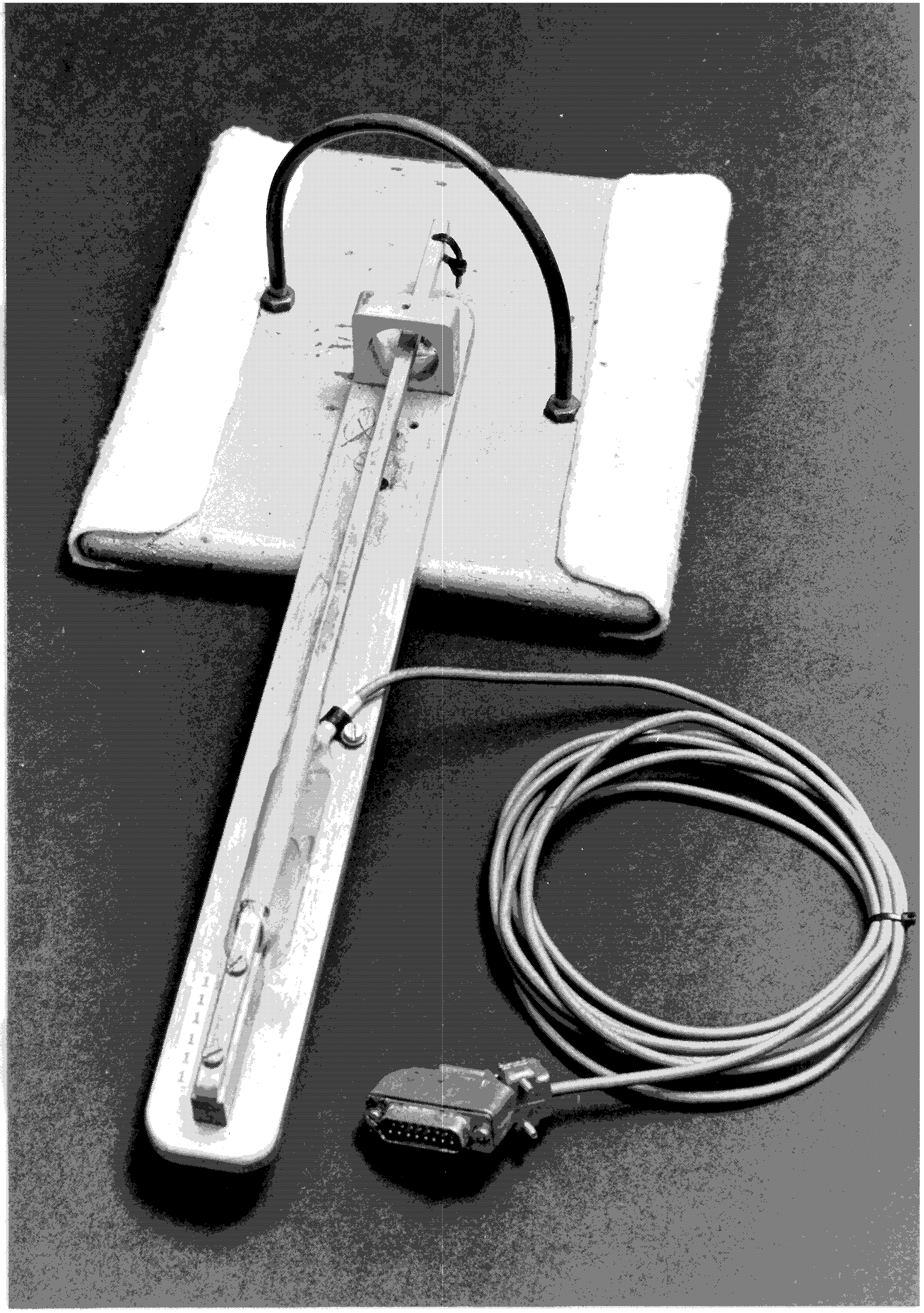

The bars are calibrated in a rig which applies known weights, and hence forces, via pulleys to each direction (up, down, left, right) which define the orthogonal ´x´ and ´y´ axes. Trim resistors are placed in the plug which connects the gauge to the conditioning box. Trimming is done in the plug so that any gauge may be connected to any box without need for recalibration.

The signal conditioning requires electronic offsets to be nulled before an experiment begins. The nulling is done with the anchor gauge in the water, so that the force due to the buoyancy of the bar is discounted.

The accuracy of the construction geometry was checked in the following way. A calibrated bar was placed in the chuck of a dividing-head. The head reading was set to zero degrees, and the bar levelled. A weight was then attached to the gauge end, and the dividing-head rotated from zero to ninety degrees, so that the force due to the weight was gradually shifted from the ´y´ to the ´x´ axis. Readings of strain were taken in each axis at one degree intervals. Table 5.1 shows the angle read from the dividing-head scale, the measured ´y´ and ´x´ strains, and the angle calculated from the arctan of the strain ratio of the two axes. The agreement of the measured and calculated angles is very close - over the whole range, there is a mean error of 0.2 degrees. In the discussion below, this is compared with the contribution due to other errors.

TABLE 5.1 ANCHOR GAUGE ANGLE LINEARITY

MEASURED ANGLE	HEAVE FORCE mN	SURGE FORCE mN	CALCULATED ANGLE
0	0	1163	0.0
5	90	1160	4.5
10	193	1145	9.6
15	290	1123	14.6
20	387	1093	19.6
25	482	1055	24.7
30	575	1008	29.8
35	661	953	34.9
40	741	891	39.9
45	817	823	44.9
50	887	747	50.0
55	947	661	55.2
60	1003	581	60.0
65	1052	488	65.2
70	1090	394	70.2
75	1119	299	75.1
80	1142	199	80.2
85	1153	100	85.1
90	1157	0	90.0

A 1 Newton weight was used as the deflection force. The maximum reading in heave or surge should therefore be 1000 mN. The difference (some 160 mN) is due to the weight of the bar.

Note that electronic offsets have been removed so that heave force is zero at zero degrees, and surge force is zero at 90 degrees.

The calculated angle is derived from the expression:

$$\text{angle} = \arctan\left[\frac{\text{x reading}}{\text{y reading}} \cdot \frac{1163}{1157}\right]$$

where the factor $\frac{1163}{1157}$ corrects for the calibration difference between the two channels.

ERROR CONTRIBUTIONS TO TENSION MEASUREMENT

1) The gauges were calibrated to within 1% of the nominal 1 Newton per Volt.

2) The gauges and their conditioning boxes exhibited a drift of, at the most, 0.5 mN over the course of a two hour experiment.

3) The worst-case root-mean-square noise in the system corresponded to 2 mN.

The first two items should be referred to the standing tension in the mooring lines when the system is at rest, namely, about 600 mN.

The noise should be compared with the alternating signals measured in the experiments. The South Uist spectra experiments produced tensions over the range 5 - 35 mN rms.

ERROR CONTRIBUTIONS TO ANGLE MEASUREMENT

1) A 1% difference in reading between the ´x´ and ´y´ axes of the anchor gauge corresponds to an error of 0.3 degrees at 45 degrees, dropping to 0.2 degrees at 22.5 and 67.5 degrees.

2) The dividing-head experiment showed a mean error of 0.2 degrees over the 0 - 90 degree range. Peak error was 0.5 degrees.

3) The worst-case noise in the system was equivalent to 0.1 degrees rms.

The first two points should be compared with the static angle of the mooring in the rest position, about 40 degrees.

The noise should be compared with the angles measured in experiments. In the South Uist 46 spectra the range covered .15 to 1.5 degrees rms.

APPENDIX B THE POSITION GAUGE

The position gauge is mounted in a plane normal to the long axis of the spine, and measures motion in that plane of the spine joint to which it is attached. The arrangement is shown schematically in figure 5.2

The cross-beam is clamped to the underside of the wireless mast, and is adjusted to be level when the spine is in the water. The fore and aft gauges are fixed on the cross-beam about 2 m apart, with a plumb bob exactly halfway between them. They have no components in common, and are identical. Each comprises:

a) a nylon line attached by a magnet to a spine joiner ring.

b) a worm pulley, motor, and optical rotation sensor.

c) an electronics board for signal conditioning and digital processing.

These are shown in the following photographs.

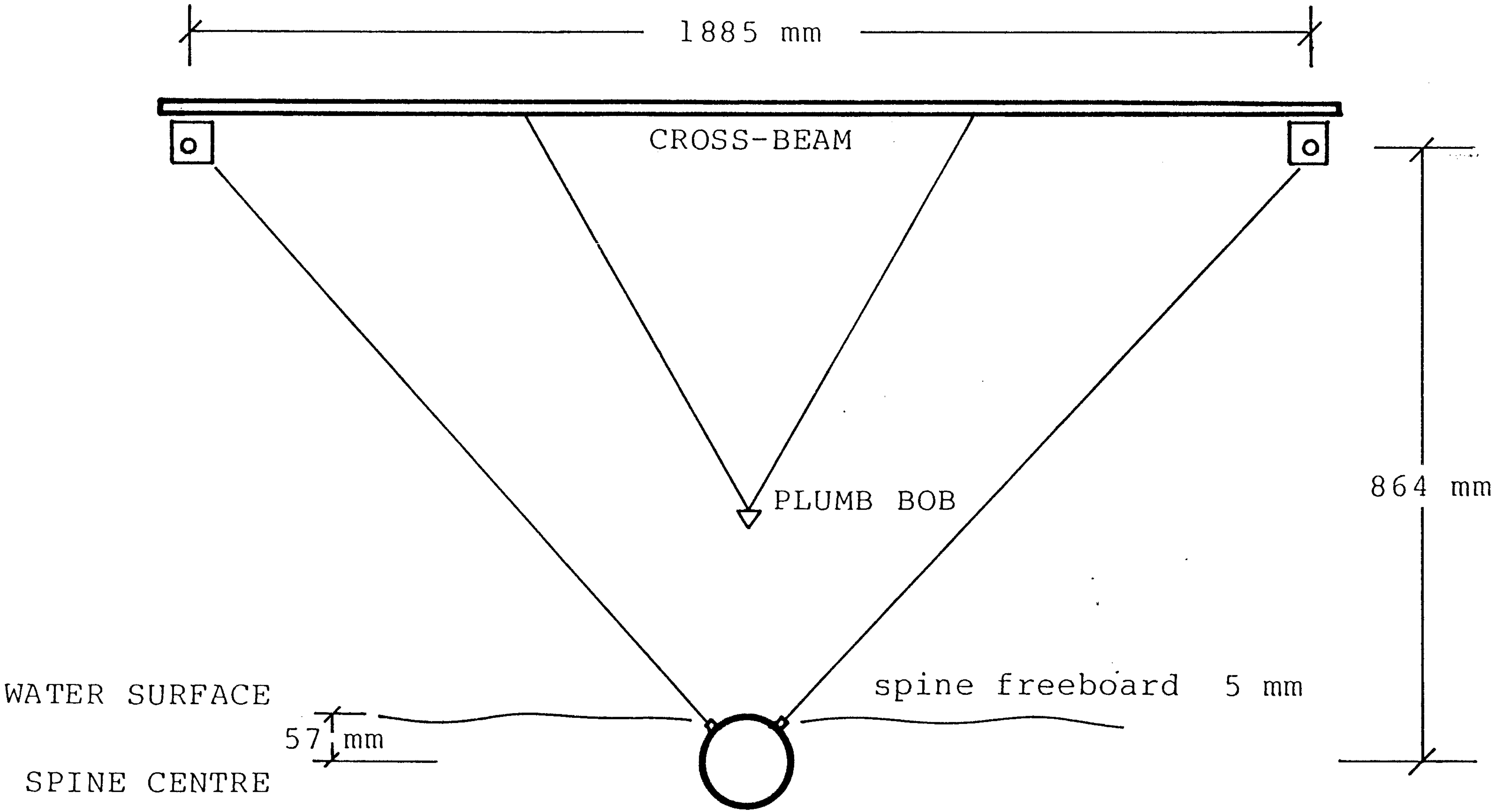

Figure 5.2 Side elevation of position gauge arrangement

The photograph shows the fore and aft lines of the position gauge. They attach to the spine by cylindrical magnets engaging with steel inserts in the spine joiner ring.

Also shown in the photograph are the power and signal cables for the spine on the left, and for the duck on the right.

The transparent tubing on the right carries a dry air supply to each spine unit to keep the interior flushed, and pressurized against water ingress.

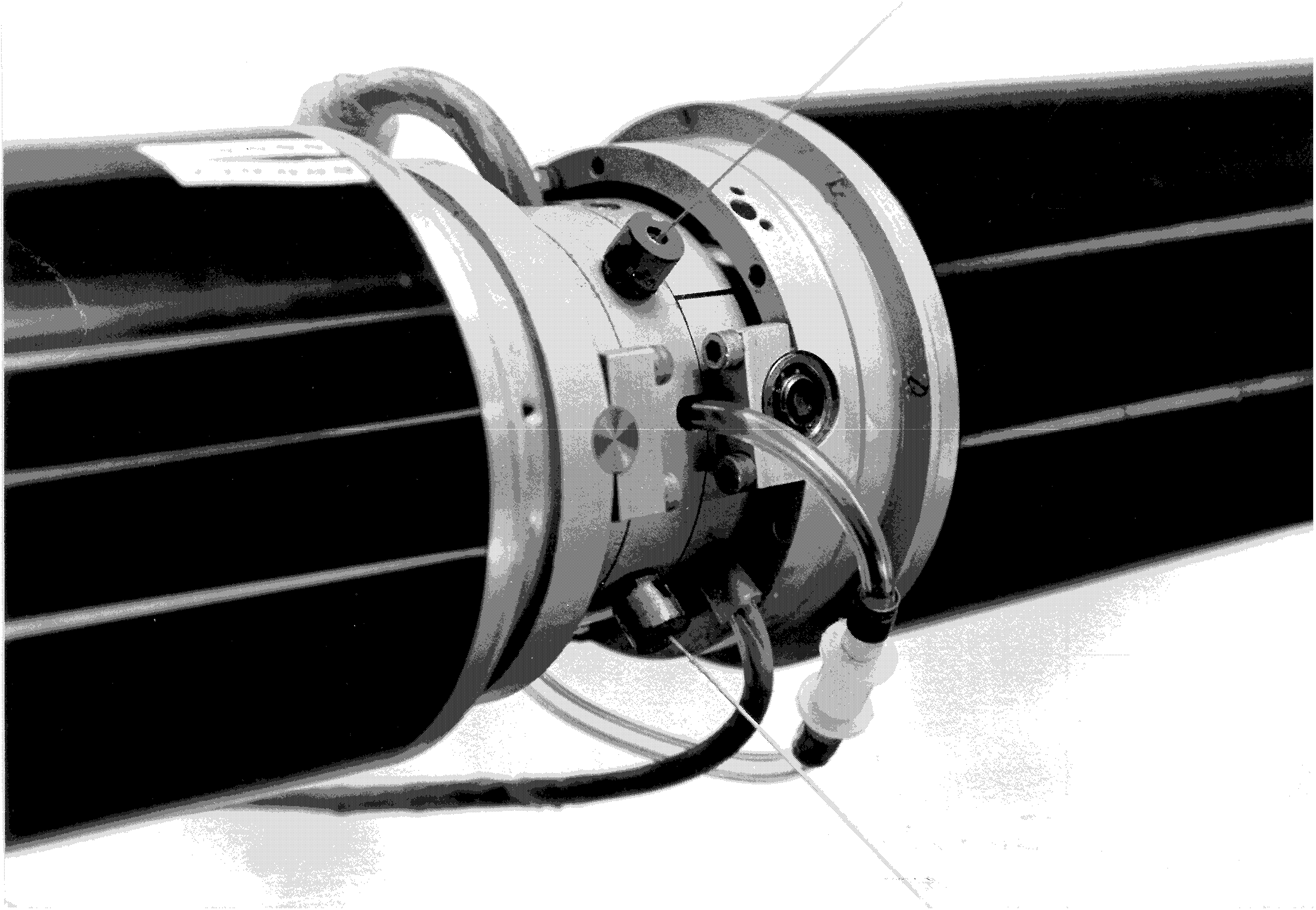

The photograph shows the position gauge assembly mounted on the wireless mast.

From the right are shown:

the worm pulley and nylon line

the motor, providing the line tension

the tachogenerator, for sensing the motor velocity

the optical encoder, for sensing the motor rotation.

Above, the analog and digital electronics.

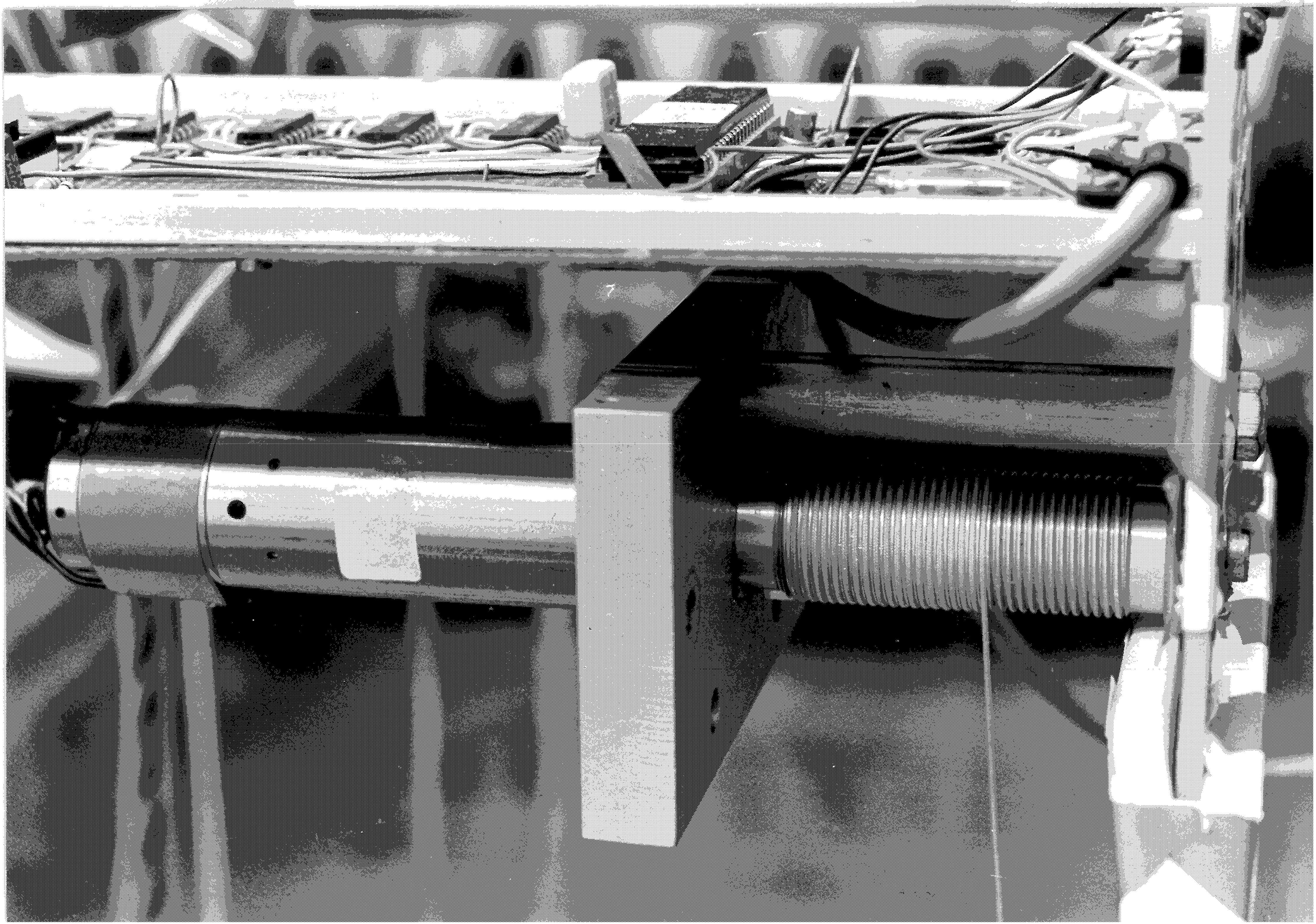

The arrangement of the gauge components is shown schematically in figure 5.3.

The nylon line attaches with a magnet to a steel insert in the aluminium alloy spine joiner ring. At the other end it winds on to a 19 mm diameter precision turned worm pulley which is mounted directly on the shaft of a low inertia DC motor. The line is kept taut by a constant current of 70 mA supplied to the motor. To compensate for brush friction, a further current of 13 mA is superimposed on the 70 mA. The 13 mA is switched positive when the tachogenerator mounted on the motor senses that the line is contracting, and switched negative when the line is extending.

By contrast, the Selspot technique is optical, uses no tie lines, and therefore induces no error forces. However, Selspot is more suitable for models which are never obscured by water - and our spines are frequently fully immersed.

The line tension was chosen to be the minimum required to accelerate the line sufficiently, and corresponded to 0.006 of the buoyancy of a single spine section. The tension cancels the weight of the magnetic quick-release which couples the instrument to the joiner ring, and the freeboard is therefore unaffected. Brush friction would have contributed a corrupting force of about 0.001 ot the buoyancy force. We believe that the positive velocity feedback reduces this by at least a factor of 10.

The optical rotation sensor comprises photo-emitter and sensor diodes arranged either side of a transparent disk printed with two concentric optical tracks. Each track contains 120 lines per revolution, and the inner is staggered from the outer by half a line width. Consequently, as the assembly rotates, the photodetectors produce two sine wave signals in quadrature.

The first stage of the electronics, the discriminator, amplifies and clips these signals to quadrature square waves at logic level. From these the ´X 2 circuit´ produces a frequency-doubled 240 counts/revolution signal line,

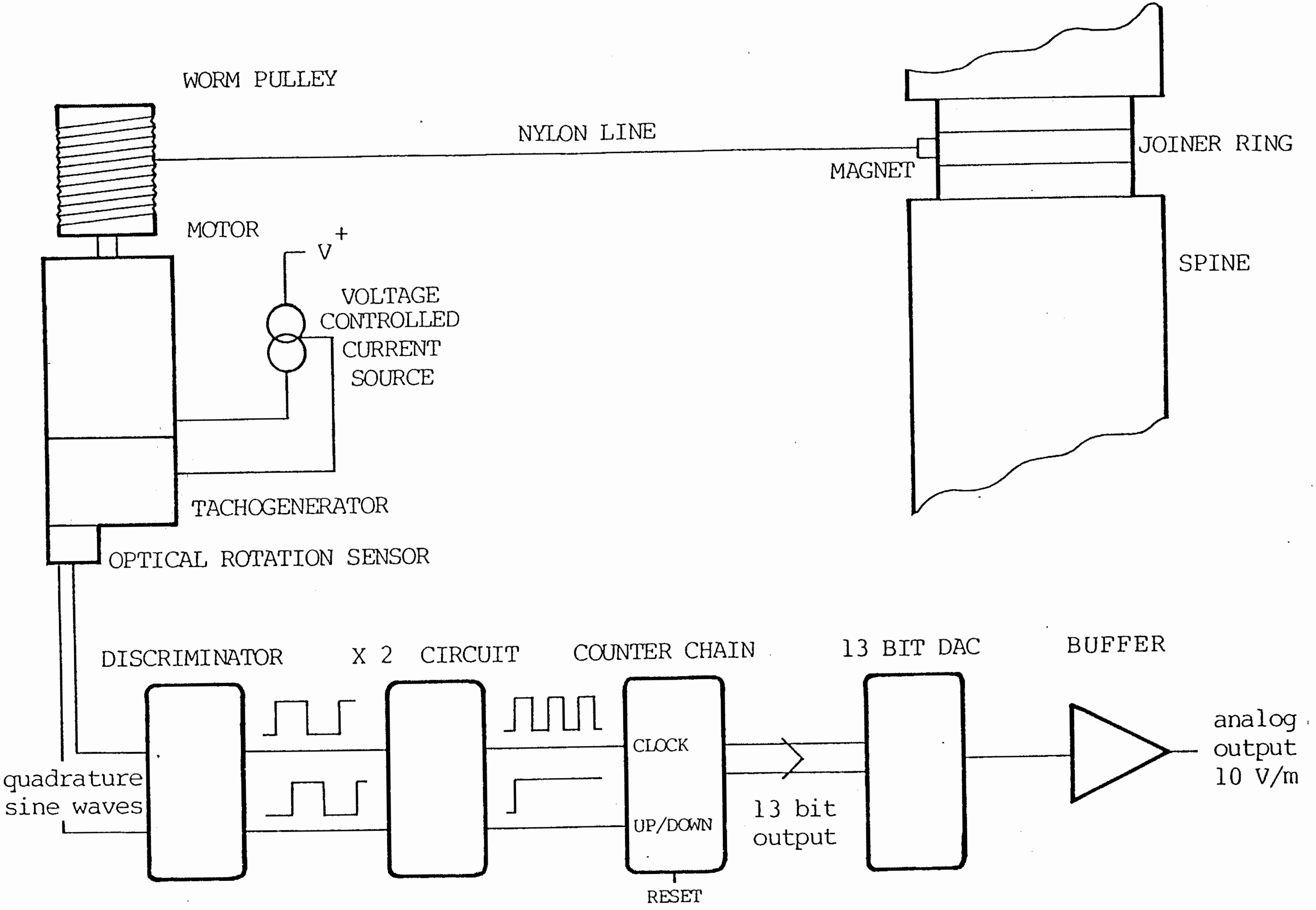

Figure 5.3 Schema of position gauge electronics

and a direction sensing 'up/down' control line. These pass to a counter chain, the outputs of which go to a 13-bit digital-to-analog convertor which passes via an op-amp to a multiplex board, and is routed to the control desk and computer.

The resolution of the apparatus is 0.25 mm; the 13 bit counter therefore allows for plus/minus 1.024 m displacement of a line. The final calibration is set by the output op-amp to be 10 V/m.

In use, the spine is lowered into the water and the wireless mast is shifted until the plumb bob is located over the centre of the spine. The counters are set to zero by momentarily depriving them of the multiplex clock signal, and a short program is run to set the linear offsets. Time series for the fore and aft gauges may then be sampled.

Figure 5.4 shows the geometry for the gauge, and beneath is the algebraic derivation of heave and surge displacement, given the fore and aft signals.

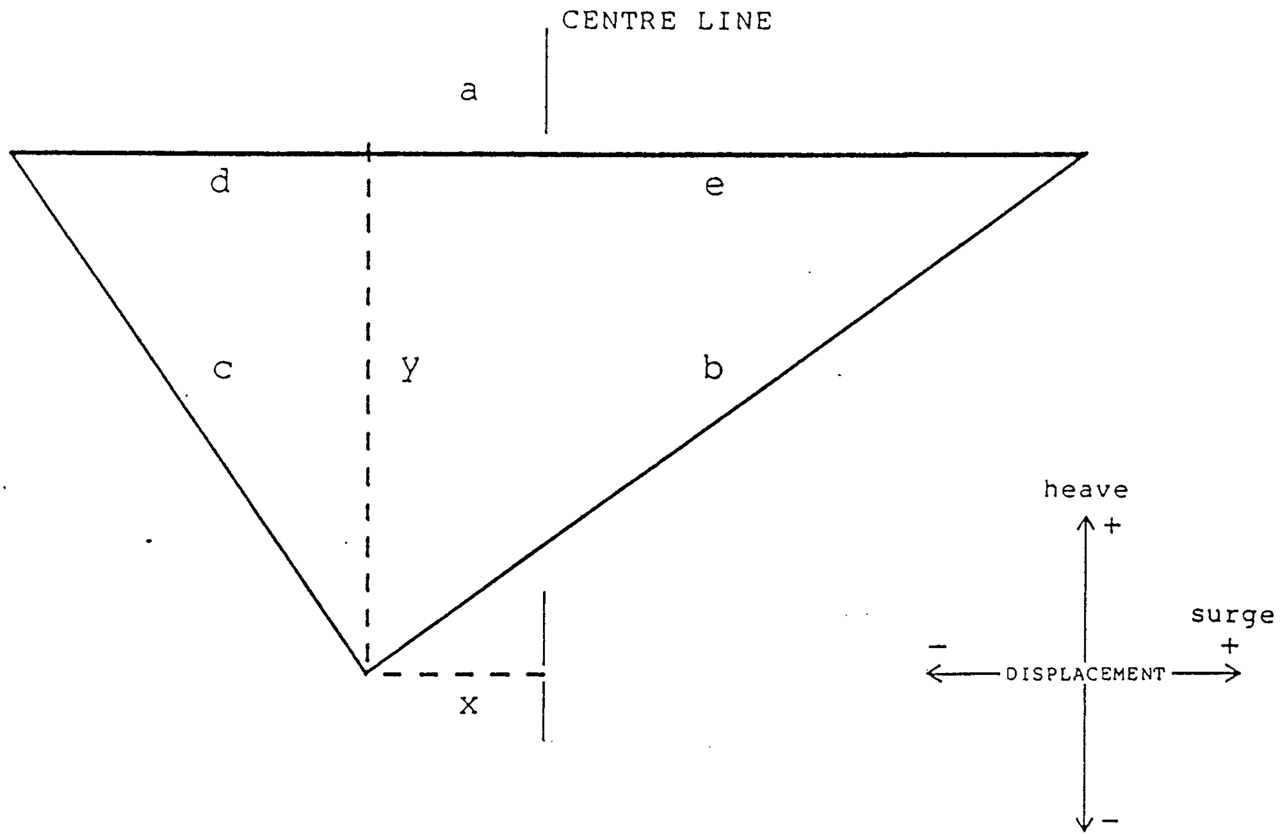

Figure 5.4 Position gauge geometry

Considering the triangles 'cdy' and 'eby', by Pythagoras:

$$(1) \qquad y^2 = c^2 - d^2 = b^2 - e^2$$

substituting $d = \frac{a}{2} - x$ and $e = \frac{a}{2} + x$ into (1) gives:

$$(2) \qquad c^2 - \left(\frac{a}{2} - x\right)^2 = b^2 - \left(\frac{a}{2} + x\right)^2$$

$$(3) \quad b^2 - c^2 = \left(\frac{a^2}{4} + a\,x + x^2\right) - \left(\frac{a^2}{4} - a\,x + x^2\right) = 2\,a\,x$$

Hence $(4) \quad x = \frac{b^2 - c^2}{2\,a}$ and $(5) \quad y = \left[c^2 - \left(\frac{a}{2} - x\right)^2\right]^{1/2}$

Displacement from an arbitrary rest position is calculated by combining these values for x and y with the rest values x_o and y_o. Using the displacement convention shown above:

$$(6) \quad \text{surge} = x_o - x; \qquad (7) \quad \text{heave} = y_o - y$$

APPENDIX C THE MOORING

A side elevation of the mooring line is shown in figure 5.5 with its 3 sections of lines and the float and sinker sized to produce equal up and downthrust of 1.2 Newtons.

TABLE 5.2 FLOAT AND SINKER CHARACTERISTICS

Masses and added masses for the float and sinker

mass of sinker = 145 grams
volume of sinker = 19 millilitres

mass of float (dry) = 23 grams
mass of float (wet) = 32 grams
volume of float = 157 millilitres

upthrust of float = 157 - 32 = 125 grams
downthrust of sinker = 145 - 19 = 126 grams

mass + added mass of sinker = 145 + 19 = 164 grams
mass + added mass of float = 157 + 23 = 180 grams

The added mass calculations assume that both float and sinker have added mass coefficients appropriate to cylinders, namely, 1.

However, the float has rounded edges, and a height to diameter ratio of 1.3 - it bears some comparison to a sphere, for which the coefficient is one half. If value of 0.9 is chosen for the coefficient, the mass plus added mass of the float is 164 grams - the same as for the sinker.

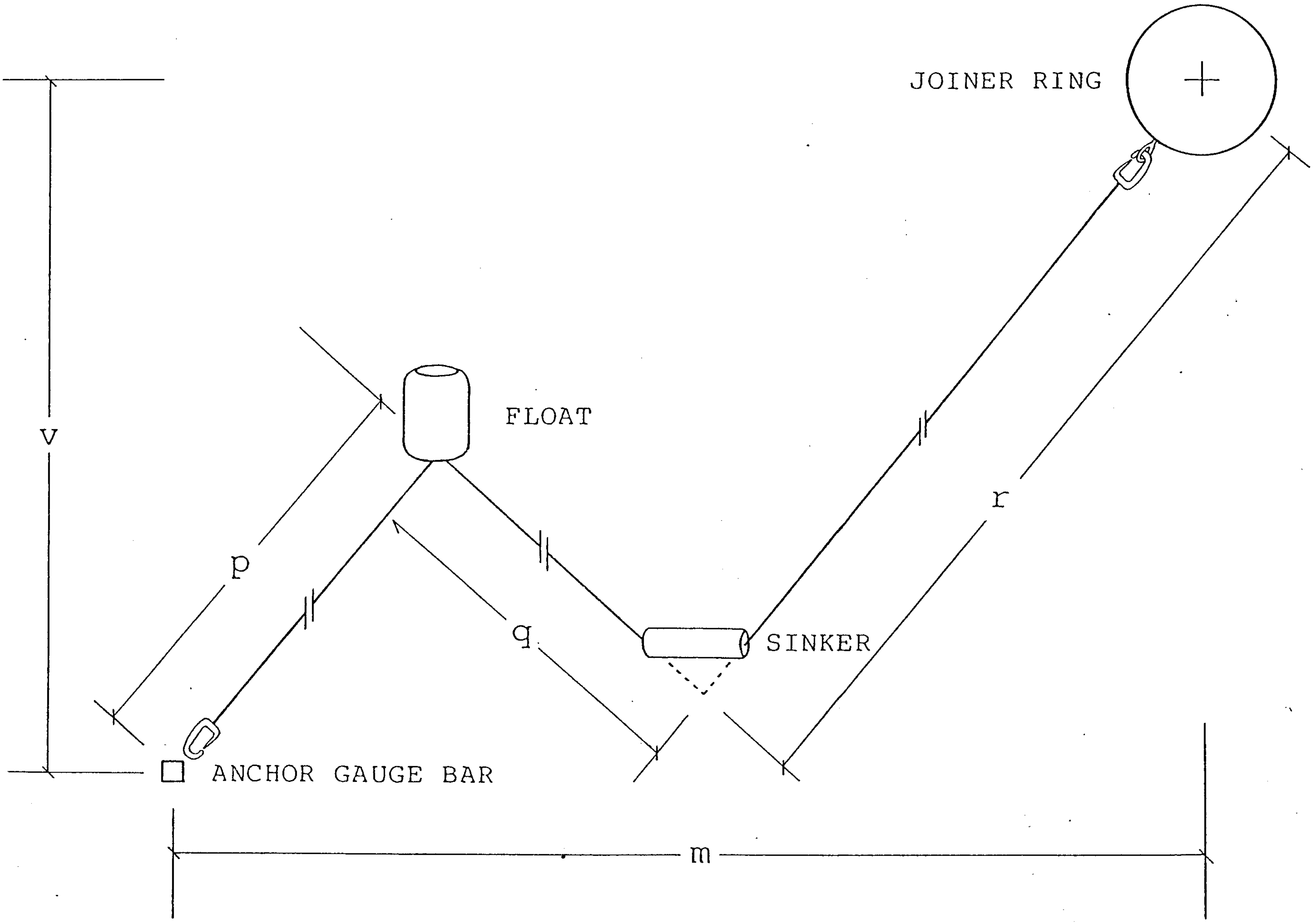

Figure 5.5 Side elevation of mooring line

In figure 5.6, the static force diagram for the float and sinker is drawn, and the algebra follows below. Making the up and downthrusts identical greatly simplifies things - one observes that lengths p and r must be under identical tensions and oriented at the same angle. This allows the equations in the vertical and horizontal axes to have just 2 unknowns - the angles A and B. A solution is therefore possible, following some trigonometrical elimination and rearrangement. The angles are given in equations 22 and 23. From these the tensions in the sections p and r are derived and presented in equations 25 and 26.

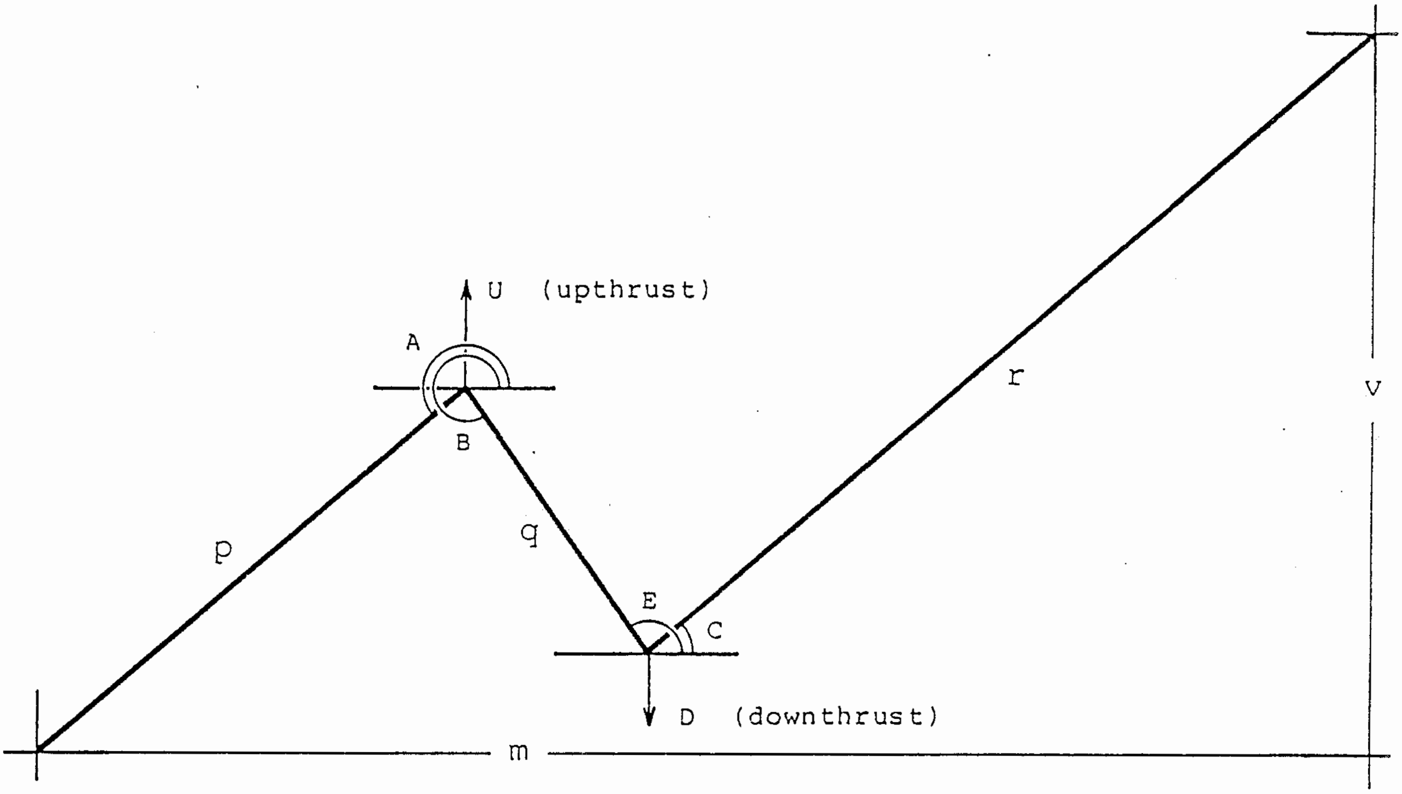

Figure 5.6 Float and sinker static forces

Let T, with its appropriate subscript, represent the tension in each of the sections p, q, r.

x axis (1) $T_p \cos A + T_q \cos B = 0$ (3) $T_q \cos E + T_r \cos C = 0$

y axis (2) $T_p \sin A + T_q \sin B = -U$ (4) $T_q \sin E + T_r \sin C = D$

From the diagram $E = \pi + B$; so adding (1) to (3), and (2) to (4)

(5) $T_p \cos A + T_r \cos C = 0$ (6) $T_p \sin A + T_r \sin C = D - U$

If $U = D$ then:

(7) $T_p \cos A = -T_r \cos C$ (8) $T_p \sin A = -T_r \sin C$

and division of (8) by (7) yields $\tan A = \tan C$, and therefore:

(9) $A = \pi + C$ and (10) $T_p = T_r$

We may refer to the dimensions of fig (1) and write

x axis (11) $-p \cos A + q \cos B + r \cos C = m$

y axis (12) $-p \sin A + q \sin B + r \sin C = v$

Because of (9) we may simplify these as:

(13) $q \cos B + (p+r) \cos C = m$

(14) $q \sin B + (p+r) \sin C = v$

Writing $j = \frac{q}{p+r}$, $k = \frac{m}{p+r}$, $l = \frac{v}{p+r}$,

(15) $\cos C = k - j \cos B$

(16) $\sin C = l - j \sin B$

Squaring and adding (15) and (16)

(17) $1 = k^2 - 2 j k \cos B + j^2 \cos^2 B + l^2 - 2 j l \sin B + j^2 \sin^2 B$

(18) $2 j (k \cos B + l \sin B) = j^2 + k^2 + l^2 - 1$

k and l convert to trigonometric quantities if divided by their modulus, n, where

$n = (k^2 + l^2)^{1/2}$, $\sin D = \frac{k}{n}$, $\cos D = \frac{l}{n}$, $\tan D = \frac{k}{l}$

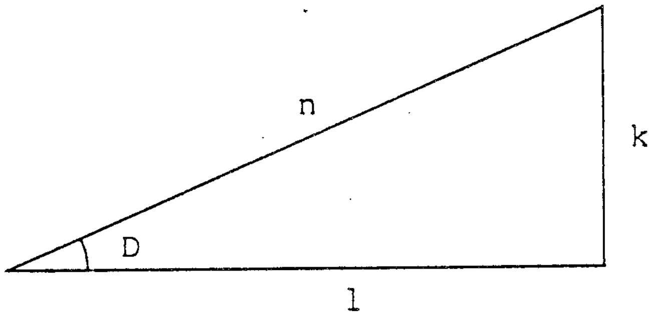

(19) $\frac{k}{n} \cos B + \frac{l}{n} \sin B = \frac{j^2 + k^2 + l^2 - 1}{2 j n} = w$ (say)

(20) $\sin D \cos B + \cos D \sin B = w$

(21) $\sin (B + D) = w$

(22) $B = \arcsin \left[\frac{j^2 + k^2 + l^2 - 1}{2 j (k^2 + l^2)^{1/2}} \right] - \arctan \left[\frac{k}{l} \right]$

From (15)

(23) $C = \arccos (k - j \cos B) = \pi + A$

From (1) $Tp = -Tq \frac{\cos B}{\cos A}$, substituting in (2) yields

(24) $-Tq \cos B \tan A + Tq \sin B = -U$

yielding:

(25) $Tq = U/(\tan A \cos B - \sin B)$, and similarly

(26) $Tp = U/(\tan B \cos A - \sin A)$

The behaviour of the mooring system can be shown by evaluating the expressions for the angle and tension of the base and second sections (p and q) as the mooring length (m) is extended.

Figure 5.7 shows the variation of angle with extension. Note that as extension increases, the angles converge to a common value, at which the line is at full stretch.

Figure 5.8 shows the tension for both lengths. The base tension rises linearly over most of its range. The second tension stays fairly constant. Both rise steeply as the extension reaches its maximum.

The different sections of rode supply the horizontal increase in force and displacement in different ways: in the base section the angle changes slowly and the tension changes fast; but in the second section the angle changes fast and the tension barely at all.

At the point where the angles of the two sections become equal, the algebra indicates that the tensions become infinite, because inextensible rodes were assumed. In practice, the slope of the tension curve will approach the limiting value of the elasticity of the rode material.

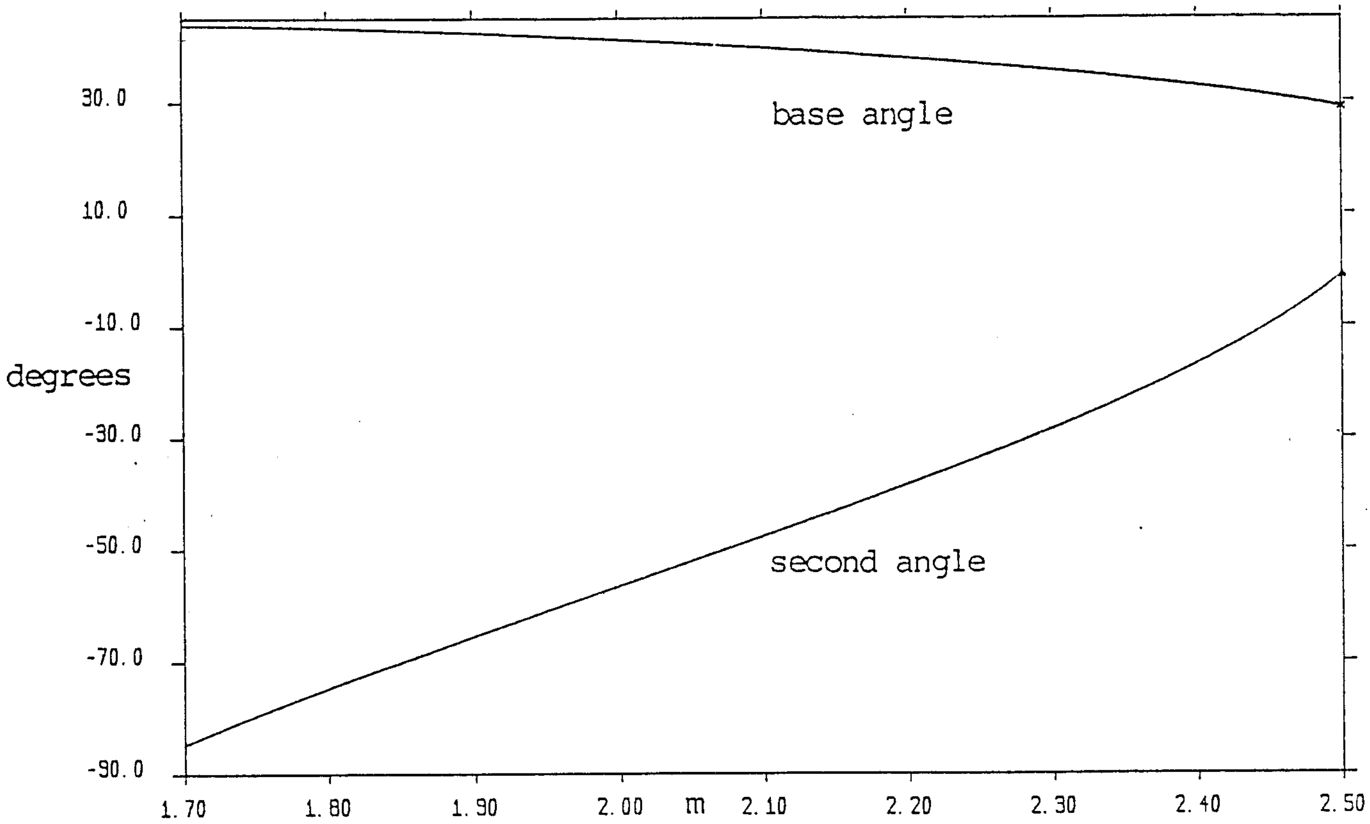

Figure 5.7 Calculated mooring angles versus extension

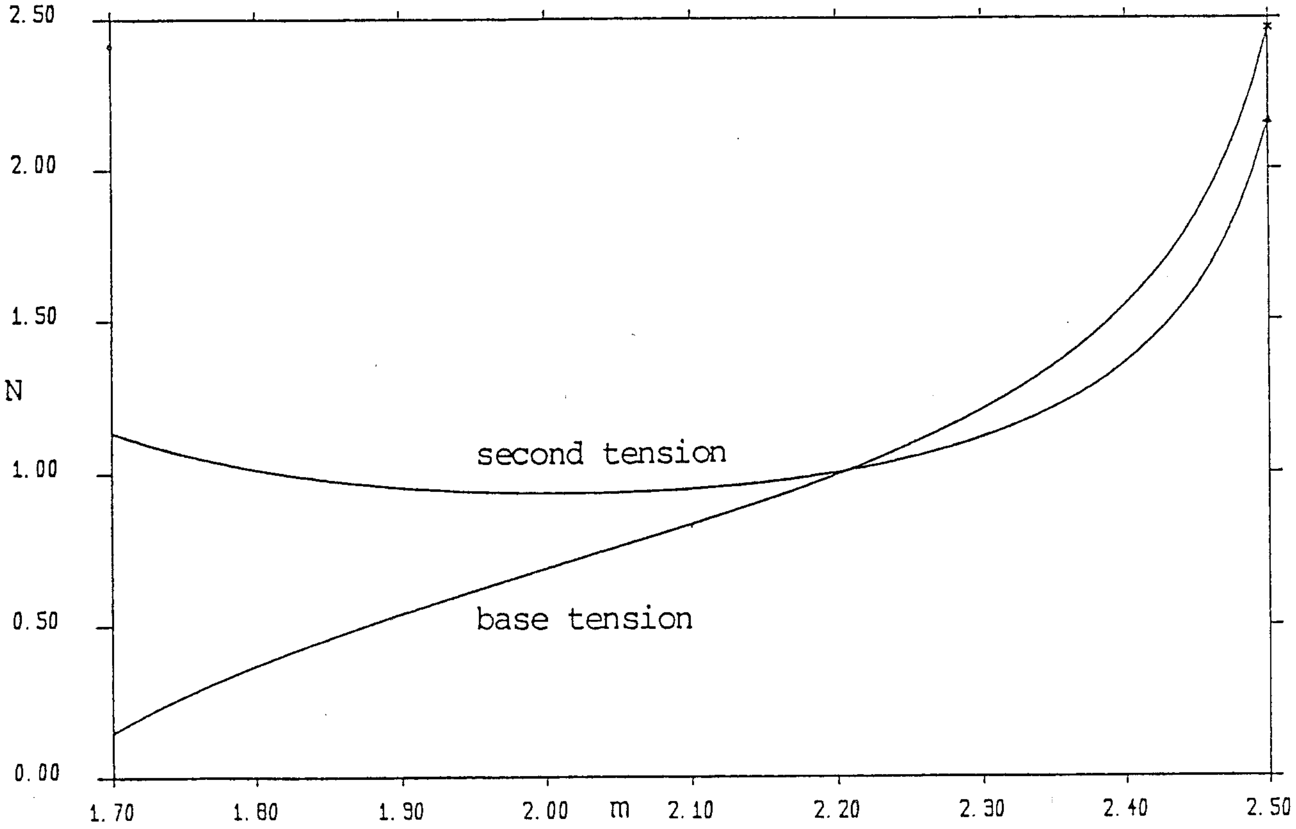

Figure 5.8 Calculated mooring tensions versus extension

These graphs may be constructed experimentally. Table 5.3 shows the measured tensions in the mooring lines for a static experiment in which the fore and aft mooring lines were attached to a stationary point. The modulus of the ´x´ and ´y´ tensions was calculated for the fore and aft cases, and the angles also calculated. The results are for the base sections only, and are compared with static theory in figures 5.9, 5.10, 5.11, and 5.12. The fit for both tensions is reasonable, and also the fit for the fore angle. The aft angle curve is approximately correct, but is vertically displaced by about 2 degrees.

If we return to equations 1 and 2, we can examine the sensitivity of angle and tension to changes in the up or downthrust. It transpires that a 1% difference between the up and downthrust produces a 2% difference in the tensions of P and Q, and a 1 degree difference in their angle. This helps to put the fit of theory and experiment into perspective - figure 5.10 implies that up and downthrust in the model have been matched to a few percent.

TABLE 5.3 STATIC TEST OF MOORING STIFFNESS

	BASE LENGTH m	HEAVE FORCE mN	SURGE FORCE mN	ANGLE	MODULUS mN
FORE	1.5	21	44	25.5	49
	1.6	64	93	34.5	113
	1.7	163	194	40.0	253
	1.8	258	294	41.3	391
	1.9	342	391	41.2	519
	2.0	414	496	39.9	646
	2.1	485	622	37.9	789
	2.2	568	783	36.0	967
	2.3	677	1006	33.9	1196
	2.4	873	1422	31.5	1669
	2.5	1447	2563	29.4	2943
AFT	1.5	70	104	33.9	125
	1.6	129	183	35.2	224
	1.7	192	247	37.9	313
	1.8	259	324	38.6	415
	1.9	323	406	38.5	519
	2.0	388	498	37.9	631
	2.1	458	610	36.9	763
	2.2	530	750	35.2	918
	2.3	625	972	32.7	1156
	2.4	790	1401	29.4	1608
	2.5	1583	3304	25.6	3664

Angle is derived from $\arctan\left[\frac{\text{heave force}}{\text{surge force}}\right]$

Mooring line lengths mm

	p	q	r
fore	845	482	1418
aft	855	492	1438

Fore surge spring constant at 2 m base length $= \frac{0.610 - 0.400}{0.2} = 1.02$ N/m

Aft surge spring constant at 2 m base length $= \frac{0.622 - 0.391}{0.2} = 1.16$ N/m

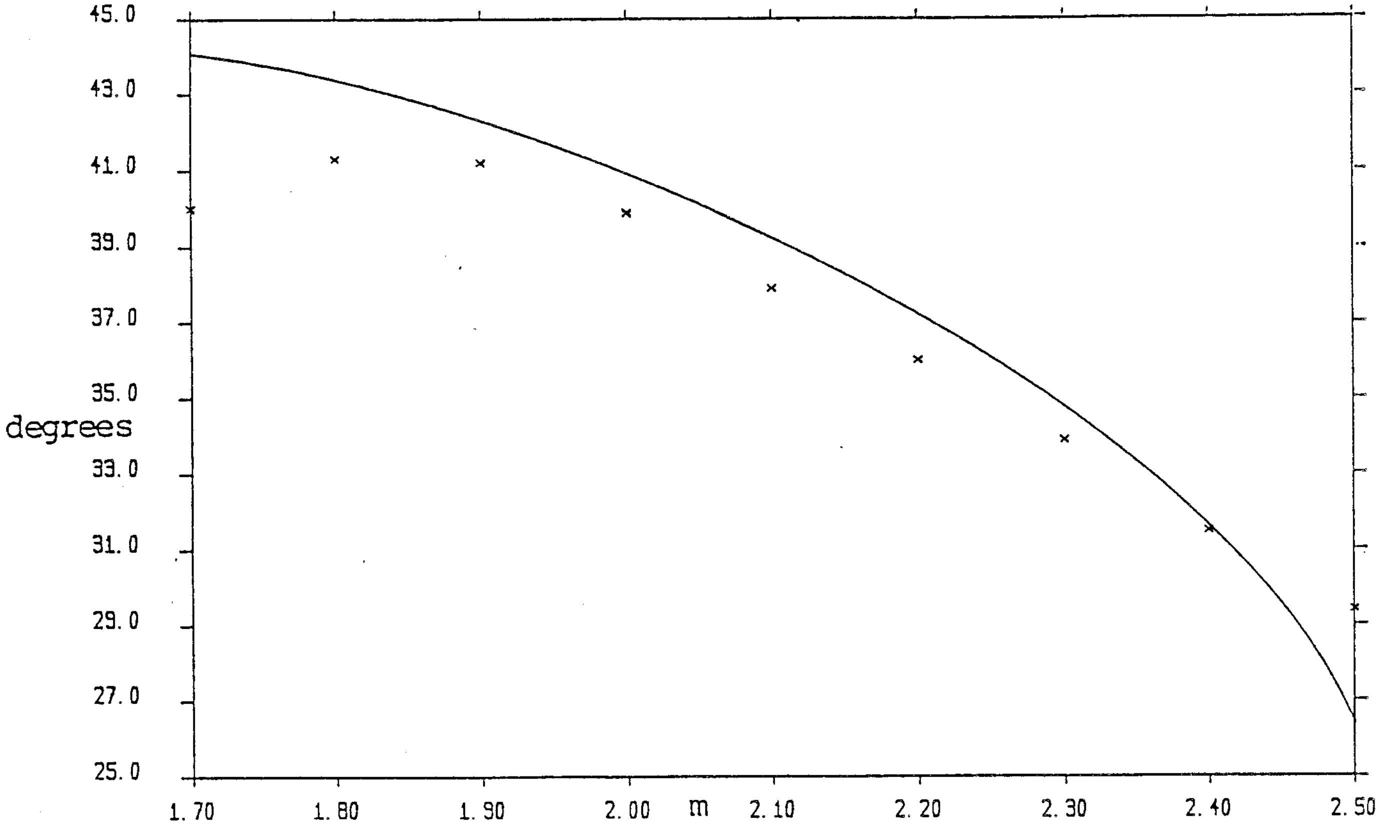

Figure 5.9 Fore base angle: measured versus calculated

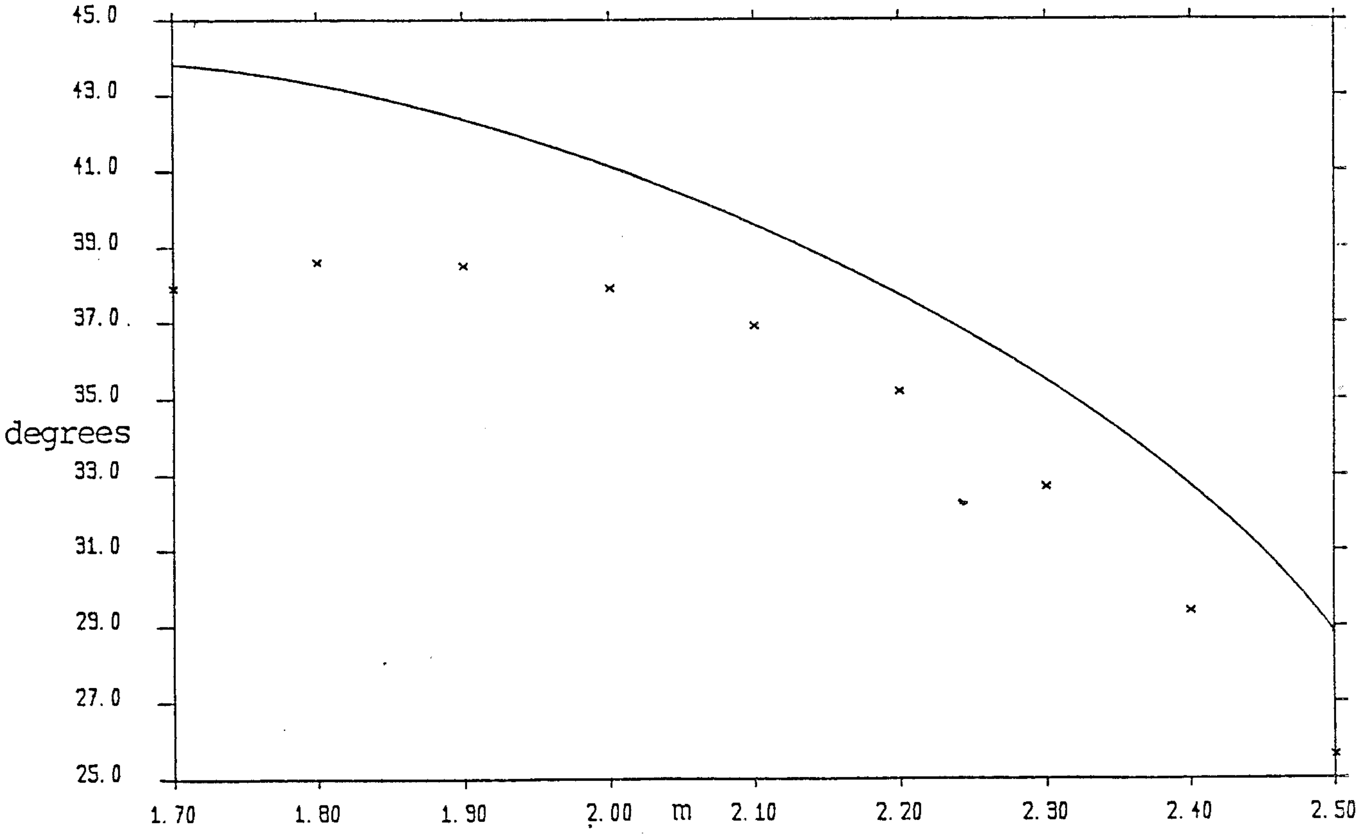

Figure 5.10 Aft base angle: measured versus calculated

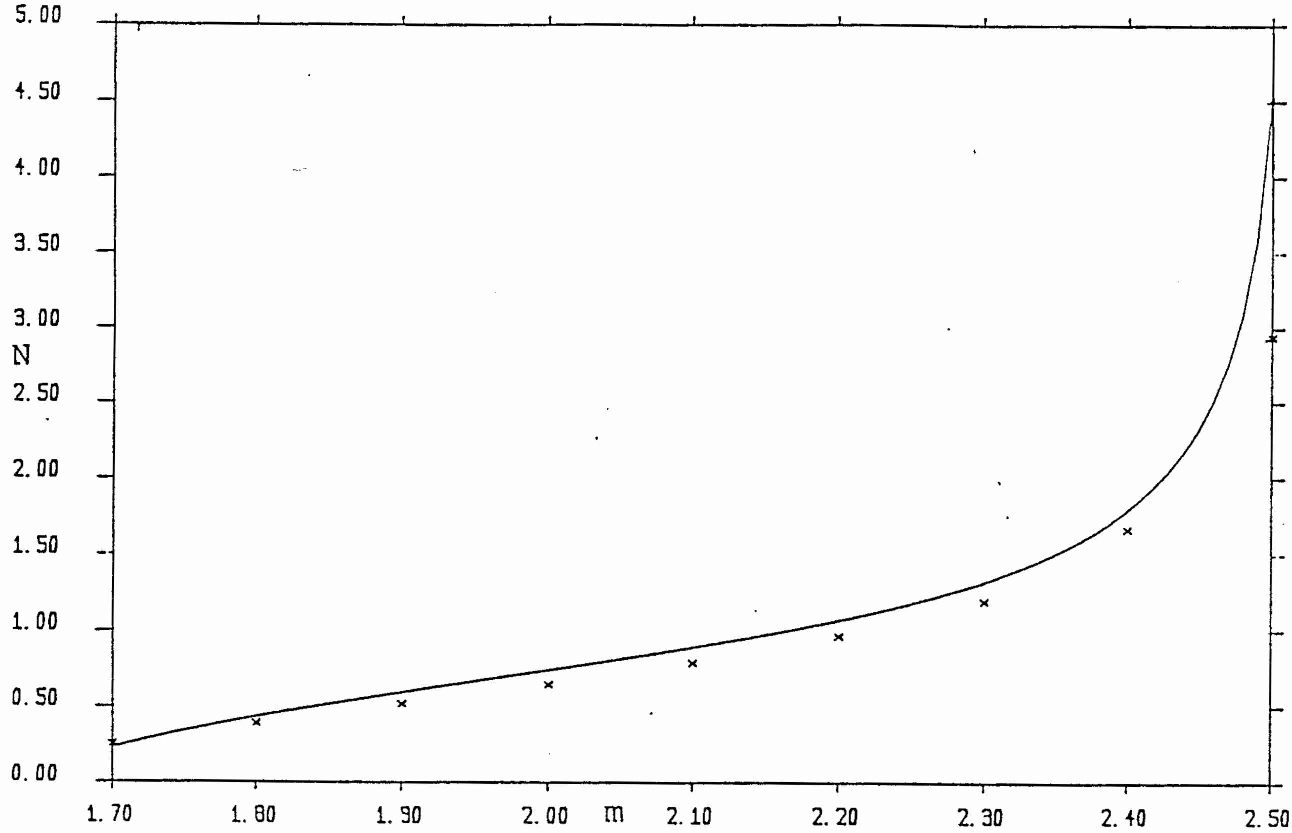

Figure 5.11 Fore base tension: measured versus calculated

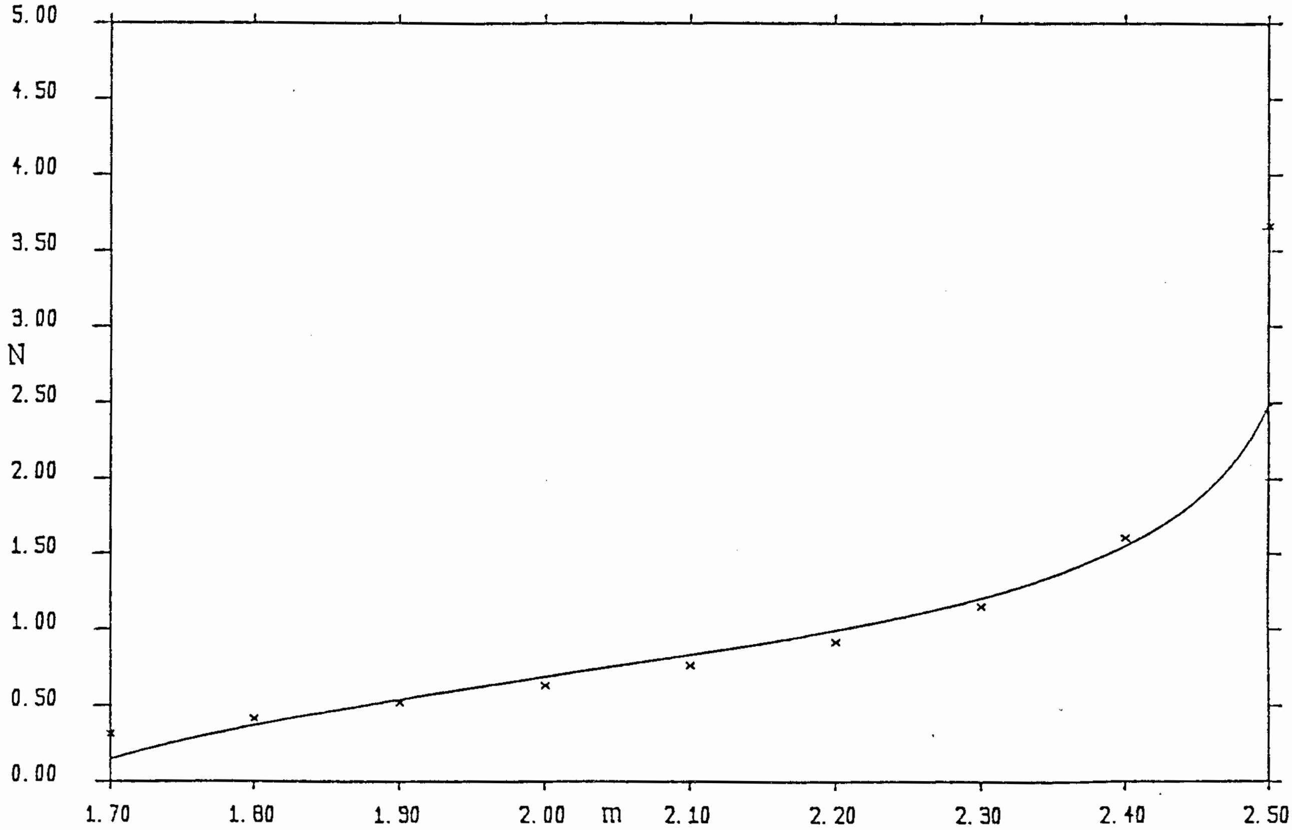

Figure 5.12 Aft base tension: measured versus calculated

With the anchor gauge alone we needed to assume that the up and downthrust were equal in order to derive the two angles A and B.

However, we also have the position gauge to help us. Since the lines remain in tension all the time, the straight line geometry shown in figure 5.13 applies, and the derivation of angles A, B, C follows below. This algebra is used in the derivation of the angle time series in Section 3.

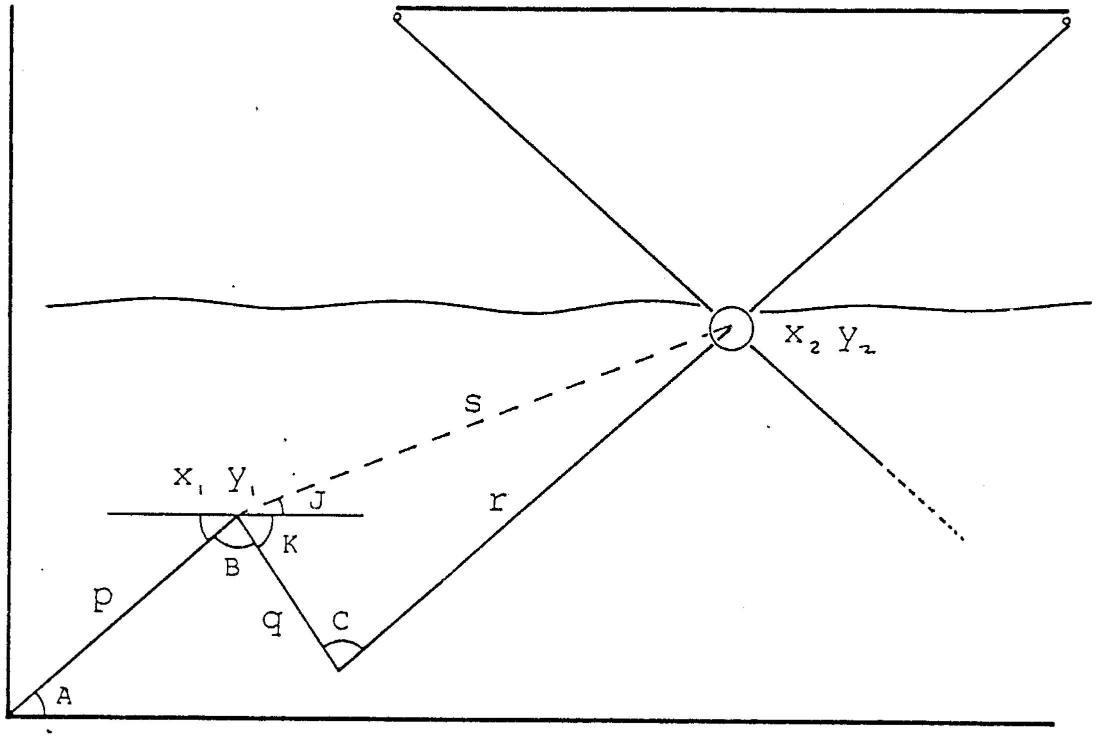

Figure 5.13 Mooring line geometry

(1) $A = \arctan\left[\dfrac{\text{heave force}}{\text{surge force}}\right]$

(2) $x_1 = p \cos A$ (3) $y_1 = p \sin A$

x_2 and y_2 are measured with the position gauge

(4) $s^2 = (x_2 - x_1)^2 + (y_2 - y_1)^2$

(5) $J = \arctan\left[\dfrac{y_2 - y_1}{x_2 - x_1}\right]$

From the cosine rule:

(6) $C = \arccos\left[\dfrac{q^2 + r^2 - s^2}{2\,q\,r}\right]$

From the sine rule:

(7) $K = \arcsin\left[\dfrac{r}{s} \sin C\right] - J$

From the diagram:

(8) $B = pi - A - K$ (radians)

APPENDIX D THE MOORING DYNAMICS

In translation, a system of N bodies with C constraints has 3N - C degrees of freedom. The mooring has 2 bodies - the float and sinker - and 3 constraints, namely that the float and sinker move in separate spherical arcs centered respectively on the anchor and the spine, and further, remain always at the same distance from each other because they are tethered by a line which remains taut. Hence there are 3 degrees of freedom, and therefore 3 modes of oscillation. A quick sketch, or observation of the mooring itself reveals that 2 oscillations are in sway, with the bodies moving normal to the plane of the mooring, and either in or out of phase with each other, and that the 3rd oscillation is in heave, with the bodies necessarily in phase.

A rigorous treatment would consider the dynamics of the mooring in all three dimensions. However, we are mainly interested in the resonances the mooring may possess, particularly if they are in the frequency-band of external forces to which it is subjected. Now, the float and sinker produce their restoring forces in the vertical plane. It is clear, therefore, that the heave oscillation will cause first and higher order restoring forces, and that sway, which produces only incidental heave motion, will produce second and higher order restoring forces. Only first order forces are linear and consequently only the heave motion will have a resonance whose frequency does not change with the amplitude of oscillation.

The heave motion, in the mooring plane, can be analysed in two dimensions. In figure 5.14 the loci of the float and sinker are shown; they follow arcs centred on the anchor and spine respectively. The float and sinker are further constrained by the line which joins them, which remains taut unless the float or weight are subjected to large accelerations (approaching g). Consequently, if the float is at any arbitrary point on its arc, the sinker is constrained to be at either of the two points where the arc of the line q intersects the arc of r. In practice the position which puts the sinker lower will have lower potential energy. We can therefore write an expression for the angle C in terms of the angle A. Note that because there is range of possible positions for the float and sinker, and yet an equilibrium position exists, a restoring force is implied, and therefore the possibility of a resonance.

Equation 3 is the Langrangian, the difference of the potential and kinetic energies for the system. The system will move so as to minimise the integral with respect to time of this difference. Equation 4 is the Euler equation which must be satisfied for this minimum to exist. These two equations allow the dynamics of the system to be inferred. The following steps lead to equation 16 for the angular acceleration of the float in terms of its angular displacement. One may make some simplifications to this expression and derive equation 19 which shows that the system behaves in the same way as a simple pendulum - that is, it has a resonant frequency which is dependant solely on the acceleration of gravity, and an effective line length. The two methods agree, and indicate a resonance of 0.34 Hz, at the bottom end of the wave frequency band.

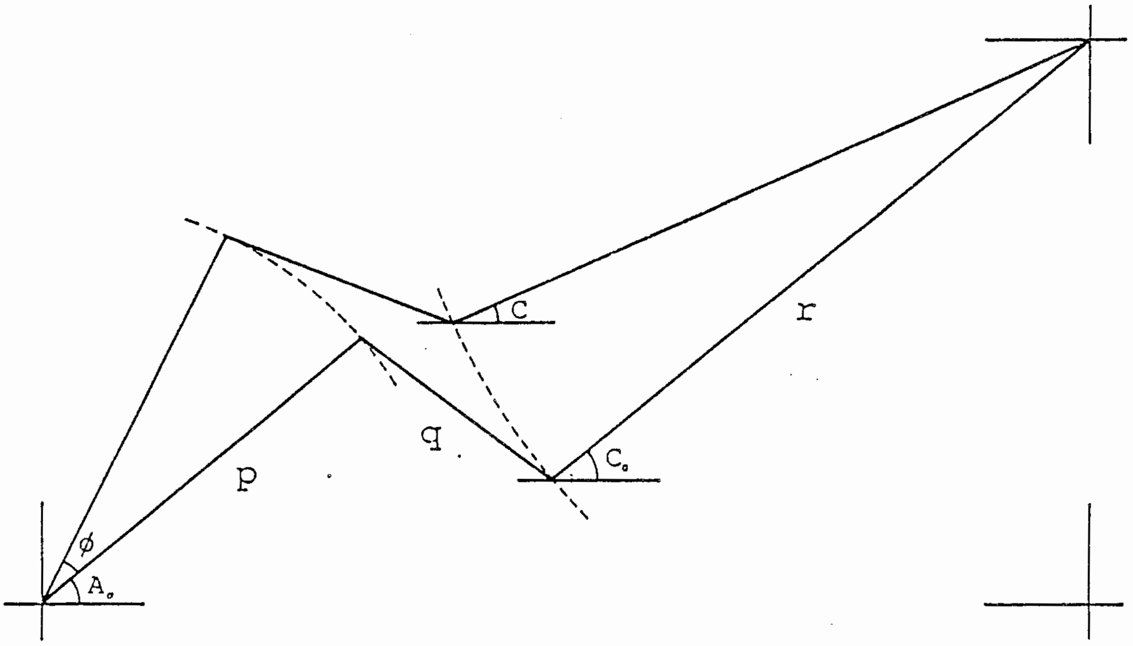

Figure 5.14 Mooring line dynamic displacement

When section p of the mooring line moves through an angle of ϕ radians, section r moves through an angle which is some function of ϕ. We may write this as:

(1) $A = A_0 + \phi;$ (2) $C = C_0 + f(\phi)$

By arrangement, float upthrust = sinker downthrust = F (say)

By coincidence, mass + hydrodynamic added mass is about the same for both float and sinker - let this equal m.

Let T = kinetic energy, and V = potential energy of the float and sinker.

(3) $L = T - V;$ (4) $\frac{\partial L}{\partial \phi} = \frac{d}{dt}\left[\frac{\partial L}{\partial \dot{\phi}}\right]$

(5) $$T = \frac{m}{2}(p\,\dot{A})^2 + \frac{m}{2}(r\,\dot{C})^2$$

(6) $$V = -F\,p\,(\sin A - \sin A_0) - F\,r\,(\sin C - \sin C_0)$$

(7) $$\frac{\partial L}{\partial \phi} = \frac{\partial(-V)}{\partial \phi} = F\left[p\cos A + r\cos C\,\frac{dC}{d\phi}\right]$$

(8) $$\frac{\partial L}{\partial \dot{\phi}} = \frac{\partial T}{\partial \dot{\phi}} = \frac{m}{2}\left[p^2\,2\,\dot{A} + r^2\,2\,\dot{C}\,\frac{d\dot{C}}{d\dot{\phi}}\right]$$

(9) $$\frac{d}{dt}\left[\frac{\partial L}{\partial \dot{\phi}}\right] = \frac{d}{dt}\,\frac{\partial T}{\partial \dot{\phi}} = m\left[p^2\ddot{A} + r^2\ddot{C}\,\frac{d\dot{C}}{d\dot{\phi}} + r^2\dot{C}\,\frac{d}{dt}\left[\frac{d\dot{C}}{d\dot{\phi}}\right]\right]$$

It is clear from the diagram that when section q of the mooring line is displaced from the rest position, it undergoes a combination of rotation and translation. However, the rotation is second order: the motion of the sinker relative to the float is small compared with their mutual translation; and the direction of rotation of q is always positive whether ϕ is positive or negative.

So, when ϕ is small, the sections p and r remain very close to parallel, the rotation of q is negligible, and the float moves a distance $p\phi$ which is identical to the distance $r(C - C_o)$ moved by the sinker. Because the float and sinker move together, their acceleration and velocity must also be the same. Therefore

$$\frac{\ddot{C}}{\ddot{A}} = \frac{\dot{C}}{\dot{A}} = \frac{dC}{d\phi} = h \quad \text{(say)}$$

Because $A_o = C_o$ we may write from (1) and (2)

(10) $A = A_o + \phi$; and (11) $C = A_o + h\phi$ and therefore

(12) $p\,\phi = -r\,h\,\phi$ (minus because C decreases as A increases)

and so

(13) $h = -\dfrac{p}{r}$

Re-examining equation (9) $\dfrac{d\dot{C}}{d\dot{\phi}} = h$, and therefore $\dfrac{d}{dt}\left[\dfrac{d\dot{C}}{d\dot{\phi}}\right] = 0$

so (9) becomes

(14) $\dfrac{d}{dt}\left[\dfrac{\partial T}{\partial \dot{\phi}}\right] = m\left[p^2\ddot{A} + r^2\ddot{C}\,h\right] = m\,\ddot{A}\left[p^2 + r^2h^2\right] = 2\,m\,p^2\ddot{A}$

and (7) becomes

(15) $\dfrac{-\partial V}{\partial \phi} = F\;p\,(\cos A + h\,r\cos C) = F\,p\,(\cos A - \cos C)$

Because of (4) we may equate (14) and (15), yielding

(16) $\ddot{A} = \ddot{\phi} = \dfrac{F}{2\,m\,p}\left(\cos(A_o + \phi) - \cos(A_o + h\phi)\right)$

The trigonometric terms in brackets expand to

(17) $(\cos A_o\cos\phi - \sin A_o\sin\phi - \cos A_o\cos h\phi + \sin A_o\sin h\phi)$

When ϕ is small $\sin\phi \to \phi$ and $\cos\phi \to 1$
And because $\dfrac{p}{r} < 1$ $\sin h\phi \to h\phi$ and $\cos h\phi \to 1$

Expression (17) therefore contracts to $\sin A\,(h\phi - \phi)$, hence

$$(18) \quad \ddot{\phi} = \frac{-F}{2\,m\,p}(\phi - h\phi)\sin A = \frac{-F}{2\,m\,p}\phi\,\left(1 + \frac{p}{r}\right)\sin A$$

$$(19) \quad \ddot{\phi} = \frac{-F}{m}\,\frac{(p + r)}{2\,p\,r}\sin A \quad \phi$$

Equation (19) shows that for small displacements, the mooring undergoes simple harmonic motion, analogous to a pendulum.

A pendulum has $\ddot{\phi} = -\frac{g}{l}\phi$ and a resonant frequency of $\frac{1}{2\,\pi}\left[\frac{g}{l}\right]$

Substituting in (19) the values for the aft mooring line:

$F = .125\ g$, $m = .164$, $p = .855$, $r = 1.438$, $A = .7175$ rad

$$\text{resonance} = \frac{1}{2\,\pi}\left[\frac{.125 \quad 2.293 \quad \sin\,(.7175) \quad 9.82}{.164 \quad 2 \quad .855 \quad 1.438}\right] = \underline{\underline{0.34\ \text{Hz}}}$$

We ran an experimental frequency scan of the mooring model. The mooring was detached from the spine and clamped rigidly at the same position the spine assumes in the water. The other end of the mooring remained anchored as before. A wave gauge was located directly above the float. A series of waves, with frequencies from 0.195 to 1.93 Hz in steps of .195 Hz was generated. The heave and surge forces were recorded. The rms surge motion of the float was calculated, and in figure 5.16 is compared with the measured rms wave motion corrected to that at the float depth.

The graph has a number of interesting features. The motion of the float is greater than that of the water at the float depth at all frequencies except between 0.5 and 0.6 Hz, where the wave amplitude shows an unexpected increase. Whereas the wave amplitude at the water surface was set to be 10 mm (7 mm rms) the wave amplitude decays exponentially with frequency, and is effectively zero above 1.4 Hz. The float motion however approaches an asymptotic value of 1.4 mm rms, or about 1/5 of the surface motion. One may reasonably assume that this is due to wave forces (inertial and viscous) on the mooring line itself. There is a pronounced peak in the float motion at around 0.4 Hz. Figure 5.16 shows an expanded view of this peak, from 0.2 to 0.6 Hz; the float motion has been normalized by dividing by the water motion at the depth of the float. A definite resonance peak occurs at 0.37 Hz, with about 2.5 times the water motion. The frequency is low enough, and the water surface clear enough to observe this float resonance directly. And the frequency agrees closely with that calculated.

In the existing mooring system the float has a single point attachment below its centre of buoyancy. It will behave as an inverted compound pendulum, with first-order restoring forces. Two more degrees of freedom have been introduced, roll and pitch, which because the float is symmetrical, produce a single resonance. The sinker has a two point fixing, at either end of the cylinder. It can oscillate in pitch and yaw, at a similar frequency to the float, since the masses and dimensions are comparable. A quick test,

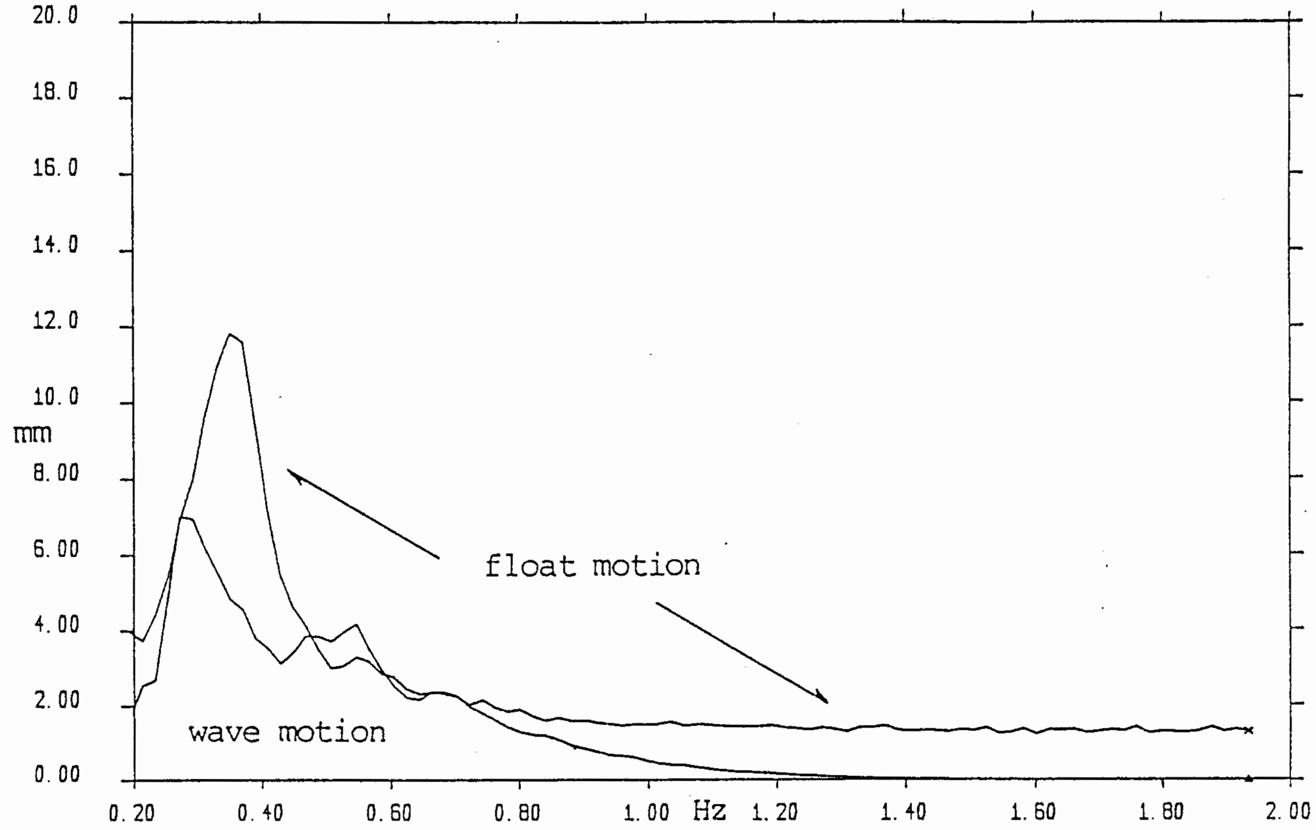

Figure 5.15 Rms surge motion versus frequency

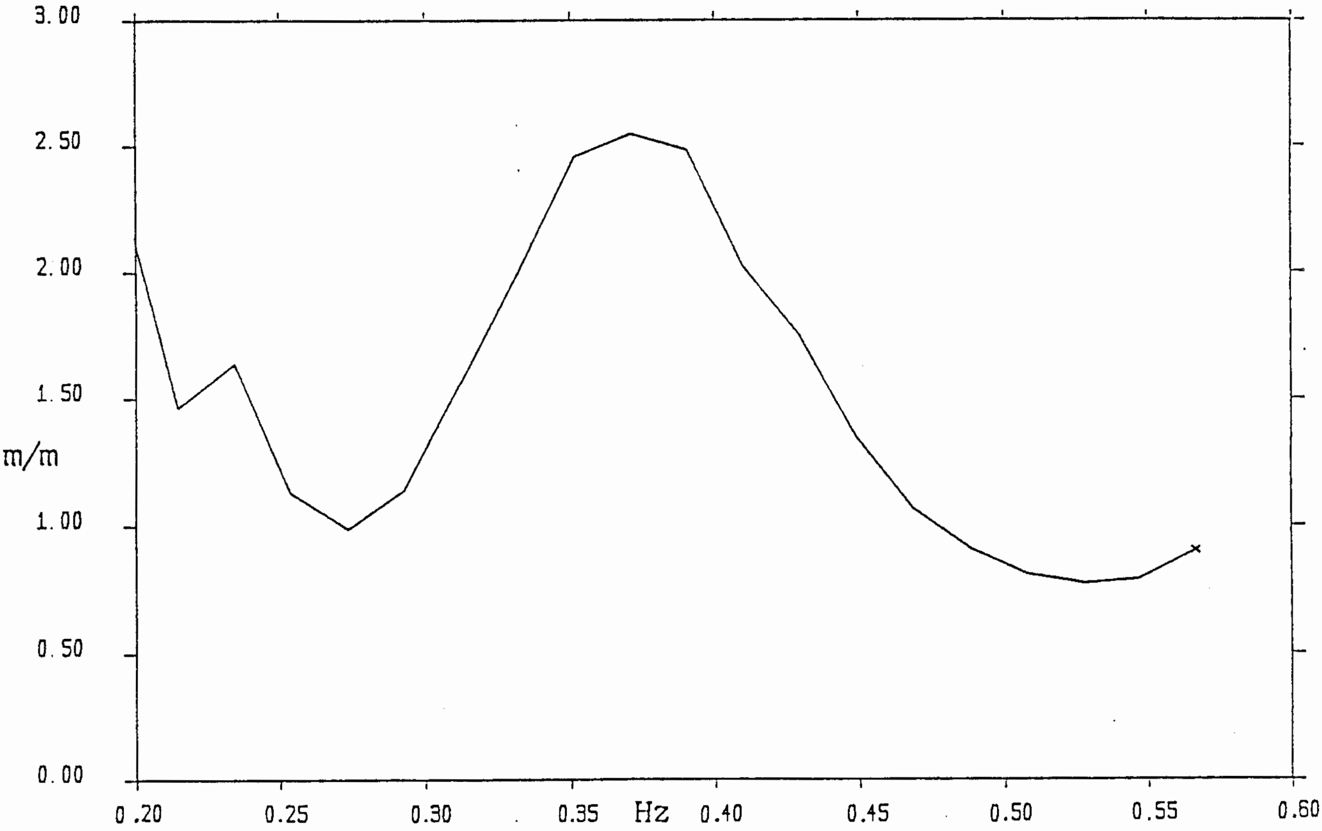

Figure 5.16 Normalised float surge motion versus frequency

oscillating the mooring by hand, indicated a float and sinker resonance around 3 Hz.

An important point is that these oscillation modes are not orthogonal, and may therefore couple. The float and sinker resonances can be heave-driven, the heave motion may be provoked by higher orders of sway.

Potentially, the mooring has a rich response to impulse, and this response covers the wave frequency band typical of the North Atlantic. The effects of this are apparent in the time series of mooring forces. It is clear that we should give serious attention to damping mechanisms and attachment points of the float and sinker.

REFERENCES

1) Bending moments in long spines, Edinburgh Wave Power Project, 1984.

2) Pirelli Project No. 8526P, Comparative fatigue tests on 3 core 22 kV A.C. submarine cable for floating wave energy convertors, 1983.